

**CZECH TECHNICAL
UNIVERSITY
IN PRAGUE**

Faculty of Nuclear Sciences and Physical Engineering

DISSERTATION

New concepts in laser wakefield acceleration

Prague 2024

Dominika Mašlárová

Bibliografický záznam

Autorka	Ing. Dominika Mašlárová, České vysoké učení technické v Praze, Fakulta jaderná a fyzikálně inženýrská, Katedra fyzikální elektroniky
Název práce	Nové koncepty v urychlování elektronů brázdovou vlnou
Studijní program	Aplikace přírodních věd
Specializace	Fyzikální inženýrství
Školitel	doc. Ing. Jan Pšikal, Ph.D., České vysoké učení technické v Praze, Fakulta jaderná a fyzikálně inženýrská, Katedra fyzikální elektroniky
Školitel specialista	Ing. Miroslav Krůs, Ph.D., Akademie věd České republiky, Ústav fyziky plazmatu
Akademický rok	2023/2024
Počet stran	131
Klíčová slova	urychlování elektronů laserem na brázdové vlně, relativistické urychlování elektronů, particle-in-cell simulace, betatronové záření, plazmové urychlování leptonů

Bibliographic Entry

Author	Ing. Dominika Mašlárová, Czech Technical University in Prague, Faculty of Nuclear Sciences and Physical Engineering, Department of Physical Electronics
Title of dissertation	New concepts in laser wakefield acceleration
Study Programme	Applications of Natural Sciences
Field of Study	Physical Engineering
Supervisor	doc. Ing. Jan Pšíkal, Ph.D., Czech Technical University in Prague, Faculty of Nuclear Sciences and Physical Engineering, Department of Physical Electronics
Supervisor specialist	Ing. Miroslav Krůs, Ph.D., Institute of Plasma Physics of the Czech Academy of Sciences
Academic Year	2023/2024
Number of Pages	131
Keywords	laser wakefield acceleration, relativistic electron acceleration, particle-in-cell simulations, betatron radiation, plasma-based lepton acceleration

Abstrakt

V této práci jsou představeny nové koncepty spojené s urychlováním elektronů na laserem vybuzené brázdové vlně (LWFA z angl. laser wakefield acceleration), což je technika urychlování elektronů na relativistické energie. Brázdová vlna je generována a tažena ultrakrátkým a ultraintenzivním laserovým impulzem při šíření v plazmatu a vytváří tak vhodné elektrické pole pro urychlování elektronů. V brázdovém poli můžeme dosáhnout výrazně vyšších akceleračních gradientů než jsou schopny dnešní, typicky využívané, radiofrekvenční urychlovače. To umožňuje stavět výrazně kompaktnější urychlovače, což je potenciálně výhodné nejen pro velké infrastruktury, jako jsou lasery na volných elektronech nebo elektronové-pozitronové srážecí, ale také pro malá výzkumná, lékařská a průmyslová zařízení. Avšak k tomu, aby bylo LWFA uvedeno do praxe, je potřebné soustředit výzkum na několik faktorů ovlivňujících zařízení založené na LWFA. Například kvalita elektronových svazků, která je závislá na procesu vstříknutí elektronů do brázdového pole a jejich následném urychlení, vyžaduje další zlepšení. Dále je potřeba zabývat se aspekty jako je stabilita a laditelnost parametrů elektronových svazků, prodloužení délky urychlování, zvýšení zisku sekundárních rentgenových zdrojů nebo kompaktní plazmové urychlování pozitronů pro potenciální budoucí elektronový-pozitronový srážecí. V této práci jsou představeny nové koncepty v rámci LWFA studovány pomocí numerických "particle-in-cell" simulací. První koncept navrhuje, že ultrakrátký elektronový svazek s nábojem stovek pC lze kontrolovatelně produkovat samotným vývojem laserového impulzu v průběhu šíření plazmatem, a to v případě, když je laserový impulz fokusován do super-Gaussova prostorového profilu místo do typického Gaussova profilu. Dále byla zkoumána nová metoda vstřikování elektronů do brázdové vlny, založená na srážce dvou laserových impulzů pod ostrým úhlem. Výsledky ukazují, že vstřikování elektronů ve většině případů probíhá jenom do jedné z příslušných brázdových vln v závislosti na časovém zpoždění mezi impulzy. Výsledky ze simulací jsou rovněž podpořeny experimenty provedenými spolupracovníky z University of Nebraska, Lincoln v USA. Další navazující studie provedená v rámci této spolupráce experimentálně prověřila potenciál vstřikování elektronových svazků do obou brázdových vln. Mimo to bylo pozorováno vytváření prstencových elektronových struktur. Další koncept se zaměřuje na novou metodu zvýšení intenzity betatronového záření, což je ultrakrátký zdroj rentgenového záření, generovaný příčnými oscilacemi elektronů během procesu LWFA. Zvýšení intenzity je v tomto případě zprostředkováno lokální modulací hustoty plazmatu. Nakonec byla zkoumána generace a akcelerace pozitronů pomocí ultraintenzivního laserového impulzu v plazmovém kanálu. Tyto poznatky mohou přinést nové přístupy k urychlovačům založeným na metodě LWFA a zvýšit jejich celkovou funkčnost a využitelnost.

■ Abstract

This thesis introduces a series of innovative concepts in the field of laser wakefield acceleration (LWFA), a cutting-edge method for accelerating electrons to relativistic energies. The electric field suitable for acceleration is provided by a plasma wave (wakefield) generated and dragged by an ultrashort, ultraintense laser pulse propagating through plasma. The wakefield can achieve significantly higher accelerating gradients than the state-of-the-art radiofrequency accelerators. Therefore, it can provide remarkably compact acceleration, which is beneficial not only for large-scale infrastructures, such as the free electron laser or electron-positron collider, but also for small-scale research, medical, and industrial facilities. However, in order to introduce LWFA for applications, focused research on several factors that influence the performance of LWFA is still required. For instance, the quality of electron beams, which depends on the injection of electrons into the wakefield as well as their further acceleration, needs to be improved. More aspects need to be addressed as well, such as stability and tunability of electron beams, prolongation of the acceleration length, enhancement of the gain of secondary X-ray sources, or compact plasma-based positron acceleration for a potential future electron-positron collider.

In this work, several of these topics are addressed by proposing new concepts via numerical particle-in-cell simulations. The first concept suggests that a laser pulse, when focused into a super-Gaussian spatial profile rather than the conventional Gaussian profile, can controllably self-produce an ultrashort electron beam characterized by a substantial charge in the order of hundreds of pC. Next, a novel optical injection process, based on the collision of two laser pulses at an acute angle, is presented. The results reveal that the injection can occur in one of the respective wakefields, depending on the temporal delay between the pulses. This work is also supported by experimental results obtained by collaborators at the University of Nebraska, Lincoln, USA. Following study carried out within this collaboration examined the potential of injecting electron beams into both wakefields. In addition, the creation of ring-like electron structures was observed. The next concept studied in this thesis focuses on a novel method of the enhancement of betatron radiation, an ultrashort X-ray radiation source, generated by transverse oscillations of electrons during the LWFA process. This method, based on the use of a plasma density modulation, offers an experimentally achievable increase of the radiation gain. Finally, a one-stage generation and acceleration of positrons with a highly intense laser pulse in a plasma channel is examined. These discoveries might bring new insights into several aspects of laser wakefield accelerators and improve their overall performance.

■ Declaration

I declare that this thesis is my own work. I have acknowledged all the sources used and listed them in the bibliography.



Ing. Dominika Mašlárová

Acknowledgments

This dissertation would not be possible without extensive support from numerous people throughout my studies. First of all, I would like to express my sincere gratitude to my supervisor, Jan Pšikal, for his awesome guidance over the years. His willingness to share his academic knowledge, regularly check on my progress, engage in thoughtful discussions about my concerns, and promptly respond to my questions and emails has been invaluable. My gratitude extends to the Department of Physical Electronics of FNSPE, CTU in Prague, for the opportunity to study and work in such an inspiring place where I have always felt so welcomed.

I would also like to thank my supervisor-specialist, Miroslav Krůs, with whom I have spent many great years working. Thanks for involving me in the research at IPP and for believing in me from the very beginning. I appreciate the trust in my ideas, even when they seemed doubtful in the first place. Thanks for giving me both freedom and invaluable constant support. I would never be where I am without this.

I had incredible luck meeting so many amazing people during my Ph.D. journey to whom I am exceptionally grateful. My sincere thanks go to Donald Umstadter for the opportunity to be a part of the research at UNL. Working under his guidance has been a great honor for me. I deeply appreciate the valuable insights, the direction he provided in our research, and the warm and engaging interactions we had, both in-person in Nebraska and during our online meetings. I would like to also thank Qiang Chen for his mentorship and so many invaluable lessons that we went through together. Our late-night European, early-morning U.S. brainstorming sessions extended to weekends, the constant exchange and refinement of ideas, and the persistent process of making corrections have been an extraordinary part of my learning experience. His commitment and drive have been immensely inspirational, teaching me the importance of persistence and patience. A special thanks go to Qiang's wonderful wife Lily for her enriching feedback on our work and her exceptional hospitality. I would like to also thank Grigory Golovin for starting the collaboration and also his family and my dear friend Junzhi Wang for taking care of a carless person in the US. I am immensely grateful to Marija Vranic for making it possible for me to come to Lisbon and supervising me during my whole stay. Our discussions were enriching to me and I learned truly a lot, especially in terms of problem-solving approaches and research presenting. This experience has transformed my way of thinking as a scientist, a change that continues to influence me deeply. Thanks also go to Bertrand Martinez for our collaboration and the fantastic times and fun we shared. My appreciation also goes to the entire GOLP group at IST, for taking me as one of them, for so many countless hours of discussions on physics and beyond, bouldering, marvelous evenings and nights, and crazy trips that I will always have „saudades“ about. I am very grateful to Tünde Fülöp for giving me new opportunities that I am already excited about and for her exceptional care and support. And big thanks, of course, go to Vojtěch Horný for always being my mentor, regardless of the formal status.

I would like to express my gratitude to the people who helped me improve this thesis. Thanks to Róbert Babjak for the discussions on DLA and for our essential coffee breaks. Thanks to Jaroslav Horníček for being openly critical of my Czech language skills and for being such a good friend to me. Thanks to David Gregocki for detailed comments on my work, supplies of music, and for teaching me so much, professionally and personally.

I would like to thank my friends outside academia for keeping me sane and grounded, reminding me that there is a world beyond research. Completing this Ph.D. journey has been an extraordinary chapter in my life, and it would not have been possible without the support of my dear parents. Their sacrifices, both big and small, have paved the way for my achievements. This work shows not only my dedication but also how much they love and support me. Immense thanks go to my grandpa for his enduring support and his continuous presence in my life. To my brother, of course, I owe thanks for his patience with his sister, for our great relationship, and for being the best sibling one could wish for. I am deeply grateful to my dear Peter, who has never doubted what I am capable of. His belief in me has been a constant source of strength. Thanks for taking this journey with me and for being my closest confidant. I believe there is so much more waiting for us.

And now... let's do physics!



Contents

Contents	17
Introduction	21
Part I	
Principle of laser wakefield acceleration (LWFA)	
1 Features of laser pulses used in LWFA	25
1.1 General properties of the laser light	25
1.2 Generation of ultrashort ultraintense laser pulses	25
1.3 Gaussian laser beams	26
1.4 Typical features of the laser beams used in LWFA	29
2 Field ionization and plasma generation	31
2.1 Types of field ionization	31
2.2 Creation of plasma by ultraintense laser fields	32
2.3 Propagation of ultraintense laser pulses in plasma	34
3 Generation of laser wakefield	37
3.1 Plasma sources	37
3.2 Wakefield generation	37
3.2.1 Linear regime	38
3.2.2 Nonlinear regime	39
3.3 Dephasing length and depletion length	44
4 Electron injection	45
4.1 Electron trapping condition	45
4.2 Properties of electron beams	47
4.3 Self-injection	48
4.4 Other injection mechanisms	49
4.4.1 Optical injection	49
4.4.2 Density down-ramp injection	50
4.4.3 Ionization injection	50
4.4.4 Injection by nanoparticles	51
4.4.5 External injection	51
4.4.6 Combined injection methods	52
5 Other laser-driven and plasma-based electron acceleration methods	53
5.1 Plasma beat wave acceleration	53

5.2 Acceleration by a train of short laser pulses	54
5.3 Self-modulated laser wakefield acceleration	54
5.4 Direct laser acceleration	54
5.5 Plasma wakefield acceleration	55
6 X-ray sources from LWFA electrons	57
6.1 Radiation generated by a single charged particle	57
6.2 Betatron radiation	58
6.3 Other secondary sources of X-rays from LWFA electrons	60
6.3.1 Free electron laser (FEL)	60
6.3.2 Inverse Compton scattering	62
6.3.3 Bremsstrahlung	62
6.4 Radiation reaction	63
7 Towards applications	65
7.1 Applications of LWFA electron beams	65
7.1.1 Electron-positron collider	65
7.1.2 Medical applications of relativistic electrons	67
7.1.3 Material probing with LWFA electrons	68
7.1.4 Applications of secondary X-ray sources	68
7.2 Current challenges in the LWFA field	70
7.2.1 High-quality properties of electron beams	70
7.2.2 Diffraction, dephasing, depletion and accelerator staging	71
7.2.3 Reproducibility and tunability	73
7.2.4 Repetition rate	73
7.2.5 Improvement of X-ray sources	74
7.2.6 Plasma-based acceleration of positrons	74
Part II	
Proposals of new concepts	
8 Methods: Particle-in-cell (PIC) simulations	79
8.1 Basics of the PIC method	79
8.2 Additional modules for PIC codes	83
8.3 Methodology employed in this work	84
9 Proposed concepts	87
9.1 Publication A: Laser wakefield accelerator driven by the super-Gaussian laser beam in the focus	87
9.2 Publication B: Transient Relativistic Plasma Grating to Tailor High-Power Laser Fields, Wakefield Plasma Waves, and Electron Injection	88
9.3 Publication C: Injection of electron beams into two laser wakefields and generation of electron rings	89
9.4 Publication D: Betatron radiation enhancement by a density up-ramp in the bubble regime of LWFA	90
9.5 Publication E: Radiation-dominated injection of positrons generated by the nonlinear Breit-Wheeler process into a plasma channel	91
Conclusion	93
Bibliography	97

Appendix: Included publications	121
Publication A	123
Publication B	125
Publication C	127
Publication D	129
Publication E	131



Introduction

Particle acceleration is an intrinsic and fundamental part of physics. It is well-connected with many disciplines such as nuclear physics, high-energy physics, astrophysics, or condensed matter physics, and contributes to a broad range of applications including industry (radiography, isotope production, material testing and modification, X-ray lithography), medicine (radiotherapy, microsurgery with free electron laser, sterilization), power generation (inertial fusion, reactor fuel breeding), and fundamental science [1].

Conventional particle acceleration techniques typically employ radiofrequency cavities with electromagnetic fields to accelerate electrons. The upper bound of final particle energy is limited by material breakdown. The breakdown occurs when the electric field strength exceeds a certain critical value, known as the dielectric strength of the material. One of the ways to circumvent this restraint might be to generate strong electromagnetic fields in a plasma - a medium that is inherently ionized and, thus, in principle, immune to such damage. The electromagnetic field in plasmas suitable for particle acceleration can be generated by laser or particle beams.

Laser wakefield acceleration (LWFA) is a technique of electron acceleration in plasmas that utilizes ultrashort laser pulses. It was first proposed by Tajima and Dawson in 1979 [2]. Their idea lies in the generation of a plasma wave (so-called wakefield) by an ultrashort, ultraintense laser pulse in underdense (optically transparent) plasma. Background plasma electrons are injected into the plasma wave dragged by the laser pulse. Subsequently, they obtain large kinetic energy within very short distances. In contrast to conventional accelerators that generate accelerating electric fields up to about 100 MV/m [3], laser-based devices are able to reach even about 100 GV/m. Energy values that were typically obtained on a hundreds-of-meters distance are nowadays attainable on tens-of-centimeter scales with plasma-based accelerators [4].

During the last two decades, enormous progress has been achieved in the LWFA field, which goes hand in hand with the increasing availability and improvement of high-power laser machines. The maximum energy in LWFA was acquired in the Berkeley Lab with the high-power BELLA laser in 2018, producing an 8 GeV electron beam [4]. This value was obtained in a plasma only 20 cm long. This result is remarkably encouraging in order to pursue more effort in the advancement of LWFA and plasma-based accelerators, in general, pushing the boundaries toward achieving energy scales of the hundreds of gigaelectronvolts, or potentially even teraelectronvolts. In addition to GeV-level energies, laser wakefield accelerators are also capable of producing charge in the order of hundreds of pC [5–7], and transverse emittance in the order of 0.1 μm [8, 9]. However, it is challenging to achieve these properties simultaneously in one electron beam. Furthermore, the quality and

reproducibility still need to be tuned more properly based on a particular application. In addition, while the LWFA acceleration length is not affected by the material breakdown, it is limited by the depletion of the laser pulse and the dephasing between the electron beam and wakefield in the later acceleration times. Therefore, in general, more research, as well as technical development is needed on this topic. This is important not only for small-scale endeavors but also for very promising and highly expected large-scale research infrastructures, e.g., fully coherent hard X-ray free electron laser (XFEL), and a plasma-based electron-positron ($e^- - e^+$) collider.

This work addresses several contemporary challenges in LWFA. It is structured into two parts. Part I is devoted to the description of LWFA and related topics. It consists of seven chapters. In Chapter 1, laser systems that are typically used for LWFA are described. Chapter 2 introduces the generation of plasma by intense light and the propagation of ultrashort ultraintense laser pulses in plasma. In Chapter 3, the mechanism of LWFA generation is discussed in detail. Chapter 4 then focuses on the injection of electrons into the accelerating part of the wakefield. In Chapter 5, alternative laser-based and plasma-based methods of electron acceleration are outlined. Chapter 6 offers a summary of secondary X-ray sources from LWFA electrons. Part I concludes with Chapter 7, which provides an overview of the application perspectives of LWFA, and discusses current challenges within the field.

Part II focuses on five new ideas related to the LWFA field proposed in the frame of this thesis. The investigation was based primarily on the analysis carried out by numerical simulations. The part comprises two chapters. The first of them, Chapter 8, introduces the method of particle-in-cell simulations, which were utilized to analyze the concepts. Employed codes and methodology are described. Chapter 9 subsequently presents a concise list of the new concepts, accompanied by their brief descriptions and referencing previously published corresponding works. The first three schemes focus on the properties of the electron injection into the wakefield. The fourth project aims at the enhancement of the gain of betatron radiation - a femtosecond synchrotron-like high-energy photon source, a natural byproduct of the LWFA electrons. The fifth proposal is targeted at the electron counterpart in a planned plasma-based electron-positron collider. It describes a novel setup where laser-generated positrons are injected into a plasma channel for further acceleration. More comprehensive descriptions of these concepts can be then found in the corresponding publications within Appendix: Included publications. In Conclusion, the studies are summarized and outlooks for future research are provided.



Part I

Principle of laser wakefield acceleration (LWFA)

Chapter 1

Features of laser pulses used in LWFA

1.1 General properties of the laser light

A specific feature of lasers, compared to other light sources, is the capability of producing beams of highly coherent and collimated light. All photons of the laser light have a fixed-phase relationship with each other. Laser beams exhibit minimal divergence and can be focused into a very small spot.

The fundamental principle behind laser operation relies on stimulated emission. In this process, a photon first interacts with an excited atom, leading to its de-excitation and subsequent emission of another photon. The new photon is coherent with the initial one. Its energy is equal to the energy difference between the two states involved in the transition. Constructing a laser requires three essential components: an active medium where stimulated emission occurs, a pumping mechanism to generate population inversion, and an optical resonator.

Nowadays, lasers are used in a wide spectrum of fields. Each application has different requirements for the laser characteristics. Laser types can be categorized into distinct groups based on several factors, e.g., active medium (solid, semi-conductor, gas, liquid, plasma), types of transitions between energy levels (molecular, electron, nuclear), the pumping mechanism (optical, electrical discharge, electron beam,..), wavelength, or duration [10]. LWFA, in particular, employs laser pulses that are ultrashort (in the order of tens of femtoseconds) and ultraintense ($\gtrsim 10^{18}$ W/cm²). The generation of such pulses is discussed in the next section.

1.2 Generation of ultrashort ultraintense laser pulses

The femtosecond-scale duration of ultrashort laser pulses can be typically obtained by mode locking, where many longitudinal modes lase in a fixed-phase relationship (see Fig. 1.1a)). These pulses then propagate at the group velocity corresponding to its center frequency. Mode-locked lasers are able to produce a train of extremely short laser pulses separated by equal time intervals $2L/c$, where L is the distance between the reflector and output coupler of the cavity, and c is the speed of light [11]. There exist two fundamental approaches to mode locking: active mode locking and passive mode locking. In actively mode-locked lasers, an optical modulator in the laser cavity is able

to change the amplitude or the phase of light under external control [12]. Passive mode locking commonly relies on a saturable absorber inside the laser cavity [13, 14]. In passive mode locking, as the light pulses become shorter, they interact more effectively with the absorber, resulting in quicker adjustments to the pulse characteristics. Thus, this method enables the generation of shorter pulses compared to active mode locking [12]. On the other hand, passively mode-locked lasers tend to generate pulses with larger time jitter, attributable to the broader spectral linewidth of mode-beating [15].

As mentioned in Introduction, the LWFA technique was already proposed a few decades ago, back in the late 1970s, by Tajima and Dawson [2]. Despite the indisputable advantage of notably short acceleration distances, its experimental exploration remained unfeasible at the time. This was primarily due to the requirement of simultaneous ultrashortness and ultraintensity of laser pulses. By that time, nearly two decades had passed since Theodore Maiman's construction of the first laser in 1960 [16]. While mode-locking has been available since 1964 [17, 18], the rapid increase in intensity stopped a few years after its inception. This was mainly due to the fact that high intensity causes damage to optical components. As a consequence, scientists were not able to get above the threshold of $\sim 10^{15}$ W/cm².

The breakthrough came with the invention of chirped pulse amplification (CPA) by Donna Strickland and Gérard Mourou in 1985 [19]. CPA revolutionized the field by avoiding the damage to optical components caused by the high energy flux during the amplification of short laser pulses. The principle of this technique is depicted in Fig. 1.1b). First, an ultrashort laser pulse is conventionally produced in a laser oscillator. For CPA, it is important that the pulse is not monochromatic but has a broad spectrum of wavelengths. This can be achieved by a proper choice of a lasing medium. In the regime of pulse durations below 100 fs, titanium-doped sapphire (Ti:Sapphire) is mostly used. Ti:Sapphire lasers can operate in continuous wave regimes at extremely narrow linewidths tunable over a wide range that spans from 680 to 1100 nm [20]. They lase most efficiently near 800 nm [21]. Moreover, they have excellent thermal conductivity, alleviating thermal effects even for high laser powers and intensities [21].

The ultrashort pulse coming from the oscillator is then stretched (chirped) in time through a dispersive optical element. As a consequence, the intensity of the laser pulse is decreased. Afterward, this pulse, with its dispersed spectrum and extended duration, propagates into an amplifier. Due to the lower intensity of the chirped pulse, the amplifier is not damaged and boosts the energy of each wavelength component. Following amplification, the pulse travels into a compressor, achieving back the recombination of the frequencies with ultrashort duration but, now, with the amplified intensity.

CPA has opened doors for many possible applications of ultraintense pulses of duration on the femtosecond scale, including LWFA. Since the discovery, the maximum achievable laser intensity has been progressively increasing. The current world record in laser intensity reached in South Korea in 2021 is in the 10^{23} W/cm² range [22]. The significance of CPA was awarded with the Nobel Prize in 2018 [23].

1.3 Gaussian laser beams

In LWFA, laser beams with the amplitude envelope given by a Gaussian function are typically used. The Gaussian beams can be focused into a very intense spot, and

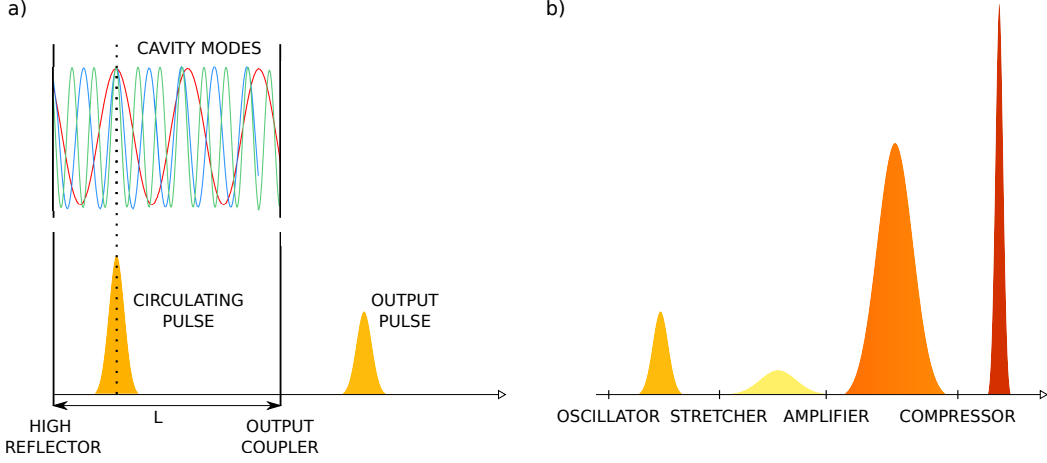


Figure 1.1: *Principle of mode locking and CPA.* a) Mode locking: Longitudinal modes in the cavity (red, blue, green) are constructively interfering with one another, producing the circulating short laser pulse. The circulating pulse is reflected between the high reflector and the output coupler, distant by L . The output pulse is generated periodically through the coupler in the time intervals $2L/c$. b) CPA: The short pulse from the oscillator is gradually stretched, amplified, and compressed, generating an ultrashort ultraintense laser pulse.

the Gaussian profile is preserved during the diffraction. Beams in LWFA usually also have a Gaussian profile in the temporal domain (i.e., they are also Gaussian pulses). In this work, if not stated otherwise, the propagation of the laser pulse is put in the x direction, and in the case of linear polarization, the wave is polarized in the y direction.

The electric field of a laser beam with a spatiotemporal Gaussian profile that moves in free space in the x direction and is linearly polarized in the y direction is given by [24]

$$\begin{aligned} \mathbf{E}_L(x, r, t) = & E_{L0} \frac{w_0}{w(x)} \exp \left[-2 \ln(2) \frac{\left(t - \frac{r^2}{2cR(x)} - \frac{x}{c} \right)^2}{\tau_L^2} \right] \exp \left[-\frac{r^2}{w^2(x)} + 2 \ln(2) \frac{r^4}{\tau_L^2 \omega_L^2 w^4(x)} \right] \\ & \times \exp \left[i\omega_L \left(1 - 4 \ln(2) \frac{r^2}{\tau_L^2 \omega_L^2 w^2(x)} \right) \left(t - \frac{r^2}{2cR(x)} - \frac{x}{c} \right) \right] \exp [i\psi(x)] \hat{\mathbf{y}}. \end{aligned} \quad (1.1)$$

Here, $r = \sqrt{y^2 + z^2}$ is a radial coordinate, t is time, τ_L is the duration of the pulse at full width at half of maximum (FWHM) of the intensity, E_{L0} is an amplitude, and $\hat{\mathbf{y}}$ is a unit vector in the y direction. Frequency ω_L is the carrier frequency of the pulse (the center frequency of the spectrum). The beam radius

$$w(x) = w_0 \sqrt{1 + \frac{x^2}{x_R^2}} \quad (1.2)$$

is the value at which the field falls to $1/e$ of its axial value, specified at a distance x from the beam focal plane. The beam waist w_0 is the radius measured when the beam is in

its focus ($x = 0$). In LWFA, w_0 is typically in the order of a few microns up to a few tens of microns. Value

$$x_R = \frac{\pi w_0^2}{\lambda_L} \quad (1.3)$$

is known as the Rayleigh length, where λ_L is the laser wavelength. Rayleigh length is the distance from the focus where the beam radius is increased by $\sqrt{2}$, and, consequently, the area by a factor of 2.¹ The radius of curvature of the wavefronts

$$R(x) = x \left(1 + \frac{x_R^2}{x^2} \right) \quad (1.4)$$

as well as phase

$$\psi(x) = \arctan \left(\frac{x}{x_R} \right) \quad (1.5)$$

also depend on the Rayleigh length. The intensity of the beam with a spatio-temporal Gaussian profile can be analogously written as

$$I(x, r, t) = |\mathbf{E}_L(x, r, t)|^2 = I_0 \frac{w_0^2}{w^2(x)} \exp \left[-4 \ln(2) \frac{\left(t - \frac{r^2}{2cR(x)} - \frac{x}{c} \right)^2}{\tau_L^2} \right] \\ \times \exp \left[-\frac{2r^2}{w^2(x)} + 4 \ln(2) \frac{r^4}{w^4(x) \tau_L^2 \omega_L^2} \right], \quad (1.6)$$

where $I_0 = E_{L0}^2$ is the maximum intensity. The total power and energy of the Gaussian beam are then

$$P_0 = \pi \frac{I_0 w_0^2}{2}, \quad (1.7)$$

and

$$\mathcal{E}_L = \frac{1}{2} \sqrt{\frac{\pi}{\ln(2)}} P_0 \tau_L, \quad (1.8)$$

respectively. Laser strength

$$a_0 = 0.855 \lambda_L [\mu\text{m}] \sqrt{I_0 [10^{18} \text{ W/cm}^2]} \quad (1.9)$$

is a parameter frequently used to describe the intensity of the laser beam. It corresponds to the maximum value of normalized vector potential $\mathbf{a} = e\mathbf{A}/(m_e c^2)$, where the vector potential \mathbf{A} is given by $\mathbf{E}_L = -\partial\mathbf{A}/\partial t$, and e and m_e are the electron absolute charge and mass, respectively.

The Gaussian spatio-temporal laser profile is routinely used in analytical and simulation studies of the LWFA process. However, in realistic experimental conditions, the profile might significantly deviate from an ideal Gaussian profile [25]. There can be several causes of discrepancies, e.g., laser halo [26], or comatic aberrations [27]. The laser profile defects are imprinted in the quality of the produced electron beam. More realistic laser

¹Note that instead of x_R , the symbol z_R is typically used for the Rayleigh length. For consistency in this work, x_R was chosen to express the Rayleigh length instead of z_R because the laser beam propagates in the x direction here.

beam distributions can be obtained by measuring experimental focal spot and wavefront. These data can be subsequently reconstructed and employed in simulations, achieving better simulation-experiment comparison [25, 28].

In addition to Gaussian beam profiles, some other options have been proposed to alternate typical LWFA structure, such as a Laguerre-Gaussian beam [29, 30] with a characteristic donut-like shape that can result in acceleration of a ring-shaped electron beam [29, 30], or even an externally on-axis injected positron beam [29].

■ 1.4 Typical features of the laser beams used in LWFA

To summarize the properties of laser beams used in LWFA, these beams typically have an ultrashort duration (ranging from a few fs to tens of fs), and they are focused into a spot size of several microns, reaching ultrahigh intensity ($\gtrsim 10^{18}$ W/cm²). Their shape is commonly approximated by a Gaussian spatio-temporal profile. They operate at the wavelength of ~ 800 nm. Consequently, laser systems are typically Joule-class and reach peak powers in the range of TWs to PWs. Their repetition rate is about 1–10 Hz [31].

As an example, the current LWFA record 8 GeV electron beam [4] has been achieved at the Ti:sapphire-based BELLA laser system [32] with a peak laser power of 850 TW, laser energy at the focal location 31 J, $a_0 \approx 2.2$, $w_0 \approx 60$ μm , FWHM duration $\tau_L \approx 35$ fs, and central laser wavelength $\lambda_L \approx 815$ nm with spectral width 40 nm. The repetition rate of the system was 1 Hz.

In this chapter, the properties of laser beams that are typically utilized in LWFA experiments have been summarized. In the next chapter, we discuss the ionization of matter triggered by ultraintense light.

Chapter 2

Field ionization and plasma generation

The outcome of the interaction between laser light and matter is significantly influenced by several key factors, including laser parameters such as wavelength, intensity, or spot size characteristics, as well as the properties of the material, for instance, its transparency to laser light. In this chapter, we will discuss how the significance of matter ionization increases with increasing intensity of the impinging light. This ionization process, driven by high-intensity lasers, results in a rapid formation of plasma, through which the laser pulse subsequently propagates.

If the intensity of laser light interacting with an atom is relatively low ($< 10^{10}$ W/cm²), electrons in the atom oscillate linearly, at the same frequency as the laser. As the laser intensity increases, electrons are stripped from atoms by ionization [33]. If the intensity overcomes

$$I_a = 3.51 \times 10^{16} \text{ W/cm}^2, \quad (2.1)$$

ionization is guaranteed for any target material. At this value, known as the atomic intensity, the laser field matches the binding strength of the electron to the atom [34]. Hence, in the case of LWFA beams with intensity $\gtrsim 10^{18}$ W/cm², field ionization is unavoidable.

2.1 Types of field ionization

The ionization process already starts at intensities much below the threshold of atomic intensity I_a (2.1). The energy necessary for ionizing an atom can be acquired by absorbing either a single photon (photoelectric effect) or a higher number of photons (multiphoton ionization, see Fig. 2.1a). The cross-section (probability) of the multiphoton event is lower for a higher number of photons. Nevertheless, the multiphoton ionization rate rapidly increases with laser intensity and becomes very significant at intensities above 10^{10} W/cm².

It is also possible that the atom absorbs an excess amount of energy beyond what is required for ionization. In this case, above-threshold ionization occurs, and more photons than are necessary for the electron to be released from the atom are absorbed (see Fig. 2.1b). The redundant energy is transformed into the kinetic energy of the electron.

If the laser intensity gets closer to I_a , tunneling ionization [35] becomes substantial. As the laser field becomes strong enough to distort the Coulomb field experi-

enced by the electron, the height of the potential barrier drops significantly. Therefore, the electron can tunnel through the barrier with some finite probability and escape from the atom [34], as depicted in the illustrative scheme in Fig. 2.1c). If the potential is suppressed to such an extent that it becomes lower than the ionization potential, the electron escapes from the atom spontaneously, and we talk about barrier-suppression ionization (Fig. 2.1d).

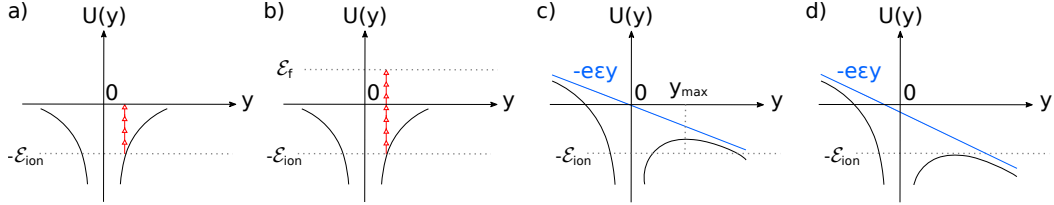


Figure 2.1: *Field ionization: multiphoton, above-threshold, tunneling, and barrier-suppression ionization.* a) Multiphoton ionization: the electron gains ionization energy \mathcal{E}_{ion} by simultaneously absorbing several photons (red arrows) to overcome the potential energy barrier $U(y) = -\mathcal{E}_{\text{ion}}$. b) Above-threshold ionization: the electron gains energy $\mathcal{E}_{\text{ion}} + \mathcal{E}_f$. Extra energy \mathcal{E}_f is transformed into the kinetic energy of the electron. c) Tunneling ionization: Coulomb potential is modified by stationary homogenous electric field ε (for simplicity). For $y \gg y_{\text{max}}$, the barrier is lower than $U(y) = -\mathcal{E}_{\text{ion}}$. As a consequence, the electron can tunnel through the barrier with some finite probability. d) Barrier-suppression ionization: ε is so strong that $U(y) < -\mathcal{E}_{\text{ion}}$ for any $y > 0$, and the electron can escape spontaneously. The illustrations are based on Ref. [34].

2.2 Creation of plasma by ultraintense laser fields

It is now clear that once the laser intensity is ultrahigh, electrons are immediately stripped from atoms, dominantly by the tunneling or barrier-suppression ionization, and interact with the laser field. The exact time of tunneling ionization has remained an unresolved, controversial topic. While some publications support the idea of instantaneous ionization, e.g., Ref. [36], some studies have also suggested that the process can have a finite time on an attosecond scale, e.g., Ref. [37].

Regardless of whether the ionization time is instantaneous or extends over attosecond or subattosecond scales, compared to the duration of femtosecond laser beams, it is negligible. For instance, one period of a Ti:sapphire-generated laser pulse with $\lambda_L = 0.8 \mu\text{m}$ has a duration of around 2.7 fs. As a consequence, an ultraintense laser beam propagating in a gaseous medium ionizes the matter immediately as it passes by, leaving free ions and electrons behind. The level of ionization depends on the particular material.

As a consequence, the laser pulse changes the state of the matter into plasma. Plasma is defined as a quasi-neutral system of freely-moving charged particles where the collective behavior of their fields plays an important role [38]. Plasma can also contain neutral particles. Quasi-neutrality expresses the equality of the number of positively and negatively charged particles in every macroscopic volume [39]. The collective behavior means that plasma generates electromagnetic fields and also reacts to external electromagnetic fields. The quantitative scale of a decrease in a local charge is called Debye length. It is defined

as

$$\lambda_D = \sqrt{\frac{\varepsilon_0 k_B T_e}{e^2 n_e}}, \quad (2.2)$$

where ε_0 is vacuum permittivity, k_B is Boltzmann constant, n_e is electron density, and T_e is electron temperature. Debye length describes a distance, where the potential of a local charge density perturbation is reduced to $1/e$ of its initial value. Here we neglect the contribution of ions as they react much slower to fluctuations of charge.

The electron plasma frequency, defined as

$$\omega_p = \sqrt{\frac{e^2 n_e}{\varepsilon_0 m_e}}, \quad (2.3)$$

is a natural electron oscillation frequency in plasma caused by the displacement of electrons due to the static ion background. The field created by these ions tries to restore the charge neutrality. As a consequence, electrons oscillate back and forth with frequency ω_p [40]. Plasma wavelength can be then written as

$$\lambda_p = \frac{2\pi c}{\omega_p} = 2\pi c \sqrt{\frac{\varepsilon_0 m_e}{e^2 n_e}}. \quad (2.4)$$

It is also possible to define ion plasma frequency similarly to the one of electrons. However, this frequency is much lower due to the high ion mass. For instance, a single proton is already $1836\times$ heavier than an electron. Due to this fact, ions cannot take part in high-frequency processes with ultrashort laser pulses, and they act like a static background for fast electrons.

The dispersion relation for an electromagnetic wave, e.g., a laser pulse, passing through plasma is expressed as

$$\omega^2 = \omega_p^2 + c^2 k_L^2, \quad (2.5)$$

where k_L is the magnitude of wave vector \mathbf{k}_L . One can see that k_L becomes imaginary if the plasma frequency exceeds the laser frequency. In such a case, the wave cannot propagate into plasma. Critical density is the density of electrons corresponding to frequency $\omega = \omega_p$. It can be derived that

$$n_c = \frac{\varepsilon_0 m_e \omega^2}{e^2}. \quad (2.6)$$

When $n_e < n_c$, the plasma is transparent to the laser light, and in such a case, it is called underdense plasma. For $n_e > n_c$, the plasma is not transparent to the laser light, and it is called overdense plasma. Plasma index of refraction can be written as

$$\eta = \sqrt{1 - \frac{\omega_p^2}{\omega^2}} = \sqrt{1 - \frac{n_e}{n_c}}. \quad (2.7)$$

As an example, $n_c = 1.74 \times 10^{21} \text{ cm}^{-3}$ for the central wavelength of Ti:Sapphire laser $\lambda_L = 0.8 \text{ }\mu\text{m}$. Most LWFA experiments with low- Z gas work with densities in the range from about 10^{17} cm^{-3} up to about 10^{19} cm^{-3} , i.e., in underdense plasma. In the next section, some important features of the propagation of ultraintense laser pulses of ultrashort duration in plasmas are discussed.

2.3 Propagation of ultraintense laser pulses in plasma

The group velocity of the laser pulse in underdense plasma is given by

$$v_{Lg} = c\sqrt{1 - \frac{\omega_p^2}{\omega_L^2}}. \quad (2.8)$$

For example, for $n_e = 10^{18} \text{ cm}^{-3}$, $v_{Lg} \approx 0.9997c$, which is close to the speed of light. When an electron with momentum \mathbf{p} and velocity \mathbf{v} interacts with the electromagnetic field of the laser, the Lorentz equation of electron motion can be written as

$$\frac{d\mathbf{p}}{dt} = -e[\mathbf{E} + (\mathbf{v} \times \mathbf{B})]. \quad (2.9)$$

Here, \mathbf{E} and \mathbf{B} are the electric and magnetic fields, respectively. For laser strength $a_0 \ll 1$, i.e., low subrelativistic fields, the solution of the equation is an oscillation of the electron at the laser frequency along a straight line parallel to the polarization vector. In such a case, $\mathbf{v} \times \mathbf{B}$ is negligible. For $a_0 \gtrsim 1$, the regime becomes relativistic. The electron oscillation velocity approaches c , and then the $\mathbf{v} \times \mathbf{B}$ component of the Lorentz force must be taken into account. For example, for $\lambda_L = 0.8 \text{ }\mu\text{m}$, $a_0 = 1$ which separates these two regimes, corresponds to the intensity of $I_0 = 2.1 \times 10^{18} \text{ W/cm}^2$.

In addition, in a non-uniform oscillating electromagnetic field, such as the field of a Gaussian spatiotemporal beam, particles also experience so-called ponderomotive force. Ponderomotive force expels the particles out of the high-intensity regions, and pushes them towards the area of the weaker field strength. The force can also be interpreted as radiation pressure which the intense laser pulse exerts on background plasma electrons [41].

In the subrelativistic regime $a_0 \ll 1$, the leading-order electron fluid motion is the quiver momentum $\mathbf{p}_q = m_e c \mathbf{a}$ [42]. By adding a perturbation $\delta\mathbf{p}$ to the electron momentum $\mathbf{p} = \mathbf{p}_q + \delta\mathbf{p}$, the net second-order force over one laser cycle, which we call ponderomotive force, is given by

$$\mathbf{F}_{\text{LP}} = \left\langle \frac{d\delta\mathbf{p}}{dt} \right\rangle = - \left\langle \left[\left(\frac{\mathbf{p}_q}{m_e} \cdot \nabla \right) \mathbf{p}_q + \mathbf{p}_q \times (c\nabla \times \mathbf{a}) \right] \right\rangle = -m_e c^2 \nabla \left\langle \frac{a^2}{2} \right\rangle, \quad (2.10)$$

where a is the magnitude of \mathbf{a} . Note that a similar derivation can analogously be applied to ions. As can be seen from Eq. (2.10), the force is inversely proportional to the mass, thus, the ponderomotive force acting on ions is significantly lower in comparison to electrons.

In the case of relativistic regime $a_0 \gtrsim 1$, generalized ponderomotive force [42–45] can be expressed with the Lorentz factor γ averaged over a cycle $\langle \gamma \rangle$:

$$\mathbf{F}_{\text{NP}} = -m_e c^2 \nabla \langle \gamma \rangle. \quad (2.11)$$

Ponderomotive force locally changes electron density. The region of the maximum refractive index is located on the optical axis. This distribution of the refractive index acts on the pulse as a positive lens [46]. Thus, self-focusing occurs due to the increase of refractive index (2.7) at the regions of high intensity. If the power of laser P satisfies $P \gg P_c$, where

$$P_c = 17.5 \frac{n_c}{n_e} \text{ GW} \quad (2.12)$$

is the critical power, the laser beam would collapse to a zero radius width at a distance $x \approx x_R(P/P_c)^{-1/2}$. In reality, additional defocusing occurs, or paraxial approximation breaks down, and collapsing does not occur [34].

If $P = P_c$, the relativistic self-focusing and diffraction compensate, and the beam propagates with a radius equal to its waist. This phenomenon is very advantageous in order to sustain high-intensity fields for laser-based acceleration, as it suppresses diffraction. Otherwise, diffraction would cause a rapid decrease in the peak laser intensity during its propagation through an underdense target.

In this chapter, the topics of field ionization and propagation of laser beams in underdense plasmas were concisely summarized. The next chapter will focus on the generation of laser wakefield.

Chapter 3

Generation of laser wakefield

In the frame of this chapter, the generation of laser wakefield and different regimes of LWFA with respect to their intensity are described. Before that, a brief introduction to plasma sources used in LWFA is presented.

3.1 Plasma sources

As mentioned previously, LWFA is based on the generation of a plasma wave, referred to as wakefield, provided by an ultrashort laser pulse propagating in underdense plasma. As the laser pulse propagates through the plasma, it drags the wave behind. The ultraintense pulse propagates inside a low- Z gas or a preionized underdense plasma. In the former case, the plasma can be created instantaneously by the laser pulse itself, when it travels through the plasma, as described in Chapter 2. In the latter case, the gas can be already preionized by another pulse preceding the main drive pulse, which generates the wakefield. The matter can be also ionized by another method than field ionization, e.g. by discharge [47]. The acceleration can take place in a gas jet [48–51], a gas cell [52–57], or a capillary [4, 58–62].

Gas jets produce uniform density by a supersonic flow through a conical nozzle. They are easy to operate with but they generally have quite poor shot-to-shot reproducibility of the density profile [54]. A gas cell is statically filled with gas, with an entrance aperture for the laser pulse on one side, and an exit on the other side. They can provide stability [53] and produce very uniform density profiles at low densities [54]. Gas capillaries are long and very narrow tubes filled with gas. They typically have a diameter in the order of 100 μm [54]. For instance, in the experiment with the 8 GeV LWFA electrons, a capillary with a diameter of 0.8 mm and a length of 20 cm was employed [4]. The plasma in capillaries can be, for example, produced by discharge. In the capillary discharge, the current ionizes matter, and the plasma is heated via Ohmic heating. As the plasma expands, the density minimum is formed on the capillary axis [63].

3.2 Wakefield generation

When a laser pulse propagates inside a self-generated or preformed plasma, it excites oscillations along its path. This is due to the ponderomotive force (Eq. 2.10 and Eq. 2.11 for $a_0 \ll 1$ and $a_0 \gtrsim 1$, respectively), which drives the electrons away from regions of high intensity toward regions of lower intensity in the laser pulse. As a consequence, a local

charge nonuniformity arises. A strong Coulomb field is generated, attracting electrons and causing them to return to the density depression [64]. Subsequently, the ponderomotive force pushes electrons away from the strong field region again, which generates another density depression. Under these conditions, electrons undergo back-and-forth motion, resulting in the formation of a plasma wave that co-propagates with the laser pulse. Its phase velocity is approximately given by the laser pulse group velocity v_{Lg} expressed in Eq. (2.8). Therefore, we will further use notation v_{Lg} for both the wake phase velocity and the laser pulse group velocity in this work. As mentioned previously, ions are far more massive than electrons, hence, they remain unaffected by the ultrashort pulse and form a static background due to their large inertia. If some of the background plasma electrons are injected into the wakefield with proper initial conditions, they may sustain in phase with the longitudinal electric field and be accelerated to high energies. The methods of the electron injection will be described in Chapter 4.

In general, LWFA can operate either in the linear regime ($a_0 \ll 1$), or in the nonlinear regime ($a_0 \gtrsim 1$). In the next two subsections, we respectively describe the characteristics of each regime.

■ 3.2.1 Linear regime

The analytical formulas for the plasma wave (wakefield) generated by the ponderomotive force (2.10) of a laser pulse in the linear regime can be obtained by approximating plasma as a cold electron fluid with mean electron velocity \mathbf{u}_e . The description of the wakefield with potential Φ and electric field $\mathbf{E} = -\nabla\Phi$ can be derived from the following equations:

- the momentum conservation equation

$$\frac{\partial \mathbf{u}_e}{\partial t} = -\frac{e}{m_e} \mathbf{E} - c^2 \nabla \frac{\langle a^2 \rangle}{2}, \quad (3.1)$$

- Poisson's equation

$$\nabla^2 \Phi = \frac{en_e}{\varepsilon_0}, \quad (3.2)$$

- and continuity equation

$$\frac{\partial n_e}{\partial t} + \nabla \cdot (n_e \mathbf{u}_e) = 0. \quad (3.3)$$

It is now assumed that $n_e = n_{e0} + \delta n_e$, where n_{e0} is an initial uniform plasma density and δn_e is a small perturbation introduced by the electrostatic wake Φ . By differentiating continuity equation (3.3) with respect to t we get

$$\frac{\partial^2}{\partial t^2} \left(\frac{\delta n_e}{n_{e0}} \right) + \nabla \cdot \frac{\partial \mathbf{u}_e}{\partial t} = 0. \quad (3.4)$$

Putting Eq. 3.1 into Eq. 3.4, we then obtain the expression for the plasma wave density modulations triggered by the ponderomotive force [65–67]:

$$\left(\frac{\partial^2}{\partial t^2} + \omega_p^2 \right) \frac{\delta n_e}{n_{e0}} = c^2 \nabla^2 \frac{\langle a^2 \rangle}{2}. \quad (3.5)$$

For wake potential Φ , expressed by Poisson's equation (3.2), the equation can be written analogously:

$$\left(\frac{\partial^2}{\partial t^2} + \omega_p^2\right)\phi = \frac{\omega_p^2 \langle a^2 \rangle}{2}, \quad (3.6)$$

where the potential was normalized to $\phi = e\Phi/(m_e c^2)$. Solutions of these equations for the density and electric field of the wave generated at frequency ω_p are

$$\frac{\delta n_e}{n_{e0}} = \frac{c^2}{\omega_p} \int_0^t \nabla^2 \frac{\langle a^2(\mathbf{r}, t') \rangle}{2} \sin[\omega_p(t - t')] dt', \quad (3.7)$$

$$\frac{\mathbf{E}}{E_0} = -c \int_0^t \nabla^2 \frac{\langle a^2(\mathbf{r}, t') \rangle}{2} \sin[\omega_p(t - t')] dt', \quad (3.8)$$

respectively, where

$$E_0 = \frac{cm_e \omega_p}{e}. \quad (3.9)$$

The wakefield can be expressed as a simple sinusoidal wave with a phase velocity given by the laser group velocity v_{Lg} from Eq. 2.8) [42]. Eqs. 3.7, and 3.8 are valid for the magnitudes of electric field $E \ll E_0$. E_0 represents the cold nonrelativistic wave breaking field [68] and expresses the maximum possible amplitude achievable at the particular plasma density. The formulas also imply that the wakefield is generated most efficiently when the envelope scale length, characterized by the gradient of $\langle a^2 \rangle$, is in the order of λ_p [42].

An example of longitudinal electric field E_x of the wakefield in the linear regime is shown in Fig. 3.1a) for a laser pulse with $a_0 = 0.3$. This figure, obtained from a simulation, clearly shows alternating areas of the electric field, where negative E_x corresponds to the accelerating part and positive E_x to the decelerating part for electrons. The density variations in plasma, depicted in Fig. 3.1b) have minor sinusoidal perturbations around the initial uniform plasma density $n_{e0} \sim 0.0029n_c$. Note that the simulation also captures the 3D evolution of the laser beam, including its divergence.

In addition to the longitudinal field of the wakefield, transverse electromagnetic fields are also generated [42]. In the linear wakefield, there is a region in each wake period equal to $\lambda_p/4$, where the forces acting on particles are simultaneously longitudinally accelerating and radially (on-axis) focusing. This is beneficial for the acceleration process because the electron beam in this area can stay naturally compressed around the acceleration axis during the acceleration process.

■ 3.2.2 Nonlinear regime

In the nonlinear regime of LWFA, where $a_0 \gtrsim 1$, the plasma wave becomes nonlinear. In such a case, the density change cannot be approximated by small perturbation δn_e . The solution of the nonlinear wakefields has been derived for the 1D geometry [70–76]. In the realistic 3D nonlinear regime, no exact analytical solution exists and the process has been mostly studied numerically.

In the 1D regime, equations for the wakefield can be derived assuming that the drive laser pulse does not evolve during the propagation. All the quantities describing the fluid and laser motion are only a function of $\xi = x - v_{Lg}t$, which is a variable co-moving

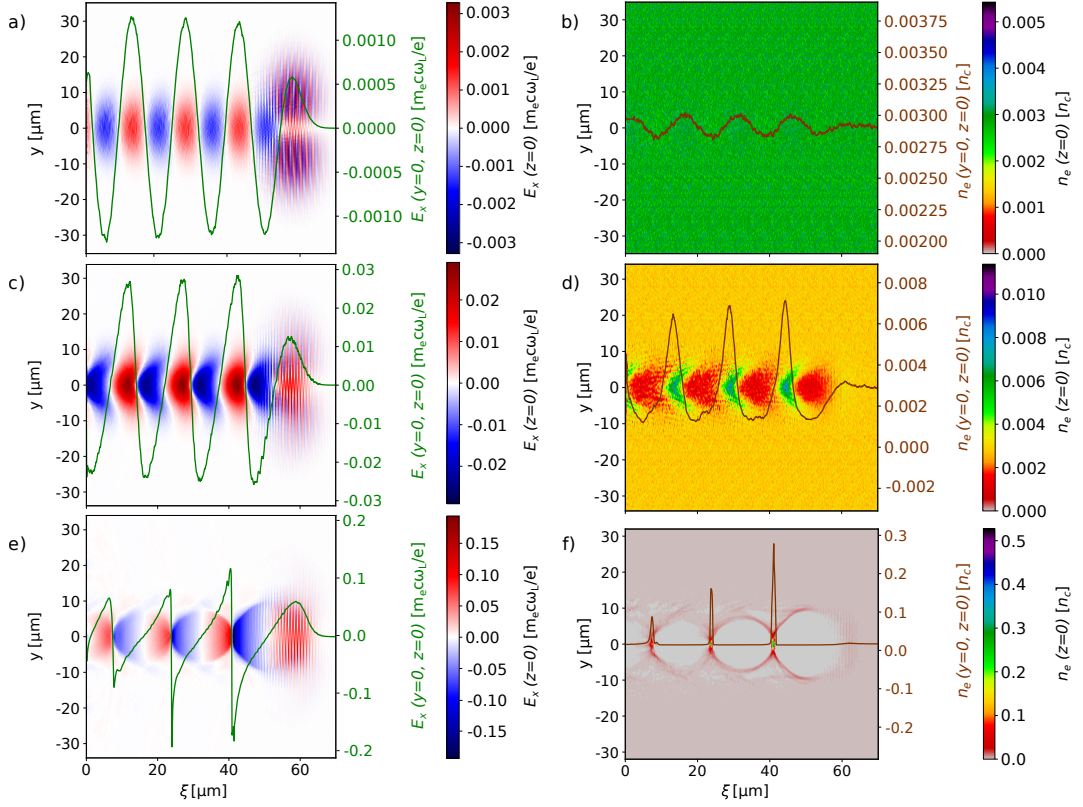


Figure 3.1: Longitudinal electric field and density profiles in the linear, weakly nonlinear, and bubble regime of LWFA. The left column shows longitudinal electric fields E_x on the axis $z = 0$ in the a) linear regime, c) weakly nonlinear, and e) bubble regime. The green line depicts E_x on the axis $y = 0$, and $z = 0$. The right column shows corresponding plasma density n_e profiles on the axis $z = 0$ in the b) linear regime, d) weakly nonlinear, and f) bubble regime. The red-brown line depicts n_e on the axis $y = 0$, and $z = 0$. The 3D simulations were performed in particle-cell-code Smilei [69]. The laser pulse is moving in the positive ξ direction, which is a coordinate co-moving with the laser pulse. The profiles are shown after 0.85 ps of the pulse propagation in plasma. The plasma had initially a uniform profile with a density of $n_{e0} = 5 \times 10^{18} \text{ cm}^{-3} \sim 0.0029 n_c$ and a 50- μm -long linear density increase from the zero value at the plasma entrance. The laser strengths have values: $a_0 = 0.3$ in the linear regime a) and b), $a_0 = 1.25$ in the weakly nonlinear regime c) and d), and $a_0 = 4$ in the nonlinear regime e) and f). Other parameters of the laser beam, linearly polarized in the y direction, are: $w_0 = 9.5 \mu\text{m}$, $\lambda_L = 0.8 \mu\text{m}$, and $\tau_L = 24.7 \text{ fs}$.

with the laser pulse [71, 72]. The equation for the wake potential of the nonlinear plasma wave is then given by [74–76]

$$\frac{c^2}{\omega_p^2} \frac{\partial^2 \phi}{\partial \xi^2} = \gamma_{Lg}^2 \left[\beta_{Lg} \left(1 - \frac{1 + a^2}{\gamma_{Lg}^2 (1 + \phi)^2} \right)^{-1/2} - 1 \right]. \quad (3.10)$$

Here, $\beta_{Lg} = v_{Lg}/c$ and $\gamma_{Lg} = 1/\sqrt{1 - \beta_{Lg}^2}$. ϕ and a are dependent on ξ . In the limit

of $v_{Lg} \rightarrow c$, the equation 3.10 simplifies to [70–73]

$$\frac{c^2}{\omega_p^2} \frac{\partial^2 \phi}{\partial \xi^2} = \frac{1 + a^2}{2(1 + \phi)^2} - \frac{1}{2}. \quad (3.11)$$

Equations 3.10 and 3.11 do not longer contain a simple sinusoidal function, as in the case of the linear wake (Eq. 3.6). The nonlinear wakefield has a sawtooth-like profile [42]. The period of the plasma wave increases with amplitude, and the nonlinear wavelength of the plasma wave in the limit of $v_{Lg} \rightarrow c$ can be written as [70–73]

$$\lambda_{pN} = \begin{cases} \left(1 + \frac{3E_{\max}^2}{16E_0^2}\right) \lambda_p & \text{for } E_{\max}/E_0 \ll 1, \\ \frac{2}{\pi} \left(\frac{E_{\max}}{E_0} + \frac{E_0}{E_{\max}}\right) \lambda_p & \text{for } E_{\max}/E_0 \gg 1, \end{cases} \quad (3.12)$$

where E_{\max} is the peak electric field of the wakefield. The maximum attainable amplitude of the 1D nonlinear plasma wave using nonlinear relativistic cold fluid equations is equal to [77, 78]

$$E_{0NL} = \sqrt{2(\gamma_{Lg} - 1)} E_0. \quad (3.13)$$

It can be seen that for the maximum amplitude of a nonlinear plasma wave, it is possible to exceed the linear threshold E_0 given by Eq. (3.9). In warm plasma, where the electron distribution has a thermal spread about its mean fluid velocity, the pressure reduces the maximum wakefield amplitude [42].

In the 3D geometry, there is an additional radial influence on the wakefield wavelength when a usual Gaussian laser beam is utilized. The wavelength varies with the distance from the axis, i.e. $\lambda_{pN}(r)$. This is caused by the fact that the laser intensity is highest on the axis $r = 0$, generating the highest wakefield amplitude. The wake magnitude then gradually decreases with increasing r . As a consequence, its wavefronts are curved [42].

The nonlinear regime can be generally divided further into the weakly nonlinear regime where $a_0 \sim 1$ and the highly nonlinear (also bubble or blowout) regime. It is ambiguous what is the exact threshold between the two regimes. Here, we will assume the typically used threshold for the bubble regime $a_0 \gtrsim 2$, stated, e.g., in Ref. [79]. In the weakly nonlinear regime, the nonlinear features are already inevitably present. However, the period lengthening and wave steeping are not as strong as in the bubble regime and linear description can be sometimes sufficient to describe certain effects on electron beam parameters [80]. An example of the weakly nonlinear regime for $a_0 = 1.25$ is presented in Figs. 3.1 c) and d) for E_x and n_e , respectively. Compared to the linear regime in Figs. 3.1 a) and b), the maximum field is about a magnitude higher, and the on-axis field exhibits a steeper gradient. The curvature of the wavefronts is also present.

In the bubble regime, the radiation pressure of the laser pulse expels plasma electrons excessively radially outward. Consequently, ion cavities (bubbles) are left behind instead of a linear periodic plasma wave [81, 82]. Almost all the electrons are expelled and a narrow electron sheath around the bubble is formed. Studies are usually focused on the acceleration in the first bubble behind the laser pulse due to the fact that it has the highest acceleration gradient, and the term "bubble" is therefore commonly used only for this first ion cavity.

An example of a nonlinear E_x profile and n_e modulations in the bubble regime are depicted in Fig. 3.1e) and Fig. 3.1f), respectively, for $a_0 = 4$. Behind the laser pulse,

a cavity without electrons (bubble) is formed. It has a typical sphere-like shape and is surrounded by a dense electron sheath. E_x has a very steep profile. The on-axis density profile also shows density spikes at the rear part of the bubble and the rear parts of the subsequent cavities (2nd and 3rd wakefield periods).

Although there is no proper nonlinear description of a 3D wakefield, a simplified phenomenological model of the bubble fields has been proposed [81, 82]. In this model, the bubble is approximated as a uniformly charged ion sphere. The fields inside the bubble can be derived using the Maxwell's equations:

$$\begin{aligned}\nabla \times \mathbf{E} &= -\frac{\partial \mathbf{B}}{\partial t}, & \nabla \cdot \mathbf{B} &= 0, \\ \nabla \times \mathbf{B} &= \mu_0 \mathbf{j} + \frac{1}{c^2} \frac{\partial \mathbf{E}}{\partial t}, & \nabla \cdot \mathbf{E} &= \frac{\rho_c}{\epsilon_0}.\end{aligned}\quad (3.14)$$

Here, μ_0 is the vacuum permeability. Charge density and current density satisfy $\rho_c = -en_e$ and $\mathbf{j} = -en_e \mathbf{p}/(m_e \gamma)$, respectively. We first calculate normalized scalar potential ϕ and normalized vector potential $\mathbf{a} = (a_x, a_y, a_z)$ inside the bubble, using gauge $a_x = -\phi$. Subsequently, the wakefield potential, expressed as $\varphi = a_x - \phi$, is employed in the calculations. As a result, $\phi = -\varphi/2$ and $a_x = \varphi/2$. The following normalizations are used in the next derivation: time to ω_p^{-1} , lengths to c/ω_p , velocity to c , mass to m_e , charge to e , density to background plasma density n_{e0} , and electromagnetic fields to E_0 (Eq. 3.9). A tilde notation will be used for the normalized quantities, with the exception of \mathbf{a} , ϕ , and φ . Maxwell equations can be now rewritten using the potentials as

$$\begin{aligned}\Delta \varphi &= 1 - \tilde{n}_e \left(1 - \frac{\tilde{p}_x}{\gamma}\right) + \left(\frac{\partial}{\partial \tilde{t}} + \frac{\partial}{\partial \tilde{x}}\right) (\nabla \cdot \mathbf{a}) + \frac{1}{2} \frac{\partial}{\partial \tilde{t}} \left(\frac{\partial}{\partial \tilde{t}} - \frac{\partial}{\partial \tilde{x}}\right) \varphi, \\ \nabla \times \nabla \times \mathbf{a} &= -\tilde{n}_e \frac{\tilde{\mathbf{p}}}{\gamma} + \frac{\partial}{\partial \tilde{t}} \left(\frac{\nabla \varphi}{2} - \frac{\partial \mathbf{a}}{\partial \tilde{t}}\right),\end{aligned}\quad (3.15)$$

where \tilde{p}_x is the normalized electron momentum in the x direction. Assuming that all the quantities depend on $\tilde{\xi}$, a coordinate co-moving with the spherically symmetrical bubble, and neglecting the terms proportional to $\gamma L_g^{-2} \ll 1$, equations (3.15) are reduced to

$$\begin{aligned}\Delta \varphi &= \frac{3}{2}, \\ \nabla_{\perp} \frac{\partial \varphi}{\partial \tilde{\xi}} &= 0,\end{aligned}\quad (3.16)$$

where ∇_{\perp} is an operator $\nabla_{\perp} = (\partial/\partial \tilde{y}, \partial/\partial \tilde{z})$. The solution for the potential is then given by

$$\varphi(\tilde{\xi}, \tilde{y}, \tilde{z}) = \varphi_0 + \tilde{C} \left(\frac{\tilde{\xi}^2}{\tilde{r}_b^2} + \frac{\tilde{y}^2}{\tilde{r}_b^2} + \frac{\tilde{z}^2}{\tilde{r}_b^2} \right), \quad (3.17)$$

where \tilde{r}_b is a constant equal to the bubble radius, and \tilde{C} and φ_0 are constants that can be now obtained additionally. The potential satisfies the first equation in Eqs. (3.16) when $\tilde{C} = \tilde{r}_b^2/4$. The value of φ_0 can be derived from the potential of the bubble surface where it reaches its maximum value $\varphi(\tilde{\xi}^2 + \tilde{y}^2 + \tilde{z}^2 = \tilde{r}_b^2) = 1$. By this, we get $\varphi_0 = 1 - \tilde{r}_b^2/4$. Finally, the potential inside the bubble can be written as

$$\varphi(\xi, y, z) = 1 - \frac{\tilde{r}_b^2}{4} + \frac{1}{4} \left(\tilde{\xi}^2 + \tilde{y}^2 + \tilde{z}^2 \right) \quad (3.18)$$

The electric and magnetic fields inside the bubble can be now calculated as $\tilde{\mathbf{E}} = -\nabla\phi - \partial\mathbf{a}/\partial t$, and $\tilde{\mathbf{B}} = \nabla \times \mathbf{a}$. Reformulating them back to the non-normalized units, we get

$$\begin{aligned} E_x &= \frac{m_e\omega_p^2}{2e}\xi & B_x &= 0 \\ E_y &= \frac{m_e\omega_p^2}{4e}y & B_y &= \frac{m_e\omega_p^2}{4ce}z \\ E_z &= \frac{m_e\omega_p^2}{4e}z & B_z &= -\frac{m_e\omega_p^2}{4ce}y \end{aligned} \quad (3.19)$$

Longitudinal electric field E_x achieves its maximum at the front of the bubble with radius r_b , i.e. $\xi = r_b$. This is a placement of the central part of the laser driver. The minimum is reached at the back of the bubble $\xi = -r_b$. At this position, the electron experiences the highest acceleration gradient. The longitudinal electric field in the bubble changes linearly with the distance behind the driver. During the acceleration process, the electron bunch advances from the rear to the central part of the bubble, as its velocity exceeds v_{Lg} . Once the electron traverses the central region, the polarity of electric field reverses, initiating the phase of deceleration. The dephasing leads to the limitation of the maximum energy gained by electrons, as will be discussed in Section 3.3. In the bubble regime, a simultaneous accelerating and focusing area now covers the length of $\sim \lambda_p/2$ due to the steepness of the wave. This is in contrast with the linear regime, where it corresponds to only a quarter of the period.

A stable self-guiding of an intense short pulse without significant variations of the pulse profile over a few Rayleigh lengths is achieved if the following condition is satisfied [83]:

$$k_p w_0 \approx 2\sqrt{a_0}, \quad (3.20)$$

where k_p is the wakefield wavenumber. In such a case, the bubble radius satisfies [84]

$$r_b \approx 2\sqrt{a_0}/k_p. \quad (3.21)$$

Although there are many limitations to the spherical model, it sufficiently describes the basic principle of acceleration in the bubble. Several extensions of this model have been proposed, considering the influence of a thin electron sheath [85], or an elliptical shape of the bubble [86, 87]. In reality, other factors, such as the charge of the electron beam inside the bubble (so-called beam-loading effect) can also influence the bubble shape and cause deviations from value (3.21) [88].

As can be seen from Eqs. (3.19), the bubble exerts a linear force in the directions transverse to the pulse propagation. This focusing force can trigger transverse (betatron) oscillations of a relativistic electron with Lorentz factor γ along the bubble axis with betatron frequency

$$\omega_\beta = \frac{\omega_p}{\sqrt{2\gamma}}, \quad (3.22)$$

leading to the production of X-ray radiation. This phenomenon will be described in Chapter 6.

3.3 Dephasing length and depletion length

The dephasing and depletion lengths are crucial terms in the theory of laser wakefield acceleration. The velocity of an electron trapped in a wakefield and accelerated along the direction of the wave propagation gradually increases and approaches the speed of light. The electron eventually outruns the accelerating part of the plasma wave with effective focusing, i.e., $\sim \lambda_p/4$ and $\sim \lambda_p/2$ in the linear and nonlinear regimes, respectively. As a consequence, the electron moves into the decelerating region of the plasma wave and becomes dephased. Hence, the energy gained by the accelerated electron is limited [42]. Dephasing length L_d is an effective acceleration length, specified as the maximum length over which electrons can be accelerated.

The most efficient use of laser energy is achieved around the density where dephasing length is approximately equal to depletion length L_{pd} [89]. The depletion length refers to the distance over which a laser pulse loses half of its energy as a result of wakefield excitation. For instance, for the 3D nonlinear regime, estimates of the dephasing length and depletion length are [83]

$$L_d \approx \frac{4}{3} \frac{\omega_L^2 \sqrt{a_0}}{\omega_p^2 k_p}, \quad (3.23)$$

and

$$L_{pd} \approx c\tau_L \frac{\omega_L^2}{\omega_p^2}, \quad (3.24)$$

respectively. An estimate of the maximum energy gained by accelerated electrons in the 3D nonlinear regime is given by [83]

$$\mathcal{E}_{\max} \approx 0.34 a_0 \frac{\omega_L^2}{\omega_p^2} [\text{MeV}]. \quad (3.25)$$

As an example, when the laser pulse has $\lambda_L = 0.8 \mu\text{m}$, $a_0 = 4$, and $\tau_L = 24.7 \text{ fs}$, then by setting $n_e = 3.6 \cdot 10^{18} \text{ cm}^{-3}$, we reach $L_d = L_{pd} \approx 3.5 \text{ mm}$ and $\mathcal{E}_{\max} \approx 650 \text{ MeV}$.

In this chapter, the generation of laser wakefield was summarized, distinguishing the features of linear and nonlinear regimes. The concepts of dephasing and depletion lengths were outlined. In the next chapter, the focus will be on the injection of electrons into the wakefield.

Chapter 4

Electron injection

A typical electron in the plasma fluid interacting with the laser pulse initially slips backward relative to the wake and is not trapped. To undergo acceleration, electrons must be primarily injected into the accelerating phase of the wakefield. This means that they need to first reach specific positions and momenta in the phase space. Once these conditions are met and the electron properly positioned within the plasma wave attains a longitudinal velocity surpassing that of the plasma wave's phase velocity, it becomes carried along by the plasma wave and the acceleration process can start. The trapping of electrons can be achieved by several techniques, which we will refer to as injection methods. In this chapter, we will analyze the process of trapping in the 1D geometry, discuss the basic characteristics of electron beams, and then overview several injection techniques.

4.1 Electron trapping condition

The injection method provides sufficient initial conditions for background plasma electrons to become trapped. The electrons that are trapped then move along closed orbits in the phase space. A curve that separates the region of trapped and untrapped orbits in the phase space is called a separatrix. Thus, the trapping can be also understood as a crossing of the separatrix by the electron trajectory in the phase space.

The separatrix is well described assuming stationary wakefield in the 1D nonlinear cold plasma theory [78]. The motion of the electron fluid in a 1D wakefield with potential ϕ (Eqs. (3.10), or (3.11)) is expressed by Hamiltonian

$$\mathcal{H}(\tilde{\xi}, \tilde{p}_x) = \mathcal{H}_0 = \sqrt{1 + a^2 + \tilde{p}_x^2} - \phi - \beta_{Lg}\tilde{p}_x. \quad (4.1)$$

Here, electron momentum p_x is normalized as $\tilde{p}_x = p_x/(m_e c)$, and $\xi = x - v_{Lg}t$ is normalized as $\tilde{\xi} = k_p \xi$. The energy of the system represented by Hamiltonian \mathcal{H} is conserved because the Hamiltonian is not dependent on time and, therefore, can be expressed by constant \mathcal{H}_0 . Here, a , ϕ , and \tilde{p}_x are $\tilde{\xi}$ -dependent. The square root term in Eq. (4.1) corresponds to the kinetic energy, and the rest of the expression is equal to the potential energy. This equation is a quadratic equation with respect to \tilde{p}_x , with solution

$$\tilde{p}_x(\tilde{\xi}) = \beta_{Lg}\gamma_{Lg}^2(\mathcal{H}_0 + \phi) \pm \gamma_{Lg}\sqrt{\gamma_{Lg}^2(\mathcal{H}_0 + \phi)^2 - (1 + a^2)}. \quad (4.2)$$

Depending on the value of the initial \mathcal{H}_0 , the electron can become trapped, or, in other words, injected into the plasma waves. Examples of several initial values of \mathcal{H}_0 are

presented in Fig. 4.1. The solid blue line corresponds to phase-space trajectories of fluid electrons without the presence of the laser \tilde{p}_x^f , corresponding to Eq. (4.2) with $\mathcal{H}_0 = 1$. The dashed blue lines correspond to particles that experienced nonzero ϕ but were not trapped by the plasma wave. The red dotted lines are the trajectories of electrons that were injected into the plasma wave. Hamiltonian corresponding to particles moving in phase space along separatrix

$$\mathcal{H}_{\text{sep}} = \frac{\sqrt{1 + a^2(\tilde{\xi}_{\text{min}})}}{\gamma_{Lg}} - \phi_{\text{min}}, \quad (4.3)$$

represented by the thick red solid line, separates the regions of trapped particles, and free fluid particles. Here, ϕ_{min} is the minimum potential and $\tilde{\xi}_{\text{min}}$ is a corresponding

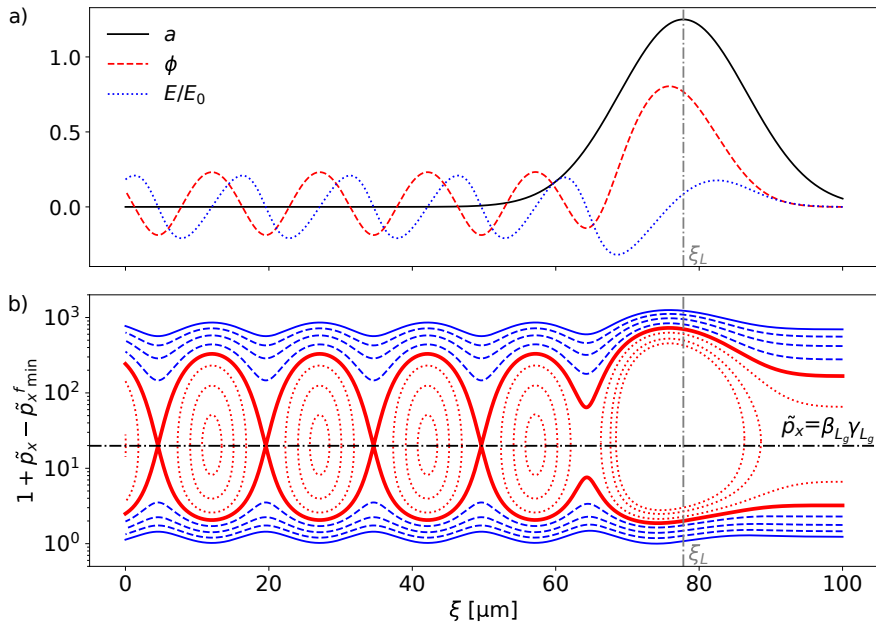


Figure 4.1: Laser potential, wakefield potential and electric field, and corresponding trajectories of electrons in the phase space. The laser and plasma have the following parameters: $a_0 = 1.25$, $\tau_L = 24.7$ fs, $\lambda_L = 0.8$ μm , $n_e = 5 \times 10^{18}$ cm^{-3} . Here, ξ is expressed in microns. The laser pulse is assumed to be one-dimensional with a Gaussian temporal profile (1.1) and nonevolving during its propagation. The laser pulse center is located at $\xi_L = 77.8$ μm (shown by the vertical dash-dotted gray line in both figures). a) Laser potential a (black solid), corresponding wakefield potential ϕ (3.10) solved numerically (red dashed), and electric field $E = -\partial\phi/\partial\xi$ normalized by E_0 (3.9) (blue dotted). b) Trajectories of electrons in the phase space with various \mathcal{H}_0 (4.1). On the y -axis, shown in the logarithmic scale, normalized momentum \tilde{p}_x is summed with 1, and subtracted by $\tilde{p}_{x,\text{min}}^f$, which is the minimum of fluid electron momentum \tilde{p}_x^f . The solid blue line corresponds to phase-space trajectories of fluid electrons \tilde{p}_x^f with $\mathcal{H}_0 = 1$. The dashed blue lines correspond to particles that are not injected, with $\mathcal{H}_0 = 0.4, 0.6, \text{ and } 0.8$. The red thick line represents the separatrix with $\mathcal{H}_{\text{sep}} \approx 0.24$ (4.3). The dotted red lines are the trajectories of injected electrons with $\mathcal{H}_0 = -0.15, -0.05, \text{ and } 0.1$. The horizontal black dash-dotted line represents momentum $\tilde{p}_x = \beta_{Lg} \gamma_{Lg}$ corresponding to the wake velocity.

coordinate. For $|\mathcal{H}_0| > |\mathcal{H}_{\text{sep}}|$, the electrons are not injected. They have an initial momentum too low or high for a given $\tilde{\xi}$ and, thus, they subsequently travel on an open orbit. $|\mathcal{H}_0| \leq |\mathcal{H}_{\text{sep}}|$ is a necessary and sufficient condition for the electron trapping.

The 1D model of trapping demonstrates the crucial requirement for electrons to be at the correct position with the correct momentum in order to become injected. Simplified analytical extensions for the injection process in 3D geometry have also been developed [90, 91]. Usually, the aim of the injection process is to inject electrons into the first wake period with the highest field (i.e., the bubble in the bubble regime), however, this depends on the actual applications. For instance, by injecting electrons into a few first wake periods, "buckets", a train of electron beams can be accelerated [92, 93].

So far, we discussed simplified 1D conditions of the injection for a single electron. When the injection process starts in real conditions, a number of electrons is naturally injected together. Due to the transverse focusing forces, the electrons create an on-axis electron beam. The type of the injection process, i.e., the technique of getting electrons into the right phase-space position, strongly affects the final properties of the whole electron beam. In the rest of the chapter, we first introduce a list of quantities that define an electron beam. Subsequently, the process of self-injection, where electrons are injected due to the natural evolution of the laser pulse and wakefield in plasma, is explained. Finally, an overview of various injection techniques that allow precise control of injection through the manipulation of laser light or plasma is provided.

4.2 Properties of electron beams

The electron beam can be simply defined as a stream of electrons. In the case of LWFA, it is a stream of injected and accelerated electrons. The most used parameters to describe an electron beam are charge, duration, mean energy, energy spread, divergence, and emittance.

The charge of the electron beam (in the absolute value) describes the total absolute charge $Q_e = eN_e$, where N_e is the number of electrons. The duration of the electron beam can be calculated as $\tau_e = L_e/c$, where L_e is the length of the beam, often characterized by its root mean square (RMS) length. In the case of a quasi monoenergetic spectrum, it is practical to define the mean energy of the e^- beam $\mathcal{E}_{\text{mean}}$. The most common definitions of the energy spread $\Delta\mathcal{E}$ are at RMS, or at FWHM. Relative energy spread $\Delta\mathcal{E}/\mathcal{E}_{\text{mean}}$ presents the spread magnitude relative to the mean energy value.

Divergence refers to the spatial dispersion of particles within a beam, or, in other words, the dispersion of angles within a beam. To obtain the transverse RMS divergence, one can calculate

$$\Delta\theta = \sqrt{\frac{\sum_i \theta_i^2}{N_e}}. \quad (4.4)$$

In a 2D definition, calculating the spread of angles, for example, in the y direction, angle θ_i of the i -th electron can be obtained as $\theta_i = \arctan(p_{y_i}/p_{x_i})$, where p_{y_i} is the momentum of the i -th electron in the y direction, and p_{x_i} is its momentum in the longitudinal x direction. The divergence is typically shown in the units of mrad.

Emittance describes the spread of an electron beam in the phase space. While the emittance can be defined in both longitudinal and transverse dimensions, we will

further use the word "emittance" for referring to the transverse normalized emittance, which is a common practice. The distribution of accelerated electrons in the transverse phase spaces (y - p_y , z - p_z), where p_y and p_z represent the electron momenta in the y and z directions, respectively, typically assumes the shape of an ellipse. The emittance is proportional to the area enclosed by this ellipse. Without the loss of generality, normalized emittance of an e^- beam in the y direction can be written as [94]

$$\varepsilon_y = \frac{1}{m_e c} \sqrt{\langle y^2 \rangle \langle p_y^2 \rangle - \langle y p_y \rangle^2}, \quad (4.5)$$

where

$$\langle y^2 \rangle = \frac{\sum_{i=1}^{N_e} y_i^2}{N_e} - \left(\frac{\sum_{i=1}^{N_e} y_i}{N_e} \right)^2, \quad (4.6)$$

$$\langle p_y^2 \rangle = \frac{\sum_{i=1}^{N_e} p_{y_i}^2}{N_e} - \left(\frac{\sum_{i=1}^{N_e} p_{y_i}}{N_e} \right)^2, \quad (4.7)$$

$$\langle y p_y \rangle = \frac{\sum_{i=1}^{N_e} y_i p_{y_i}}{N_e} - \frac{\sum_{i=1}^{N_e} y_i}{N_e} \frac{\sum_{i=1}^{N_e} p_{y_i}}{N_e}, \quad (4.8)$$

and y_i is the y coordinate of the i -th electron. Emittance is commonly expressed in the units of μm or mm mrad . Sometimes, π mm mrad is also used. In this work, we will use the symbol ε_n for normalized transverse emittance expressed in μm .

4.3 Self-injection

The self-injection of background plasma electrons into the wakefield is the least experimentally demanding LWFA injection technique [79]. In the early stages of LWFA experiments, it was already demonstrated that the self-injected electron spectrum in the bubble regime can inherently exhibit quasi monoenergetic characteristics [95–97]. There are two types of this mechanism: the longitudinal and transverse self-injections [28].

Longitudinal self-injection is an analogy to the one-dimensional wave breaking [68, 77, 78]. Electrons which can be later injected originate on the axis of laser propagation, gaining energy by moving across the wakefield. When their velocity exceeds the wake phase velocity v_{Lg} at the time they reach the rear part of the bubble, the wave breaking occurs and the periodical wake structure is destroyed. The electrons can become trapped and further accelerated. This mechanism generally produces a beam with a low divergence but also a low charge (\sim few pC). In low densities, it is possible to achieve only the longitudinal injection, avoiding the presence of transverse injection of different properties [28].

The transverse self-injection [98] is a multi-dimensional effect that occurs in the nonlinear regime. Injected electrons are originally located within a thin cylindrical shell volume (collection volume) with a radius that scales with the laser spot size [79, 99, 100]. They attain a sufficient velocity when sliding down the slowly expanding sheath and become trapped at the rear part of the bubble. If the bubble expansion is time-limited, the injection process is terminated and the resulting electron beam is quasi monoenergetic.

Transverse self-injection can be naturally achieved in later times of the acceleration, after the self-focusing process of the laser pulse. The transverse injection is very suitable

for achieving a high charge in the order of hundreds of pC. On the other hand, it is difficult to control and tune other parameters such as energy spread; therefore, in general, poor-quality electron beams are produced [28]. However, research has shown that with a specific choice of laser-plasma parameters, the properties of electron beams can be at least partially controlled. This can be achieved by properly locating the focus of the laser pulse within the plasma. In such a case, the continuous injection can be suppressed, reducing the low-energy tail of the electron beam [101].

■ 4.4 Other injection mechanisms

In addition to the self-injection, several other techniques have been developed for improved control of the injection process. The aim is to reach enhanced tunability and to provide a separation of the injection and acceleration process. Here, we list several injection techniques.

■ 4.4.1 Optical injection

The concept of optical injection relies on the utilization of one or more laser pulses (referred to as injection pulses, or injectors) to induce the injection of electrons into the wakefield generated by the primary laser pulse (referred to as the drive pulse, or driver).

The LILAC (Laser Injected Laser ACcelerator) scheme was the first proposal of optical injection. It was introduced by Umstadter et al. in 1996 [102]. In this scheme, a transversely propagating injection pulse intersects with the wakefield generated by the drive pulse. The polarization vector of the injector is parallel to the longitudinal field of the driver wakefield. The ponderomotive force exerted by the injection pulse disrupts the trajectories of plasma electrons. Some of these electrons gain sufficient momentum to become injected into the driver wakefield.

Shortly after the LILAC, an alternative optical injection method driven by the interference of two counter-propagating injection laser pulses has been proposed [103–106]. In this scheme, the two pulses, with polarizations perpendicular to the polarization of the drive beam, collide behind the drive beam, creating a slow beat wave. Electrons within this beat wave undergo longitudinal oscillations, acquiring additional longitudinal momentum that is sufficient for wakefield trapping. Subsequently, a simplified version of this method was introduced, utilizing just one injection beam with the same polarization direction as the one of the drive beam [107] (see Fig. 4.2 for the illustration). This injection method has been then demonstrated experimentally, producing quasi monoenergetic electron beams with tunable beam energy [108]. Recently, the LILAC ponderomotive technique has been also carried out experimentally, however, not at 90° but at 155° collision angle [109]. In addition, the optical injection can be also a result of wake-wake interaction instead of pulse-pulse interaction [110], which has been also shown experimentally [109]. In experiments with counter-propagating pulses, the collision angle often deviates from 180° [93, 109, 111–113], in order to avoid damage of the optical system [112].

Other optical methods have been also proposed by simulations. For instance, it has been shown that a low-intensity counter-propagating injection beam can trigger the injection in the same manner as transverse self-injection, by slightly suppressing the

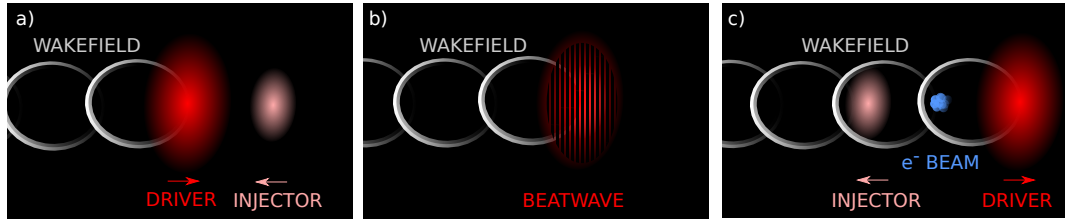


Figure 4.2: *Principle of the beatwave optical injection.* a) The driver coming from the left creates the wakefield. The less intense injector is coming from the right. b) The two pulses collide creating the beatwave. c) The collision results in the injection of the e^- beam into the driver wakefield.

ponderomotive force of the drive beam [114]. Another example is an orthogonal collision of two laser pulses with perpendicular polarizations that induces electron trapping, mostly due to the stochastic heating of electrons [115]. Further simulation studies have revealed that the injection can be triggered by an injection pulse that propagates some distance behind the drive pulse if the delay between the beams is properly adjusted [87, 116].

■ 4.4.2 Density down-ramp injection

The down-ramp injection was first described by Bulanov et al. in 1998 [117]. The injection is based on the propagation of a laser pulse through a downward transition (down ramp) in plasma density. When a laser pulse, centered at $\xi = 0$, originally propagating through a uniform plasma, enters a down ramp, the local phase velocity changes as

$$v_{Lg} = \frac{c}{1 + \frac{\xi}{k_p} \frac{dk_p}{dx}}. \quad (4.9)$$

Since $\xi < 0$ for the wake, because it is always behind the pulse, the phase velocity decreases because $dn_e/dx < 0$, which also means that $dk_p/dx < 0$. In other words, the phase velocity of the wakefield decreases as long as the plasma density decreases. If the fluid velocity of electrons locally equals or exceeds v_{Lg} , injection is triggered, and electrons are consequently trapped in the wakefield [42].

It has been experimentally proven that the stability of beams injected by this method can be better than the one of beams generated by the self-injection mechanism [118]. Simulations have shown that the quality of the electron beam depends on the ramp length, the peak density of the ramp, as well as the laser intensity [119].

The injection has been demonstrated experimentally by many scientific groups, e.g., Refs. [118, 120–125]. The density down-ramp effect can be obtained by laser focusing at the downstream edge of a gas jet [120], using another laser pulse to create a density perturbation [122], inserting a narrow nozzle into a gas jet supplied from a thicker nozzle [118], or inducing a shock in the gas flow [121, 123–125].

■ 4.4.3 Ionization injection

Electrons can be also trapped in the wakefield due to additional ionization by the driver laser beam [52, 126, 127]. The core of this method is in the utilization of a mixture

of low and high- Z gases, where Z is the atomic number, such as the mixture of helium and nitrogen. Outer-shell electrons of the high- Z gas are ionized by the less intense front of the laser pulse. In contrast, inner shell electrons can overcome atom binding energy only at later times, in the regions of the highest laser intensity. As a consequence, they are released close to the axis and slip back to the rear part of the accelerating area, i.e., the rear part of the bubble in the bubble regime. This dephasing of electrons causes crossing of the separatrix, hence, the electrons become trapped in the wakefield.

Ionization injection might naturally result in a large energy spread of the electron beam, as the injection is triggered continuously along a long-distance region [52, 127]. This aspect can be significantly improved by operating in the regime of self-truncated ionization injection, where the laser intensity is properly chosen for the particular gas mixture. The ionization of the high- Z gas then occurs only in the region of the highest self-focusing, resulting in a short duration of the process [128]. Also, simulations have shown that the application of a few-tens-of-Tesla magnetic field can ensure that the injection occurs over a shorter distance with reduced energy spread and enhanced charge and peak energy [129].

■ 4.4.4 Injection by nanoparticles

The first concept of utilizing nano-scale particles for the injection was published in 2007, suggesting that the disturbance of the wakefield by a nanowire in the plasma can trigger electron trapping [130]. Later, in 2018, a complex theoretical and simulation study about nanoparticle-assisted injection was published [131]. The idea is to utilize nanoparticles inserted into plasmas. As a laser pulse propagates through the plasma, the nanoparticle is ionized by the leading edge of the laser pulse. The electric field of the ionized nanoparticles increases and attracts vicinal electrons. As a consequence, the attracted electrons gain additional momentum and overcome the threshold for trapping. The results also suggest that the beam charge can be controlled by tuning the material density, number, and position of nanoparticles. Recently, the method has been verified experimentally [7, 132]. A stable generation of electron beams with a charge of hundreds of pC, broad energy spectrum, and small divergence has been demonstrated [7].

■ 4.4.5 External injection

The control of the injection process offers the tunability of electron beams and separation of the injection and acceleration process. Nonetheless, it still relies on the interaction of the laser pulse and background plasma electrons which eventually form a compact electron beam. In contrast to the previous methods, in external injection, the electron beam does not come from the background plasma but it is delivered from an external conventional accelerator. This accelerator also provides electron pre-acceleration, necessary for wakefield trapping. The external source provides more stable control of the initial quality of the electron beam, while LWFA provides a much shorter and more compact acceleration device for further acceleration. The external injection therefore combines the advantages of radiofrequency and laser-based acceleration.

One of the biggest challenges of the technique is to synchronize the external electron beam with the wakefield. The arrival time jitter of the electron beam Δt_{arr} has to be significantly smaller than the wake period $\Delta t_{arr} \ll \lambda_p/c$ [133]. Moreover, the duration

of the electron beam has to be in the range of a few fs. The e^- beam transverse size in the micrometer scale is required to achieve proper transverse dimensions for trapping [133]. In addition, the transition between vacuum and plasma can remarkably influence the e^- beam parameters [134, 135]. Nowadays, several projects worldwide have attempted to demonstrate a high-efficiency capture, e.g., Refs. [136–139]. The study of external injection might also bring insight into the staging of plasma-based acceleration.

■ 4.4.6 Combined injection methods

In addition to all the methods mentioned here, it has been shown that certain combinations of these techniques can be also utilized. For instance, a combination of a down-ramp injection and ionization injection in a gas mixture of helium and nitrogen at the plasma entrance resulted in enhanced stability of the electron beam energy and charge [140]. Another interesting optical technique examined by numerical simulations relies on an injection pulse that has frequency tripled compared to the co-propagating drive pulse [141]. The ionization injection occurs when the peak amplitude of the combined fields exceeds a certain threshold. It is also possible to utilize an injection laser pulse propagating orthogonally to the drive pulse in a high- Z gas [142]. The drive laser pulse excites the wakefield, while the injection pulse further ionizes the medium to high-charge states to induce the ionization injection into the drive wakefield.

To summarize this chapter, numerous injection methods have been proposed and widely examined by the scientific community, each offering distinct benefits with various experimental demands. The variety of techniques might ultimately offer a higher diversity of future applications.

Chapter 5

Other laser-driven and plasma-based electron acceleration methods

In addition to LWFA, other laser-driven and plasma-based electron acceleration methods have been invented. Here, we provide an overview of several of these techniques.

5.1 Plasma beat wave acceleration

Plasma beat wave acceleration (PBWA) was suggested by Tajima and Dawson in the original paper about LWFA [2] as its potential alternative. The basis for PBWA is the resonant excitation of a plasma wave using two laser pulses, an idea that had been previously explored by Rosenbluth and Liu in 1972 for plasma heating applications [143].

In PBWA, the process involves the utilization of two relatively long laser pulses ($c\tau_L > \lambda_p$) with frequencies ω_{L1} and ω_{L2} ($\omega_{L1} > \omega_{L2}$) that resonantly excite a plasma wave. The frequencies must be chosen properly to satisfy resonant condition $\Delta\omega_L = \omega_{L1} - \omega_{L2} \approx \omega_p$. The beat wave generated by the pulses acts as a series of short laser pulses of duration $\Delta\tau_L = 2\pi/\Delta\omega_L$. The ponderomotive force that comes from the beating laser pulses drives the plasma wave with a large amplitude. The phase velocity of the plasma wave is given by $\Delta\omega_L/\Delta k_L$, where $\Delta k_L = k_{L1} - k_{L2}$ and k_{L1} and k_{L2} are the wavenumbers of the lasers with frequencies ω_{L1} and ω_{L2} , respectively [42].

This technique does not require such high intensities as LWFA. This was a very interesting advantage, especially at the time of its invention in 1979, when ultraintense laser pulses ($\gtrsim 10^{18}$ W/cm²) were not available. However, PBWA has several limitations. For instance, due to the nonlinear effects, the period of the beat wave is fixed, whereas the period of the plasma wave increases. Consequently, the plasma wave eventually becomes out of phase with the laser beat wave. This resonant detuning puts a limit on the maximum amplitude of the plasma wave [42, 143]. In addition, plasma instabilities, such as the saturation of the wave by a parametric coupling to ion waves, can be a limiting factor in PBWA [144]. While LWFA has been recently studied more extensively, some works have also explored the PBWA regime lately, e.g., Ref. [145].

5.2 Acceleration by a train of short laser pulses

The generation of a plasma wave can be also achieved through a sequence of short laser pulses [74, 146]. This pulse train can be fine-tuned if the width of the pulses and spacing between them are independently controlled, maintaining a resonance with the plasma wave [147]. Careful optimization of these laser pulse parameters helps to eliminate resonant detuning. While the control of the plasma wave can be more difficult than in the LWFA case, a train of pulses has the advantage of driving amplitude waves larger than a single pulse with the same energy due to the enhancement of the ponderomotive force [147, 148]. Nowadays, the pulse train can be, for instance, obtained via temporal shaping techniques from a single laser pulse. A minor fraction of the same pulse can undergo frequency doubling or tripling to serve as an ionizing pulse, enabling ionization injection into the plasma wave [149].

5.3 Self-modulated laser wakefield acceleration

Under specific conditions, a single laser pulse can undergo self-modulation, breaking into a sequence of short pulses with widths in the order of the plasma wavelength λ_p . This process, referred to as self-modulated laser wakefield acceleration (SM-LWFA) [43, 45, 150–152] requires that the pulse length is long compared to the plasma wavelength $c\tau_L > \lambda_p$ and the pulse power is larger than the power required for relativistic self-guiding of the laser pulse $P > P_c$ [43, 45, 152, 153]. The self-modulation is an instability that occurs from the plasma wave generating regions of boosted focusing and diffraction [154]. The precise control of the phase and amplitude of the plasma wave in the SM-LWFA regime is difficult as the mechanism is based on an instability [155].

5.4 Direct laser acceleration

When an electron beam directly interacts with a laser pulse, a mechanism called direct laser acceleration (DLA) [156, 157] can be initiated, leading to the acceleration of electrons. DLA is based on effective resonance energy exchange between the pulse and electrons [157]. It occurs when the betatron oscillation frequency (3.22) of electrons in the plasma is close to the Doppler-shifted laser frequency experienced by relativistic electrons. In this scenario, electrons experience a substantial increase in longitudinal momentum through the $\mathbf{v} \times \mathbf{B}$ component of the Lorentz force (2.9) [156].

Simultaneous acceleration can be achieved through the combined processes of SM-LWFA and DLA [158], or, alternatively, by synchronous LWFA and DLA when a part of the laser pulse with sufficient intensity overlaps with an electron beam inside the bubble [159, 160]. DLA generates a broad energy spectrum but it can be very useful for applications where a high charge is required since it is capable of producing ~ 100 s of nC [161].

DLA might benefit from an energy gain at high intensities as the maximum energy of electrons increases with increasing intensity [162]. In the regime of extreme intensities $\gtrsim 10^{22}$ W/cm², which are currently already available, radiation reaction can be expected to noticeably affect electron motion [163–166]. Radiation reaction is a phenomenon where electrons in an intense electromagnetic field lose energy as they produce radiation (as

discussed in Sec. 6.4 in more detail), which in turn alters their trajectories. Nevertheless, a recent study has demonstrated that for the DLA with multi-PW laser pulses, it might be more beneficial to operate at intensities $I \sim 10^{21}$ W/cm² and instead increase the value of w_0 [167].

■ 5.5 Plasma wakefield acceleration

Plasma wakefield acceleration (PWFA) is a method for accelerating particles to relativistic energies based on a similar principle as LWFA. However, instead of a laser beam, a beam of particles (electrons [168, 169], protons [170, 171], or positrons [172]) is used as the driver. The advantage of these accelerators is that the dephasing length is not relevant as the driver propagates with velocity close to the speed of light; thus, acceleration can be maintained for a long time.

Due to this advantage, these types of accelerators are widely studied nowadays, hand-in-hand with laser wakefield accelerators. Moreover, the hybrid LWFA-PWFA technique might bring the advantages of both methods in the future. In this case, LWFA generates an electron beam which then drives a subsequent PWFA stage.

The energy spread of electrons generated by PWFA is quite large; however, some approaches for spread reduction have been proposed [173, 174]. An energy spread of about 0.1% has been recently reported from the SPARC_LAB facility in Frascati, Italy [175].

Chapter 6

X-ray sources from LWFA electrons

In this chapter, we describe the X-ray generation produced by charged particles, types of secondary X-ray sources from LWFA electrons, and the effect of radiation reaction on relativistic particles.

6.1 Radiation generated by a single charged particle

First, we describe the radiation from a moving charged particle that undergoes a change in its velocity in a general sense. To put it simply, when the velocity of the particle is altered, it creates a disturbance in the electric and magnetic fields around it. This disruption is transformed into a traveling electromagnetic wave, which carries energy away from the particle.

The analysis of the radiation of electromagnetic waves from a particle can be found, e.g., in Ref. [176]. The radiation from a single electron calculated at the observer point \mathbf{r} far from the source, located at \mathbf{r}_e , can be calculated by the Liénard-Wiechert retarded potentials

$$\phi_{\text{LW}}(\mathbf{r}, t) = -\frac{e}{4\pi\epsilon_0} \left[\frac{1}{(1 - \boldsymbol{\beta} \cdot \mathbf{n})R} \right]_{\text{ret}}, \quad (6.1)$$

and

$$\mathbf{A}_{\text{LW}}(\mathbf{r}, t) = -\frac{e}{4\pi\epsilon_0 c} \left[\frac{\boldsymbol{\beta}}{(1 - \boldsymbol{\beta} \cdot \mathbf{n})R} \right]_{\text{ret}}. \quad (6.2)$$

Here, $\boldsymbol{\beta} = \mathbf{v}/c$, where \mathbf{v} is the velocity of the electron, \mathbf{n} is a unit vector in the direction $\mathbf{R} = \mathbf{r} - \mathbf{r}_e$, and $R = |\mathbf{R}|$ is the distance between the emission point and the observer point. The symbol "ret" refers to the fact that the quantities are expressed in retarded time

$$t' = t - \frac{|\mathbf{R}|}{c}, \quad (6.3)$$

where t is the time at the observer frame. Using $\mathbf{E}_{\text{LW}} = -\nabla\phi_{\text{LW}} - \partial\mathbf{A}_{\text{LW}}/\partial t$ and $\mathbf{B}_{\text{LW}} = \nabla \times \mathbf{A}_{\text{LW}}$, one can obtain formulas for the electric and magnetic fields emitted by the particle:

$$\mathbf{E}_{\text{LW}}(\mathbf{r}, t) = -\frac{e}{4\pi\epsilon_0} \left[\frac{(1 - \beta^2)(\mathbf{n} - \boldsymbol{\beta})}{(1 - \boldsymbol{\beta} \cdot \mathbf{n})^3 R^2} + \frac{\mathbf{n} \times ((\mathbf{n} - \boldsymbol{\beta}) \times \dot{\boldsymbol{\beta}})}{(1 - \boldsymbol{\beta} \cdot \mathbf{n})^3 cR} \right]_{\text{ret}}, \quad (6.4)$$

and

$$\mathbf{B}_{\text{LW}}(\mathbf{r}, t) = -\frac{e}{4\pi\epsilon_0 c} \left[\frac{(1 - \beta^2) (\mathbf{n} \times (\mathbf{n} - \beta))}{(1 - \beta \cdot \mathbf{n})^3 R^2} + \frac{\mathbf{n} \times \dot{\beta} + \mathbf{n} \times (\mathbf{n} \times (\beta \times \dot{\beta}))}{(1 - \beta \cdot \mathbf{n})^3 cR} \right]_{ret}, \quad (6.5)$$

respectively. Here, $\dot{\beta} = d\beta/dt$. For relativistic motion, the radiation is spread over a wide range of frequencies [176]. The radiation intensity radiated per unit solid angle Ω per unit frequency ω can be expressed in the general form as follows:

$$\frac{d^2 I}{d\omega d\Omega} = \frac{c\epsilon_0}{\pi} |\mathcal{F}[R(t)\mathbf{E}(t)](\omega)|^2, \quad (6.6)$$

where \mathcal{F} indicates the Fourier transform from time t to frequencies ω . Using the electric field from Eq. (6.4), one can write Eq. (6.6) accordingly as

$$\frac{d^2 I}{d\omega d\Omega} = \frac{e^2}{16\pi^3 \epsilon_0 c} \left| \int_{-\infty}^{\infty} \frac{\mathbf{n} \times ((\mathbf{n} - \beta) \times \dot{\beta})}{(1 - \beta \cdot \mathbf{n})^2} e^{i\omega(t - \mathbf{n} \cdot \mathbf{r}_e(t)/c)} dt \right|^2. \quad (6.7)$$

Here, because the observation is conducted far from the source, it is assumed that this distance is sufficient for the vector \mathbf{n} to vary only slightly during the motion and can be therefore considered as a constant. Also, $R(t') \approx r - \mathbf{n} \cdot \mathbf{r}_e(t')$, where $r = |\mathbf{r}|$ is a distance from the origin to the observation point.

6.2 Betatron radiation

Transverse oscillations of electrons in plasma can lead to the production of betatron radiation [177–180]. This is also an intrinsic feature of electrons accelerated by LWFA, where betatron oscillations result from the transverse force that, in addition to the accelerating wakefield forces, pushes electrons towards the laser propagation axis. The radiation is produced whenever the electron is injected slightly off the propagation axis. For typical electron beams with a finite transverse size, this implies that electrons within the beam undergo such oscillations. Radiation is emitted mostly at the turning points of electron sine-like trajectories. The process is illustrated in Fig. 6.1.

The wavelength of the betatron oscillations of the electron in the bubble regime can be approximated as follows. We neglect transverse velocities of the electron $v_y \approx 0$ and $v_z \approx 0$ and assume that $v_x \approx c$. Then the Lorentz force (2.9) experienced by electrons in the y and z directions can be, respectively, written as

$$F_y = \frac{d(m_e \gamma v_y)}{dt} = -e(E_y - cB_z),$$

$$F_z = \frac{d(m_e \gamma v_z)}{dt} = -e(E_z + cB_y).$$

We will now consider the bubble fields according to the phenomenological model (3.19), getting

$$\frac{d^2 y}{dt^2} + \left(\frac{1}{\gamma} \frac{d\gamma}{dt} \right) \frac{dy}{dt} = -\frac{\omega_p^2}{2\gamma} y,$$

$$\frac{d^2 z}{dt^2} + \left(\frac{1}{\gamma} \frac{d\gamma}{dt} \right) \frac{dz}{dt} = -\frac{\omega_p^2}{2\gamma} z.$$

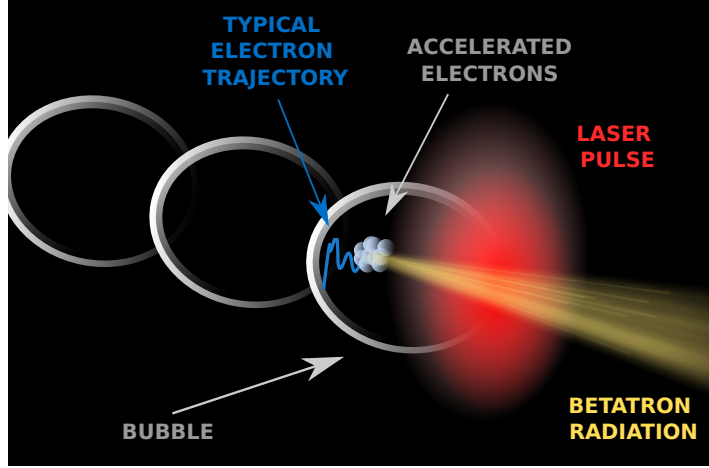


Figure 6.1: *Principle of betatron radiation.* Accelerated electrons in the electron beam oscillate in the bubble, located behind the laser pulse, as they are accelerated forward in the direction of the pulse propagation. Betatron radiation, typically generated in the X-ray range, is produced most at the turning points of electron trajectories within a cone oriented forward. A typical trajectory of a single electron is depicted by the blue curve. In practice, each electron within the beam follows a unique trajectory.

These are the equations of a harmonic oscillator with betatron frequency (3.22). The wavelength of betatron oscillations can be written as $\lambda_\beta = \lambda_p \sqrt{2\gamma}$. Due to the gradual growth of γ during the acceleration, λ_β also increases. When the electron changes the direction, momentum varies rapidly but the change in energy is small. The amplitude of oscillations r_β decreases with $\gamma^{-1/4}$ [176], and the oscillations are damped with time.

In order to characterize betatron radiation, parameter $K = r_\beta k_p \sqrt{\gamma/2}$, commonly used to describe radiation emitted from undulators, can be employed. Based on K , two different regimes of radiation can be distinguished: undulator regime ($K \ll 1$), and wiggler regime ($K \gg 1$), which occurs exclusively in the case of LWFA betatron radiation [180–183]. The latter regime produces a broad, synchrotron-like spectrum within a very narrow cone around the axis of the laser pulse propagation, typically in the range from several keV up to 10s of keV energies [31]. An electron oscillating with λ_β emits primarily at the fundamental wavelength $\lambda_\beta/(2\gamma^2)$. The denominator represents a double Lorentz transformation, first from the laboratory frame to the electron frame, and then from the Doppler effect of observing the electron emission in the laboratory frame.

The formula for radiation (6.6) is valid for arbitrary particle motion. To calculate betatron radiation, we can assume that the particle moves in an instantaneous circular motion. Eq. (6.6) can be written in the following form:

$$\frac{d^2I}{d\omega d\Omega} = \frac{e^2 \omega^2}{16\pi^3 c \epsilon_0} \left| \int_{-\infty}^{\infty} \mathbf{n} \times (\mathbf{n} \times \boldsymbol{\beta}) e^{i\omega(t - \mathbf{n} \cdot \mathbf{r}_e(t)/c)} dt \right|^2 \quad (6.8)$$

Assume that a relativistic electron with motion in the $x - y$ plane travels in the positive x direction with normalized velocity $\beta_x \sim 1$. The observation takes place in the $y - z$ plane. θ is an angle between \mathbf{n} and the x -axis. We can then write

$$\mathbf{n} \times (\mathbf{n} \times \boldsymbol{\beta}) = \beta(-\mathbf{e}_\parallel \sin(vt/\rho) + \mathbf{e}_\perp \cos(vt/\rho) \sin \theta), \quad (6.9)$$

$$t - \mathbf{n} \cdot \mathbf{r}_e(t)/c = t - (\rho/c) \sin(vt/\rho) \cos \theta, \quad (6.10)$$

where \mathbf{e}_{\parallel} is the unit vector in the y direction, $\mathbf{e}_{\perp} = \mathbf{n} \times \mathbf{e}_{\parallel}$, and ρ is an instantaneous radius of curvature of the electron path. We assume here that the radiation is concentrated within a very small angle, i.e., $\theta \ll 1$. The equation (6.8) then leads to

$$\frac{d^2 I}{d\omega d\Omega} = \frac{e^2 \omega^2}{16\pi^3 c \varepsilon_0} | -\mathbf{e}_{\parallel} A_{\parallel}(\omega) + \mathbf{e}_{\perp} A_{\perp}(\omega) |^2, \quad (6.11)$$

where

$$A_{\parallel}(\omega) = \frac{c}{\rho} \int_{-\infty}^{\infty} t \exp \left(i \frac{\omega}{2} \left[\left(\frac{1}{\gamma^2} + \theta^2 \right) t + \frac{c^2}{3\rho^2} t^3 \right] \right) dt, \quad (6.12)$$

$$A_{\perp}(\omega) = \theta \int_{-\infty}^{\infty} t \exp \left(i \frac{\omega}{2} \left[\left(\frac{1}{\gamma^2} + \theta^2 \right) t + \frac{c^2}{3\rho^2} t^3 \right] \right) dt. \quad (6.13)$$

Finally, we get

$$\frac{d^2 I}{d\omega d\Omega} = \frac{e^2 \omega^2 \rho^2}{12\pi^3 c^2 \varepsilon_0} \left(\frac{1}{\gamma^2} + \theta^2 \right) \left[K_{2/3}^2(\Xi) + \frac{\theta^2}{1/\gamma^2 + \theta^2} K_{1/3}^2(\Xi) \right], \quad (6.14)$$

where $K_{2/3}$ and $K_{1/3}$ are modified Bessel functions of the second kind, and $\Xi = \frac{\omega \rho}{3c} \left(\frac{1}{\gamma^2} + \theta^2 \right)^{3/2}$. A half of the power is radiated at frequencies below critical frequency [176, 178]

$$\omega_c = \frac{3c\gamma^3}{2\rho} = \frac{3}{2} K \gamma^2 \omega_{\beta} \sim \frac{\sqrt{n_e} r_{\beta} \gamma^{5/2}}{\lambda_{\beta}}. \quad (6.15)$$

It can be seen that the critical frequency increases with increasing plasma density, electron energy and oscillation amplitude, and decreases with the increasing betatron wavelength.

In LWFA, betatron oscillations typically produce fundamental radiation in the soft X-ray regime [31], however, it is possible to extend this range even up to gamma spectrum. For instance, the betatron amplitude can be resonantly enhanced when electrons interact with the rear part of the laser pulse [184, 185]. Experimentally, 10^7 photons with energies between 1 and 7 MeV were emitted by this method [185].

6.3 Other secondary sources of X-rays from LWFA electrons

In this section, we will discuss types of secondary X-ray radiation that are not intrinsic to LWFA but can be generated by utilizing electron beams that were produced from a LWFA source. As a consequence, such X-ray sources inherit the compactness of the LWFA accelerator, compared to the conventional sources of relativistic electrons. In particular, here, we focus on brief descriptions of free electron laser, inverse Compton scattering, and bremsstrahlung.

6.3.1 Free electron laser (FEL)

FEL is a specific type of laser where the amplification of the radiation is reached by precise movements of electrons in the magnetic field [186, 187], instead of the excitation of atoms as in typical laser systems. There is especially a great interest in building FELs that

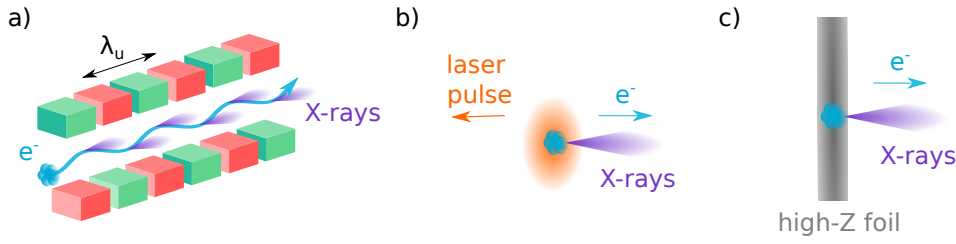


Figure 6.2: *Generation of secondary X-ray radiation.* a) XFEL: The e^- beam (blue) travels through periodic magnetic field (red and green magnets) of the undulator, alternating with wavelength λ_u , emitting coherent X-ray radiation (purple). b) Inverse-Compton scattering: the e^- beam is scattered by the light of the laser pulse (orange), which leads to the production of X-ray photons. c) Bremsstrahlung radiation is produced when the e^- beam is slowing down in the high-Z foil (grey).

can produce radiation in the X-ray range (XFELs). A principle of XFEL is depicted in Fig. 6.2a).

In the FEL, relativistic electrons propagate through an undulator consisting of a series of magnets with alternating polarity. In addition to the longitudinal motion, electrons oscillate transversely during the transition through the undulator. While undergoing the oscillations, electrons emit synchrotron radiation. This radiation is not coherent. However, if the undulator properties are properly tuned (resonance condition is matched), the transverse electric field from transverse electron motion couples with the transverse field of the radiation. As electrons and the field exchange energy, some electrons are accelerated, while some of them are decelerated. As a result, electrons couple into microbunches and emit coherent radiation. Until the saturation of the effect, the radiation is gradually amplified.

The basic principle of FEL can be described via undulator motion. Assume that the electron beam is moving in the x direction. The magnetic field in the undulator is nonzero in the y direction and oscillates in the x direction $B_y = B_0 \cos(2\pi x/\lambda_u)$, with the amplitude B_0 and undulator wavelength λ_u . The resulting lasing wavelength is

$$\lambda_{\text{FEL}} = \frac{\lambda_u}{2\gamma^2} \left(1 + K_u^2/2 + \gamma^2\theta^2 \right), \quad (6.16)$$

where $K_u = eB_0\lambda_u/(2\pi m_e c)$ is the undulator strength.

The emission can be self-amplified or initially induced. In the self-amplified spontaneous emission (SASE), electrons are initially distributed regularly and emit incoherently, until they microbunch and the radiation starts to be emitted coherently. In the seeded FEL, electrons pre-interact with a coherent source seed in a shorter undulator, resulting in coherent amplification. By employing this approach, temporal coherence, which is naturally missing in SASE, is enhanced.

Currently, XFELs operate on the basis of conventional technology, with GeV electron beams produced on km ranges. For instance, European XFEL (EuXFEL) is a 3.4-km long X-ray source [188]. As plasma-based accelerators are also capable of producing e^- beams in such an energy range, LWFA-based XFEL would lead to a compact bright X-ray source. Recently, the first proof-of-principle XUV FEL based on the LWFA method has been demonstrated, lasing at $\lambda_{\text{FEL}} = 27$ nm wavelength [189]. Shortly after that, a

demonstration of an LWFA-based FEL in a seeded configuration was presented, where control over the radiation wavelength was accomplished [190]. An external seed of wavelength 270 nm was produced by separating a small fraction of the driver laser and subsequently tripling its frequency. These results might build a path towards a compact LWFA-driven XFEL.

■ 6.3.2 Inverse Compton scattering

In inverse Compton scattering (ICS), a relativistic electron collides with a photon [191]. As a consequence, a new photon with a higher energy is scattered. In experiments, low energy laser photons of near-infrared wavelength are typically used. One can utilize LWFA-produced relativistic electrons that collide with a laser pulse from the same laser system at 180° , as illustrated in Fig. 6.2b), which is the geometry leading to the highest achievable photon energy. Laser photon frequency ω_L is typically significantly lower than the frequency of the newly generated photon in the laboratory frame $\omega_\gamma = 4\gamma^2\omega_L$, where γ is the electron relativistic factor. This is due to the effect of the Doppler upshift by 2γ in the electron reference frame, and the second Doppler upshift by 2γ in the laboratory frame.

In reality, the collision is typically performed at an obtuse angle close to $\alpha \approx 180^\circ$ to avoid damage to optics. Also, due to the oscillations of the electron in the laser field, its relativistic factor reduces to $\gamma \rightarrow \gamma/\sqrt{1+a_0^2}$, leading to changes in the final photon energies [192]. If radiation reaction is negligible, then the energy of the scattered photon observed close to the axis can be expressed as

$$\mathcal{E}_\gamma = \frac{2\gamma^2(1 - \beta \cos \alpha)}{1 + \gamma^2\theta^2 + a_0^2/2 + 4\gamma\frac{\mathcal{E}_L}{m_e c^2} \sqrt{1 + a_0^2/2}} \mathcal{E}_L, \quad (6.17)$$

where β is the ratio of electron velocity to c , θ is the angle at which the photon is emitted with respect to the electron propagation axis, and \mathcal{E}_L is the energy of the laser photon. If a beam of produced photons is observed at a small angle, the spectrum is quasi-monoenergetic [31]. Its energy spread depends on the observation angle, electron beam energy and energy spread, electron beam emittance, as well as the energy spread of the laser potential across the laser beam [193, 194]. For high laser intensities, where $a_0 \gtrsim 1$, ICS is in the nonlinear regime, where multiple laser photons (instead of one) scatter from an electron to produce one high-energy photon. Compton sources typically range from X-ray to gamma-ray spectrum, with energies from keVs to 10s of MeVs [31].

■ 6.3.3 Bremsstrahlung

The bremsstrahlung process can be triggered by relativistic electrons impinging on a dense target (see Fig. 6.2c). When they pass through the high- Z material, they radiate photons in the gamma range as they slow down in the proximity of nuclei inside the target. The energy of photons produced by bremsstrahlung is in a similar range as in the case of Compton sources [31]. It is even possible to generate bremsstrahlung radiation reaching an energy of more than 100 MeV using electrons accelerated by an intense laser pulse [195]. Compared to betatron radiation and ICS, the repetition rate is not given by the laser system (~ 10 Hz), but it is limited by the solid target [31].

6.4 Radiation reaction

In this section, the effects of radiation reaction (RR) are described. RR expresses a response of a particle to its own radiation. In classical electrodynamics, it can be characterized by the Abraham-Lorentz equation [196]. The RR force acting on a single electron can be written in a simple form as

$$F_{\text{rad}} = \frac{e^2}{6\pi\epsilon_0 c^3} \dot{\mathbf{a}}, \quad (6.18)$$

where $\dot{\mathbf{a}}$ is a time derivative of the electron acceleration vector \mathbf{a} . A generalized self-consistent form of the equation of motion under the influence of the external forces and the radiation recoil force is called the Lorentz–Abraham–Dirac (LAD) equation [197]:

$$\frac{du^\mu}{d\tau} = -\frac{e}{m_e} F_{\text{ext}}^{\mu\nu} u_\nu + \frac{e^2}{6\pi m_e} \left(\frac{d^2 u^\mu}{d\tau^2} + u^\mu \frac{du_\nu}{d\tau} \frac{du^\nu}{d\tau} \right). \quad (6.19)$$

Here, u is the electron four-velocity, τ is the proper time, and $F_{\text{ext},\mu\nu}$ is the field tensor of the external electromagnetic field. When there is no external force acting on the electron in addition to RR, the LAD equation leads to a solution with an exponential acceleration. Moreover, some solutions lead to violation of the causality. In addition, the LAD equation includes the third derivative of the position, leading to the necessity of three integration constants.

Later, a simplified solution of the LAD equation was proposed. It uses an assumption that the second term in Eq. (6.19), corresponding to the RR force, is significantly smaller than the first term $-(e/m_e)F_{\text{ext}}^{\mu\nu}u_\nu$, connected to the external force. In this case, a substitution $du/d\tau \rightarrow -(e/m_e)F_{\text{ext}}^{\mu\nu}u_\nu$ can be applied. The resulting formula called the Landau–Lifshitz equation can be written as [198]

$$\frac{du^\mu}{d\tau} = -\frac{e}{m_e} F_{\text{ext}}^{\mu\nu} u_\nu + \frac{e^4}{6\pi m_e} \left[-\frac{m_e}{e} (\partial_\alpha F_{\text{ext}}^{\mu\nu}) u_\nu u^\alpha + F_{\text{ext}}^{\mu\nu} F_{\text{ext},\nu\alpha} u^\alpha + (F_{\text{ext}}^{\nu\alpha} u_\alpha)^2 u^\mu \right]. \quad (6.20)$$

This equation is free from the third derivative of the position. Currently, it is the most widely used classical theory of RR [199]. An exact solution for an electron motion in a plane wave has been also derived [200].

In the classical Landau–Lifshitz approximation, the electron is losing energy continuously. When the energy of radiated photons is not negligible compared to the electron mass, the quantum effects need to be taken into account. In this case, the photon emission has stochastic features and individual particles can experience sudden energy drops. The relevance of quantum effects on electron dynamics is typically described by dimensionless electron quantum parameter

$$\chi_e = \frac{|p_\mu F^{\mu\nu}|}{m_e c E_c}, \quad (6.21)$$

where p is the electron four-momentum and $F_{\mu\nu}$ is the general electromagnetic tensor. E_c represents so-called Schwinger field

$$E_c = \frac{m_e^2 c^3}{e\hbar} \approx 10^{18} \text{ V/m}, \quad (6.22)$$

which corresponds to the value when the electromagnetic field becomes nonlinear. Here, \hbar is the reduced Planck constant. For instance, for a laser wavelength $\lambda_L = 1 \mu\text{m}$, E_c corresponds to intensities in the range of 10^{29} W/cm^2 . When $\chi_e \gtrsim 1$, the particle experiences the electric field $E \gtrsim E_c$ in its rest frame and the quantum effects are substantial. Consequently, the classical approximation can be used when $\chi_e \ll 1$. For $\chi_e \gtrsim 0.1$, quantum electrodynamics (QED) stochastic effects start to play a nonnegligible role. For $\chi_e \gtrsim 1$, particles radiate a notable fraction of their energy, and the likelihood of a spontaneous electron-positron pair creation in vacuum is markedly increased.

In LWFA, RR usually does not have a particular importance, because the RR force is significantly lower than the accelerating force. Nevertheless, RR can start to affect the electron dynamics, including betatron oscillations [201], in a multi-GeV energy regime, which might also be particularly important in multi-stage LWFA [202, 203]. When an electron, accelerated within the wake, enters the RR-dominated regime, an equilibrium is established between acceleration and RR. As indicated recently, the RR averaged over betatron oscillations saturates at a level smaller compared to the accelerating force [202].

Proposals for experiments that aim to analyze RR through the collision of a highly intense laser pulse with an electron beam frequently assume that the electron beam comes from an LWFA source. The primary reason is that one compact laser system can be used to generate both laser pulses: one that generates a wakefield and accelerates the electron beam, and the second one that collides with this electron beam, triggering RR effects on the electron. Some works consider this idea in theoretical proposals, e.g., Ref. [204], and it has been also already carried out experimentally, e.g., in Ref. [205].

Chapter 7

Towards applications

This chapter, comprised of two sections, is devoted to general outlooks of laser wakefield accelerators. In Section 7.1, potential applications of LWFA beams are discussed. Following that, Section 7.2 addresses the current challenges within the community that need to be addressed to introduce laser-plasma accelerators for these applications.

7.1 Applications of LWFA electron beams

In this section, promising applications of LWFA beams are described, namely electron-positron collider, medical applications, material probing, and applications of secondary X-ray sources.

7.1.1 Electron-positron collider

Plasma-based acceleration aspires to become a key technology for future colliders. Nowadays, the largest operating collider and accelerator is the well-known Large Hadron Collider (LHC) [206], located at the border of France and Switzerland. Employing conventional technologies, the collider with a 27-km-long circumference can accelerate protons up to 6.8 TeV, which corresponds to the collision energy of 13.6 TeV [207]. Following numerous milestones achieved by the LHC, including the experimental observation of the Higgs Boson [208], there is a growing interest within the scientific community in a larger collider with the potential to achieve even higher collision energies. The prevailing inclination is toward the development of a future collider based on e^- - e^+ collisions. A significant advantage is that, unlike hadrons, e^- and e^+ are non-composite particles, which means that the entire collision energy can be used to generate new particles and measurements can be more precise.

There are currently few prospects of colliders based on conventional technology. International linear collider (ILC) [209], most likely to be placed in Japan, is aimed to be a few tens of kilometers long and reach up to 200-500 GeV (extendable to 1 TeV) center-of-mass energies. There is also an aim to build new machines within the CERN complex. A new linear collider, named the Compact Linear Collider (CLIC) [210], with a length of ~ 11 km, should cover approximately the diameter of the current LHC [211]. At the initial stage, CLIC should be able to reach the collision energy of 380 GeV. There is a plan to increase the collision energy to 3 TeV later by increasing the accelerator length to more than 50 km [211]. Moreover, the next circular collider Future Circular Collider (FCC) is planned to be built around the LHC. The FCC examines scenarios for proton-

proton and heavy ion collisions, electron-positron collisions, proton-electron collisions, and proton-heavy ion collisions [212]. To reach the final goal of 100 TeV collision energy with radiofrequency acceleration, a 100 km circumference is needed, requiring at least a €21 billion budget just for the construction [213]. The space extensiveness and financial demandingness of the machines result in substantial interest in plasma-based technology, as has been also highlighted in several recent strategic reports for particle physics [214, 215].

Plasma-based lepton collider would not only lead to the compactness of the devices but the overall power consumption would be lowered by utilizing intrinsically short, few-fs long particle beams [216–218]. This reduction in beam duration would mitigate beamstrahlung [219], a source of radiation loss due to the emission of electromagnetic radiation by particles undergoing acceleration. A conceptual design of such a device has not yet been provided, however, preliminary studies have been already delivered, e.g., Ref. [220]. Community recommendations developed for the *Snowmass 2021 Accelerator Frontier* outlined the requirements for 1 TeV, 3 TeV, and 15 TeV colliders [219]. Some of the recommended parameters are listed in Table 7.1. There is also a debate about gamma-gamma collider where two photon beams would be utilized, generated by inverse Compton scattering from laser-plasma electrons [219].

Application	Requirements
Laser-plasma 1, 3, and 15 TeV e^- - e^+ colliders	$Q_e \sim 0.2$ nC $\Delta\mathcal{E}/\mathcal{E}_{\text{mean}} < 1\%$ $\varepsilon_n < 0.1$ μm Repetition rate ~ 50 kHz
Pre-clinical VHEE applications	$\mathcal{E}_{\text{mean}} \sim 150 - 200$ MeV $\Delta\mathcal{E}/\mathcal{E}_{\text{mean}} < 10\%$ $\varepsilon_n \approx 1$ μm
Ultrafast electron diffraction	$Q_e > 10$ fC $\mathcal{E}_{\text{mean}} \approx 3 - 5$ MeV $\Delta\mathcal{E}/\mathcal{E}_{\text{mean}} \approx 1\%$ $\varepsilon_n < 0.05$ μm Repetition rate > 100 Hz
XFEL	$Q_e \gtrsim 10$ pC $\Delta\mathcal{E}/\mathcal{E}_{\text{mean}} \sim 0.1\%$ $\varepsilon_n \sim 0.1$ μm Repetition rate ~ 10 -100 kHz

Table 7.1: Illustration of parameters required for certain applications of laser wakefield accelerators: a numerical example of parameters recommended for a TeV-range e^- - e^+ LWFA collider using plasma channels [219]; parameters of VHEE necessary for pre-clinical trials [221]; parameters for ultrafast electron diffraction [221]; general requirements for LWFA-based XFEL [222–224].

In principle, the electron-beam branch in an $e^- - e^+$ plasma-based collider could work as follows: An electron beam is firstly injected into damping rings to reach the required emittance. Subsequently, the plasma-based staged accelerator is used to bring the energies up to TeV ranges. In the staging process [225], several plasma cells followed by each other need to be implemented. The beam needs to be captured out of each plasma cell to be refocused into the next one while preserving its properties, such as emittance [226]. It is not yet clear if the stages will utilize a laser or particle driver beam to produce the plasma accelerating structure. However, simultaneous roadmaps have been proposed for the development of both technologies [227]. LWFA and PWFA share a lot of physics independent of the driver, and both strategies might benefit from each other [227]. Moreover, complementary laser and plasma wakefield advantages might lead to the utilization of hybrid LWFA-PWFA accelerators [228] in such next-generation experiments and science [229].

In any case, a plasma-based collider would require the generation of collider-quality e^- and e^+ beams, with relatively high charge but ultralow emittance, and preservation of these qualities, together with a high repetition rate [226, 230]. In this decade (2020s), laser-plasma community needs to demonstrate the staging of multi-GeV accelerators with Joule-class kHz laser systems. Collider systems such as positron source and injector, and cooling systems, should be addressed as well [219].

The overall goal is to generate TeV beams with the aforementioned quality. The acceleration of positrons in a plasma wake generated by a single positron beam has been already demonstrated experimentally [231]. However, the positron acceleration research is behind the electron acceleration and it will take a few more years to reach a similar quality for positrons. The reason is that the concepts developed for the multi-stage acceleration of an electron bunch do not automatically work for positrons. This is due to the fact that the transverse fields in plasma accelerating structures such as the LWFA bubble are usually naturally defocusing for positrons. Therefore, there are still many challenges to be overcome.

■ 7.1.2 Medical applications of relativistic electrons

Although the practical utilization of LWFA electron beams is at an early stage of development, there is a great intention to incorporate them into real-world medical applications, driven by their increasing reproducibility and availability. LWFA has unique properties that can be beneficial in medical applications, namely their short duration and high ionizing radiation dose [221]. Electrons with energies from 100 MeV to 250 MeV, commonly referred to as Very High Energy Electrons or VHEE, are suitable for radiotherapy.

A treatment arrangement could be possibly placed in a single treatment room, reducing the radiation time and treatment uncertainties compared to X-ray therapy [232]. Beam parameters can be controlled by changing the parameters of the laser and gas [232]. A dose of a few Gy should be delivered in less than a few minutes [233] and needs to be deposited within a reasonable amount of time over a projected surface of 3 cm^2 , which corresponds to a $\sim 10 \text{ nC}$ electron beam [221]. A recent experimental study has demonstrated that LWFA electrons can deliver up to 1.6 Gy dose to the target with a few hundred shots [234]. Another work demonstrated a clinically acceptable VHEE electron beam, with less than 1% charge uncertainty, which could deposit a total maximum dose of 65 Gy to the target area [235]. These results suggest that radiation in the range of therapeutic doses can

already be obtained with existing laser-plasma technology. Examples of some parameters of VHEE beams required before clinical trials are listed in Table 7.1.

In radiotherapy, in general, the probability of completely eliminating cancerous tissues is dependent on the dose, while the dose is simultaneously restricted by the risks of severe radiation-induced side effects [236]. This can be overcome with an arising method called flash radiotherapy (also FLASH, FLASHRT, or FLASH-RT) [237, 238], where the dose per time unit is greater than in conventional radiotherapy (40 Gy/s vs. 0.5–5 Gy/min, respectively) [233]. Better disease control with FLASH, with fewer side effects, was already supported by preclinical data [236]. According to *Transformative Technology for FLASH Radiation Therapy: A Snowmass 2021 White Paper* [239], LWFA might offer the most promising technology for compact and affordable VHEE medical machines that can operate in the ultrahigh ionization dose regime. Necessary electron energies are already generated and well controlled in laboratories, but the stability and reproducibility require further improvement. Limitations of lower repetition rates compared to conventional accelerators need to be addressed as well.

■ 7.1.3 Material probing with LWFA electrons

LWFA electrons can also provide ultrahigh temporal resolution in ultrafast probing experiments. Since the proof-of-principle electron radiography with an LWFA source was performed in the 2000s [240], several other demonstrations of the effect have been conducted [241–244]. Recently, the first single-shot electron radiography measurement using an electron source generated by the down-ramp injection has been demonstrated [244]. Another study examined laser-based radiography of various metallic and biological plant samples with two types of targets, Ar and He gas-jet targets [243]. It was discovered that, in this study, the DLA mechanism was responsible for acceleration in the case of the Ar target, while LWFA was present in the case of the He target. Radiography with LWFA beams is also interesting for plasma physics to probe sub-ps dynamics of plasma, e.g., relativistically expanding electromagnetic fields from the interaction of intense laser pulses with foil targets [242].

Moreover, a new method to probe the electric field structure of a wakefield has been invented [245], where a density modulation of an LWFA e^- probe that traverses the wake enables the wakefield reconstruction. LWFA is also very promising for probing materials at the atomic scale via ultrafast electron diffraction due to the femtosecond source that is inherently synchronized with the driver laser pulse [221]. This has been already demonstrated by measurements of the structural dynamics of single-crystal silicon nanomembranes pumped by an ultrafast laser pulse [246]. A concise list of requirements that need to be achieved to introduce ultrafast electron diffraction for applications is summarized in Table 7.1.

■ 7.1.4 Applications of secondary X-ray sources

Secondary X-rays from LWFA, described in Chapter 6, offer advantageous features for future applications, producing X-ray beams with a micrometer-scale source size, ultrashort duration, and energies in the range from keVs to hundreds of MeVs that are naturally synchronized with the drive laser pulse [31]. These unique properties can be employed, for instance, in medical, biological, and industrial imaging or radiography [31].

Here, we list some examples of potential applications.

Betatron radiation has several promising utilizations, for instance, phase-contrast imaging in the X-ray domain. X-ray phase-contrast imaging has recently led to a revolution in resolving power and tissue contrast in biomedical imaging, microscopy, and material science [247]. So far, progress in phase-contrast imaging has been held back mostly due to the lack of suitable X-ray sources with the necessary spatial coherence properties [248]. Although synchrotrons have proved to be the optimum source of spatially coherent X-rays [249], their extensive size and high cost limit their accessibility. In contrast, the LWFA betatron sources of reduced size, where the high spatial resolution is reached due to the small micrometer-scale source size, would be more accessible for common use in applications, e.g., hospitals and fundamental research small-scale laboratories. Typical peak energies generated by current LWFA experiments are already close to the ranges needed for various radiographic procedures, such as mammography [3]. X-ray phase-contrast imaging by the betatron sources has been demonstrated in proof-of-principle experiments, for instance, the static X-ray phase-contrast imaging of biological specimens [248] and a bone structure [250]. In addition, the betatron source enables detailed X-ray imaging of complex microstructures, e.g., irregularities in an aluminum-silicon system [251].

The intrinsic temporal resolution of betatron radiation is below 100 fs, indicating that significantly faster processes could be probed without compromising spatial resolution [252]. This enables direct observation of ultrafast radiation events in aqueous systems of chemical and biological interests [253–255]. Radiation with such properties can also provide time-resolved absorption spectroscopy at the fs scale for warm dense matter [256]. Moreover, ultrafast laser-driven shock waves in a silicon target have been analyzed by a betatron-generated radiograph [252].

Similarly to betatrons, Compton scattering sources have a transverse size in the order of microns. However, they are easier to tune, and, in case the electron energy spread is small, they can have a narrower bandwidth than betatron radiation [221]. They can deliver higher photon energies, from keVs up to 10s of MeV [31]. Therefore, Compton sources tend to find applications in slightly different areas, such as gamma-ray radiography, photofission, and possibly nuclear resonance fluorescence [31]. A compact tunable X-ray source based on inverse-Compton scattering with an electron beam from a laser wakefield has been demonstrated, e.g., in Ref. [257], where high-energy X-rays (>10 MeV) were produced in a narrow cone angle (5-10 mrad). The radiography with such a source can be, for instance, useful in the inspection of cargo containers and welded structures produced by large industries [31]. Another example of an experimental demonstration was a 6 MeV Compton X-ray beam generated with an LWFA electron source that provided high-quality imaging of a target composed of 8-mm thick depleted uranium shielded by 80-mm thick steel [258]. Moreover, a radiograph of a USB flash drive obtained with an LWFA-based Compton source was demonstrated with a $1.2\times$ magnification [259].

With bremsstrahlung radiation, it is possible to achieve the highest gamma-ray energies among the LWFA sources, up to 100s of MeV [31]. It has been already demonstrated that a <100 μm source, where photon energies can exceed 100 MeV, can be produced with a conversion efficiency of about 80% using a 0.5 mm-thick tantalum target [260]. A possible application of bremsstrahlung is non-destructive material testing, which is important for high-density metals such as steel or nickel that might contain small internal,

hardly detectable features. With the LWFA source, imaging with a resolution of 150 μm has been achieved on several samples, e.g., on a 5-cm thick nickel alloy [261]. A recent Monte Carlo simulation study has suggested that there is a potential to accumulate nuclear isomers by laser-driven photonuclear excitation using available LWFA e^- beams [262].

XFELs extend the capabilities of laser technology into the X-ray regime, offering a unique opportunity to combine ultraintense, ultrashort, coherent properties with those of X-ray light. These features can be utilized in several applications. For instance, XFELs can induce nonlinear X-ray interactions with matter [263], providing novel possibilities for studying materials and biological samples under extreme conditions. This is in contrast to conventional X-rays that trigger linear interactions and limit the interpretations of events under extreme conditions. It has been shown that the femtosecond response of small polyatomic molecules that contain one heavy atom to ultraintense, hard X-ray pulses from XFELs are qualitatively different than with soft or less intense hard X-rays [264], possibly leading to a more efficient description of local radiation damage that occurs on ultrashort timescales. Another example of the XFEL potential is the single-particle scattering imaging of protein molecules. Unique X-ray features enable the study of protein dynamics under conditions closely resembling physiological parameters without the need for their crystallization. This is beneficial since some types of proteins, such as membrane ones, are challenging and sometimes even impossible to crystallize [265].

■ 7.2 Current challenges in the LWFA field

In this section, some aspects that influence the performance of laser wakefield accelerators are discussed, and some current challenges are outlined.

■ 7.2.1 High-quality properties of electron beams

While low-emittance electron beams with low-energy spread are generally required for many utilizations, the specific characteristics of electron beams are inherently tied to the facility aimed at a particular application. For instance, hundreds-of-MeV scales with acceptable higher energy spread (see Table 7.1), sufficient for pre-clinical VHEE applications, correspond to state-of-art LWFA beams, routinely obtained in numerous laboratories worldwide [221]. In contrast, large-scale devices such as the e^- - e^+ collider or XFEL demand extremely low emittance and energy spread. In addition, a high charge is required for the collider. With the LWFA technology, charges in the order of hundreds of pC [5–7] and transverse emittance $\sim 0.1 \mu\text{m}$ [8, 9] have been obtained. However, reaching these values simultaneously in a collider-quality beam still remains a challenging task.

The initial parameters of electron beams are given by the injection process. For instance, it has been shown that the tuning of the optical injection parameters leads to the possibility of controlling the phase-space volume of the injected electrons [111]. Methods of electron injection and manipulation of the electron phase space have been continuously improved [266]. Controlled injection mechanisms offer more possibilities for tuning the final beam quality and provide perspective for further improvement, in general. As an example, a $\sim 0.5 \text{ nC}$ beam was obtained by self-truncated ionization injection [5]. In contrast, Barber et al. [9] demonstrated that down-ramp injection produces beams

with significantly better emittance ($0.5 \mu\text{m}$) compared to ionization injection ($1 \mu\text{m}$). However, both of these configurations showed clear dependence of the emittance on charge density that can be adequately tuned. The energy spread of $\sim 1\%$ was demonstrated already in 2009 with the optical injection method [111]. It seems that laboratories have been currently exploring the variety of injection techniques, determining their particular advantages.

The final parameters of electron beams are also significantly affected by the subsequent acceleration process, including the effect of beam loading [267–269]. Beam loading refers to alterations in the wakefield’s electric field caused by the presence of the accelerated electron beam. The accelerated beam introduces additional charge into the plasma, modifying the local electric fields and potentially slowing down the acceleration of subsequent electrons. However, it has been demonstrated experimentally that if the injected charge is appropriately controlled, beam loading can actually improve the performance by creating a plateau in the accelerating field, thereby minimizing energy spread [5]. In addition, specific complex wavefronts of the driver laser pulse might lead to better e^- beam parameters [270].

In principle, the quality of electron beams can be also tuned externally, outside the main LWFA stage during the beam transport, as will be also shortly discussed in the next subsection, Subsection 7.2.2. It seems that the interplay among the control of the injection process, acceleration process, and external beam manipulation can eventually lead to the desired beam quality based on the particular application.

■ 7.2.2 Diffraction, dephasing, depletion and accelerator staging

As the laser pulse travels through plasmas, it undergoes diffraction, resulting in a decrease in on-axis intensity and, consequently, a reduction in the acceleration gradient. This issue can be effectively addressed through the waveguiding in plasmas [271]. It has been shown that low-density plasma channels are suitable for guiding high-intensity laser beams over multiple Rayleigh lengths [271, 272]. With preformed plasma waveguides, the acceleration length and the energy gain for a given laser power can be increased, as was also demonstrated in the state-of-art LWFA energy record of 8 GeV [4].

As discussed in Section 3.3, the accelerated particle beam will eventually outrun the accelerating region of the wakefield due to the dephasing. Consequently, particles enter the decelerating phase and begin to lose energy. To mitigate this limitation challenge, one potential solution is the application of density tapering [170, 273–276]. This method involves increasing plasma density during the acceleration stage, thereby reducing λ_p , and preserving the phase of particles within the wakefield bucket. Moreover, injecting particles into several plasma periods behind the laser pulse offers an opportunity to extend the distance over which plasma density can be tapered [276]. Electrons can gradually travel into preceding plasma periods, gaining energy over multiple wake periods. Another alternative is the use of so-called flying focus [277, 278]. This technique employs a chromatic focusing system. The colors of the laser are arranged in time in order to propagate the focus over a distance potentially greatly exceeding the Rayleigh lengths [277]. Improvement of this method can be achieved using an axiparabola [279] and a novel echelon optic [278]. The axiparabola creates an extended focal region, and the echelon alters the temporal delay, making the wake phase velocity equal to c , preventing trapped electrons from surpassing the wake. Note that, unlike LWFA, PWFA

is not constrained by dephasing, as the relativistic driver particle beam has a velocity close to c , much higher than v_{Lg} (2.8). Nevertheless, this mechanism still requires another accelerator, in order to generate the particle drive beam.

A single stage of a laser-plasma accelerator is also ultimately limited by laser depletion [219]. There has been an alternative proposal for mitigating both depletion and dephasing, called traveling-wave electron acceleration (TWEAC), where the wakefield is generated by two ultrashort, pulse-front-tilted, obliquely incident laser beams in a line focus. The focal region moves with c , i.e., faster than v_{Lg} , so accelerated electrons cannot overtake the accelerating structure. Depletion is suppressed because the acceleration cavity is always generated by a previously unused section of the laser pulse in plasma regions previously unperturbed by the laser light.

In some experiments, notable additional energy loss was attributed to the transfer of energy to annular, ring-like electron structures inside or outside the wakefield. There are several reasons that can cause the formation of such rings, for instance, the splitting of an electron beam inside a wake bucket due to the creation of out-of-axis electron streams [280, 281], plasma wake elongation along a density down ramp with a non-Gaussian laser beam [282], high-divergence electrons originated on the boundaries of the wakefield structure [283, 284], or defocusing of a laser pulse [285].

Despite the promising solutions for mitigating diffraction, dephasing and depletion, for applications targeting energy ranges beyond 10 GeV, it appears highly likely that accelerator staging might be eventually employed. Implementing multiple acceleration stages proves effective in enhancing the final beam energy, a necessity for, e.g., laser-plasma colliders [220, 286]. The staging introduces challenges in transporting the electron beam between each successive stage. Quality-preserving transport is also crucial in the case of external injection, described in Subsection 4.4.5, where the beam is delivered from a conventional accelerator into the plasma accelerating section. The combination of extremely high energy, large divergence, and energy spread makes this problem challenging to be solved [287–289]. Quadrupoles and solenoids used in conventional accelerators are able to shape the beam, however, they do not improve the emittance [287]. If the electron beam comes with an energy spread from one stage, the transport can lead to large emittance growth. This is due to the difference in focusing forces between plasma and external optics [226]. Suitable transport might be reached by tailoring acceleration properties such as plasma density in order to match the phase spaces of the beams between two accelerator stages [289–293].

Steinke et al. [225] demonstrated a coupling of two laser-plasma stages, where electrons originally with 120 MeV from the first stage of LWFA gained additional ~ 100 MeV in the second acceleration stage by using another synchronized laser pulse. The electron beam generated in the first stage was transported to the second stage target using a pulsed active plasma lens [294, 295]. Plasma lensing is a technique, where an electron bunch propagates through a plasma, where focusing forces on the beam are induced. Plasma lens can be passive, in case the bunch self-focuses in plasma [296], or active, in case the focusing is provided by a pre-generated plasma structure, e.g. wakefield triggered by another driver [297, 298]. The active plasma lens can be also provided by applying a discharge current in a gas-filled capillary [295], the effect that has been broadly demonstrated for ion beams using z-pinches [294, 299, 300]. It is also possible to create a plasma lens when the density is higher than the plasma density (overdense regime), where the focusing

is provided by self-generated fields due to the background plasma shielding [301–303]. A discharge-capillary active plasma lens was used experimentally to focus 100-MeV-level electron beams from a laser-plasma accelerator [295]. Such lenses can reach tunable gradients of more than 3000 T/m, enabling the focusing of GeV-level electron beams over distances of a few cm [295].

■ 7.2.3 Reproducibility and tunability

One of the greatest challenges in LWFA is a highly sensitive dependence of electron beams on laser-plasma parameters, leading to difficulties with controlling the electron beam properties. Achieving robust reproducibility is essential for the effective operation of any particle accelerator. The possibility of tuning electron beam parameters by adjusting the experimental setup is also of great importance for the accelerator’s practicality. A well-chosen approach, such as a carefully selected injection method, might, in principle, improve stability and tunability. For instance, it has been shown experimentally [118, 304] and theoretically [305] that the down-ramp injection might be a good injection candidate to reach the required reproducibility. It provides the possibility of tuning the beam charge and energy by altering the plasma density profile.

However, it appears that this approach alone might not be sufficient, and additional sophisticated methods are necessary to effectively regulate laser-plasma parameters. As an example of such a method, research has demonstrated that shot-to-shot fluctuations can be effectively suppressed using a stable gas-filled capillary target. In this technique, the target gas is ionized by the wake-driving laser pulse, not by an electrical discharge [53]. Furthermore, implementing laser waveform control has been found to boost the stability of electron beams, as a strong dependence of stability and electron energy on the spectral phase has been detected [306]. The stability of laser parameters that determine the intensity in the focal spot will need to be improved as well. High repetition rate systems need to be explored for the implementation of feedback loops to provide automatic stabilization [221]. There have been successful reports to utilize statistical behavior from consecutive electron beams to analyze the correlations of laser and electron parameters, leading to a few percent stability of central energy [307]. Such a tool holds the potential to enable accelerator tunability through efficient feedback loops, independent of the specific details of the accelerator setup. Another study implemented a genetic algorithm to apply active feedback at a 5-Hz repetition rate by adjusting the temporal shape of the laser pulse automatically [308]. This resulted in an increase in the average charge and energy of electron beams. Examples of advances mentioned here show a promising path toward the LWFA stability improvement.

■ 7.2.4 Repetition rate

Several application goals require LWFA to operate at a high repetition rate (see, e.g., Table 7.1 for the collider, ultrafast electron diffraction, and XFEL). Currently, LWFA typically operates at a few Hz. To successfully demonstrate high-repetition-rate accelerators, high-average-power lasers operating at kHz repetition rates need to be developed over the next few years [221]. The repetition rate can be boosted by lowering the laser energy, as more laser pulses can be delivered in a time unit. This is a crucial issue to LWFA accelerators since it is favorable to reduce the laser pulse duration toward fs scales,

leading to single-cycle or few-cycle pulses. Electron acceleration at kHz repetition rate has already been demonstrated, e.g., in Refs [309–311]. Progress has led to energies in the tens of MeV range at the kHz regime achieved nowadays [311].

Another aspect of high-repetition rates is a restoration of the plasma source on kHz frequencies. It has been experimentally proven that hydrodynamic optical-field-ionized (HOFI) plasma channels [271, 312] can be generated at kHz-scale pulse repetition rates in a static gas cell and for an extended period as plasma recombines to form an approximately uniform-like gas within 1 ms [313]. Further advances in research and engineering on lasers and plasma that can be used for high-repetition-rate LWFA would lead us closer to applications.

■ 7.2.5 Improvement of X-ray sources

Secondary X-ray sources directly inherit complications of source electron beams. They also require several enhancements, mainly the stability and tunability of electron beams and increased radiation per energy unit [31]. A higher electron charge would increase the radiation gain, as each electron contributes to the overall radiation output.

In betatron radiation, in particular, the boost of betatron oscillation amplitude can also enhance the radiation gain. Such an amplitude growth can be induced, for example, by the interaction of the electron bunch with the rear part of the driving pulse [184, 185, 314], a tailored profile of the driving pulse [183, 315], a clustering gas jet target [316], long focal length optics [317], double injection in an evolving bubble [318], or external wiggler magnetic field [319]. Several studies have also shown that manipulation with the plasma density is also a promising method of betatron radiation enhancement [320–323]. Additionally, transverse electron oscillations can be boosted by extra DLA inside the LWFA bubble [324]. Moreover, the occurrence of ring electron beams caused by a non-Gaussian laser beam along the transverse density perturbations in a downramp can result in an order-of-magnitude increase in the measured X-ray emission [282]. This can be achieved by modifying the laser pulse chirp and duration [282].

A tunable narrowband Compton source of 0.05–2 MeV was demonstrated with $\sim 2 \times 10^7$ photons per second with a 10 Hz laser system [257]. The source characteristics could be further improved by increasing the energy of the scattering e^- beam, reducing the electron energy spread, improving the pointing of the laser and electron beams, and minimizing the fluctuations [257]. It has been demonstrated that for the bremsstrahlung source based on LWFA electron beams, the electron beam properties and a proper choice of target parameters can assure the tunability of the X-ray source size, divergence, energy range, and flux [325].

In addition, many X-ray sources, such as XFEL (see Table 7.1), require a high repetition rate (kHz and above) [221]. For XFEL, higher electron energy is also required to produce harder X-rays than the state-of-the-art 27 nm [189]. It is therefore probable that a portable compact LWFA-based XFEL will be once available, but presumably not in the very near future [31].

■ 7.2.6 Plasma-based acceleration of positrons

Positron acceleration awakens particular interest in the context of laser-based electron accelerators because of its direct application in the plasma-based collider, as described

above in Subsection 7.1.1. The acceleration of positrons still lags behind electrons by around a decade of concentrated research [226]. Compared to electrons, where many injection schemes extract electrons directly from plasma, for positrons, an external source is needed. In addition, typical accelerating structures generated by a particle or laser driver in plasmas, such as the bubble in the LWFA bubble regime, defocus positrons on the propagation axis [220, 226].

Regarding the generation of positrons, in addition to conventional sources (e.g., as in Ref. [326]), it is possible to use the capability of high-intensity lasers to generate positrons via several mechanisms [327]. For instance, in the nonlinear Breit-Wheeler process, a high-energy photon decays into an $e^- - e^+$ pair when interacting with multiple photons from the intense laser pulse. The high-energy gamma photon can be produced by the nonlinear inverse Compton scattering of an impinging electron beam on the laser light. This was experimentally demonstrated first (and up-to-date only), at the SLAC E144 experiment in 1997 [328], where a 46.6 GeV electron beam collided with a laser pulse of $\sim 10^{18}$ W/cm² intensity. The mechanism has been also widely studied by many theoretical works [329–342], motivated mainly by the development of cutting-edge multi-PW laser facilities [343–349]. Positrons can be also generated by the Bethe-Heitler process [350] during the irradiation of solid targets by a laser pulse [351–354] or an LWFA electron beam from a laser wakefield accelerator impinging on a solid target [355].

For laser-plasma positron acceleration, several concepts that can create simultaneous focusing and accelerating fields for positrons have been proposed. Such structures can be generated either by tailoring the driver laser beam [29, 356, 357] or plasma density profile [358–361]. In addition, a few experimental demonstrations of positron PWFA [172, 231, 359, 360, 362], where a positron beam was used as a driver, have been demonstrated. However, this scheme still requires a relativistic particle beam driver, referring back to the original complication.

There have been efforts to propose a one-stage generator and accelerator of positrons, e.g., by producing positrons by the Breit-Wheeler process directly inside the plasma wakefield [363]. Additionally, new regimes where positrons are created in an overdense target in a near-critical plasma or critical plasmas via linear Breit-Wheeler and subsequently accelerated have been invented [364, 365]. One-stage accelerator can also rely on the DLA process preceded by the nonlinear Breit-Wheeler process invoked by the same laser pulse [366].

The plethora of potential schemes seems to be promising in order to solve the situation with the positron arm in the plasma $e^- - e^+$ collider. While the positron laser-plasma acceleration is still at the beginning compared to electrons [226], research focus in this direction is highly motivated, as the future collider would significantly benefit if both accelerator arms were based on the new compact technology.

In this chapter, we have named possible applications of LWFA electrons and secondary X-ray sources and some of the main challenges that need to be addressed by the community. In the second part of this thesis, five concepts related to these aspects will be proposed.



Part II

Proposals of new concepts

Chapter 8

Methods: Particle-in-cell (PIC) simulations

In this chapter, the particle-in-cell (PIC) simulation method, which was used for studies in this work, will be briefly described. The basic principle will be discussed, followed by a concise overview of advanced PIC tools that can be useful to study important features of laser-plasma interaction. The codes utilized in this thesis, along with the general methodology, are also outlined.

8.1 Basics of the PIC method

Broadly speaking, there are two general approaches that can be employed to simulate laser-plasma interaction: the first one follows a fluid description, which operates with the equations of magnetohydrodynamics, and the second one relies on a kinetic description, which can be also used for plasma that is not in thermal equilibrium. In addition, hybrid combinations of these two methods have been developed.

The PIC method, based on the kinetic approach, is highly suitable for investigating laser-based acceleration. With PIC, it is possible to analyze non-equilibrium scenarios, including the generation of plasma waves, electron trapping, and acceleration. It also provides a useful tool for exploring the nonlinear effects that are challenging to model analytically. In this method, individual particles move in a continuous phase space, while the current and density distributions are computed at points of a stationary grid, consisting of numerous cells.

The PIC technique is based on the Vlasov equation, a collisionless form of the Boltzmann transport equation. It can be written as

$$\frac{\partial f_s}{\partial t} + \frac{\mathbf{p}}{\gamma m_s} \cdot \nabla f_s + \mathbf{F}_L \cdot \nabla_{\mathbf{p}} f_s = 0. \quad (8.1)$$

Phase space distribution function $f_s(\mathbf{x}, \mathbf{p}, t)$ is defined for each particle species s of mass m_s and Lorentz factor $\gamma = \sqrt{1 + |\mathbf{p}|^2 / (m_s^2 c^2)}$, where \mathbf{x} and \mathbf{p} are the position and momentum of a small phase-space element. The distribution function corresponds to the probability of finding a particle within a phase-space element $d\mathbf{x}$ and $d\mathbf{p}$ for position and momentum, respectively. ∇ and $\nabla_{\mathbf{p}}$ are the del operators with respect to $d\mathbf{x}$ and $d\mathbf{p}$. $\mathbf{F}_L = q_s(\mathbf{E} + \mathbf{v} \times \mathbf{B})$ is the Lorentz equation of motion, where q_s is the charge of a particle and $\mathbf{v} = \mathbf{p} / (\gamma m_s)$ is the velocity of a phase space element.

The PIC method does not directly solve the Vlasov equation for the entire distribution function, however, it effectively captures the dynamics of the system by tracking the motion of a representative ensemble of particles. It assumes that the distribution function of species s is given by the superposition of distribution functions f_k of all single particles of this species, k , with positions \mathbf{x}_k and momenta \mathbf{p}_k :

$$f_s = \sum_k f_k(\mathbf{x}_k, \mathbf{p}_k). \quad (8.2)$$

To handle the immense number of plasma particles in simulations, macroparticles are utilized, each assigned a statistical weight to represent a significant quantity of real particles clustered closely in phase space. Given that LWFA experiments commonly occur within the density range of approximately 10^{17} to 10^{19} cm^{-3} , this strategy proves highly beneficial. It circumvents the computational challenge associated with simulating an exceptionally large number of particles in such scenarios.

For each macroparticle, a specific functional form of particle weighting is, in the 6D phase space, assigned as

$$f_k(\mathbf{x}, \mathbf{p}, t) = N_k S_x(\mathbf{x} - \mathbf{x}_k(t)) S_p(\mathbf{p} - \mathbf{p}_k(t)). \quad (8.3)$$

S_x and S_p are shape functions of position and momentum, and N_k is the number of physical particles in the element of the phase space represented by the macroparticle. The spatial function can be factorized as

$$S_x(\mathbf{x} - \mathbf{x}_k(t)) = S_x(x - x_k(t)) S_y(y - y_k(t)) S_z(z - z_k(t)). \quad (8.4)$$

Here,

$$S_x(x - x_k(t)) = b_l \left(\frac{x - x_k}{\Delta x} \right), \quad (8.5)$$

where Δx is the scale length of the macroparticle in the x direction and b_l is the b -spline of the l -th order. S_y and S_z are defined accordingly. The spline of the 0th order is defined as follows:

$$\begin{aligned} b_0(x) &= 1 & \text{if } |x| < 1/2, \\ b_0(x) &= 0 & \text{otherwise.} \end{aligned} \quad (8.6)$$

The corresponding spatial function of Eq. (8.6) is commonly called "cloud in a cell" because the macroparticle forms a uniform square cloud in the phase space with an infinitesimal span in the momentum direction and a finite size in the space. The spline of order l is given by

$$b_l(x) = \int_{-\infty}^{\infty} dx' b_0(x - x') b_{l-1}(x'). \quad (8.7)$$

Functions of the first three orders are shown in Fig. 8.1. In PIC, higher-order splines are usually not used. Momentum shape function is typically described by the Delta function:

$$S_p(\mathbf{p} - \mathbf{p}_k(t)) = \delta(\mathbf{p} - \mathbf{p}_k(t)). \quad (8.8)$$

As a consequence, the spatial shape function remains constant in time. In the relativistic case, the equations of motion for a macroparticle k of species s moving in the electromagnetic field have the following form:

$$\frac{d\mathbf{x}_k}{dt} = \frac{\mathbf{p}_k}{\gamma_k m_s}, \quad (8.9)$$

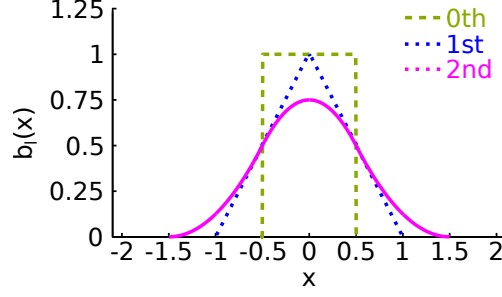


Figure 8.1: *B-spline functions (8.6), (8.7) of the first three orders: the 0th order (olive dashed), the 1st order (blue dotted), the 2nd order (magenta solid).*

$$\frac{d\mathbf{p}_k}{dt} = q_s \left(\mathbf{E}_k + \frac{\mathbf{p}_k}{\gamma_k m_s} \times \mathbf{B}_k \right), \quad (8.10)$$

where

$$\gamma_k = \sqrt{1 + \left(\frac{\mathbf{p}_k}{m_s c} \right)^2}. \quad (8.11)$$

Particle positions and momentum are typically calculated using a second-order integrator [367–369]. Fields \mathbf{E}_k and \mathbf{B}_k in Eq. (8.10) are the values of electric and magnetic field \mathbf{E} and \mathbf{B} interpolated to the macroparticle position, respectively. The calculation of \mathbf{E} and \mathbf{B} is performed at the points of a grid, created by discretizing the simulation domain. The fields are obtained from the Maxwell’s equations (3.14), completing the closed description for the Vlasov equation. Charge and current densities ρ_c and \mathbf{j} are deposited on the grid from the positions and momenta of macroparticles [370]:

$$\rho_c(x, t) = \sum_s \sum_k q_s N_k S_x(\mathbf{x} - \mathbf{x}_k(t)), \quad (8.12)$$

and

$$\mathbf{j}(x, t) = \sum_s \sum_k \frac{q_s}{\gamma_k m_k} \mathbf{p}_k N_k S_p(\mathbf{p} - \mathbf{p}_k(t)), \quad (8.13)$$

respectively. In summary, once the initial conditions for macroparticles and electromagnetic fields are set, the PIC algorithm generally consists of four main iterative steps, repeated until the end of the simulation (see also Fig. 8.2):

1. Compute charge and current densities in each cell from positions and velocities of macroparticles.
2. Compute fields from the densities obtained from the previous step.
3. Weight the fields and compute the Lorentz force, interpolating it from the grid back to the particle positions.
4. Advance the positions and velocities of macroparticles by one time step using the force from the previous step.

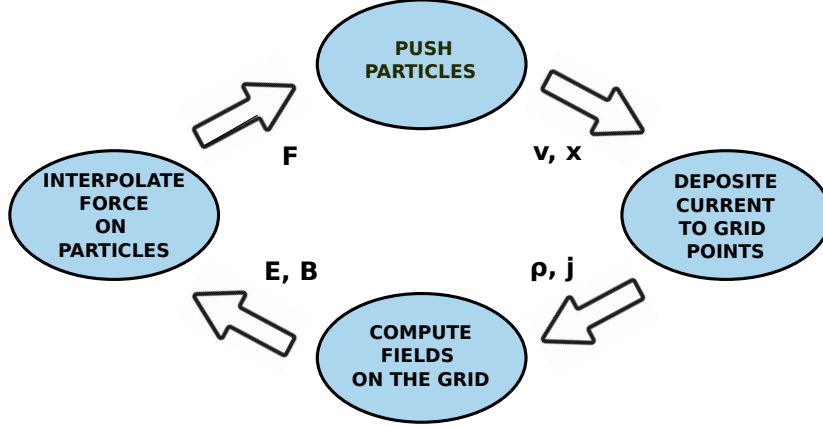


Figure 8.2: *The principle of the main loop of the PIC algorithm.*

The field equations are usually solved by the Finite-Difference Time-Domain (FDTD) method. A second-order scheme proposed by Yee in 1966 [371] is commonly used. In this scheme, the electric field components are calculated between the boundary points of each cell of the grid. The magnetic field components are located at the center of the cell faces. Time-centered field variables are needed to achieve second-order accuracy in current density calculations. The procedure for each timestep Δt is as follows:

1. Calculate the fields at $l + 1/2$ time:

$$\mathbf{E}^{l+1/2} = \mathbf{E}^l + \frac{\Delta t}{2} (c^2 \nabla_d \mathbf{B}^l - \mathbf{j}^l), \quad (8.14)$$

$$\mathbf{B}^{l+1/2} = \mathbf{B}^l - \frac{\Delta t}{2} (\nabla_d \mathbf{E}^{l+1/2}), \quad (8.15)$$

where ∇_d is a del operator on the Yee grid.

2. Calculate the current \mathbf{j}^{l+1} at $l + 1$ time.
3. Calculate the fields at $l + 1$ time:

$$\mathbf{B}^{l+1} = \mathbf{B}^{l+1/2} - \frac{\Delta t}{2} (\nabla_d \mathbf{E}^{l+1/2}), \quad (8.16)$$

$$\mathbf{E}^{l+1} = \mathbf{E}^{l+1/2} + \frac{\Delta t}{2} (c^2 \nabla_d \mathbf{B}^{l+1} - \mathbf{j}^{l+1}). \quad (8.17)$$

Despite its wide use, the Yee scheme may lead to the numerical dispersion of electromagnetic waves. The dispersion results in slower numerical group velocity than the real group velocity, which is a non-physical effect [372]. If a particle gains enough energy to exceed the numerical speed of light, significant errors may occur due to the new electromagnetic waves it emits. This effect was first described by Godfrey in 1974 [373]. It is called numerical Cherenkov instability, referring to the Cherenkov radiation [374], a well-known physical phenomenon. Simulations of LWFA can be also affected by this numerical effect.

Significant growth of the electron bunch emittance caused by this instability has been observed [375]. To suppress the numerical Cherenkov instability effect in the modeling of laser wakefield, schemes of higher order are commonly used nowadays, e.g., the one proposed by Lehe et al. [375]. This scheme can be utilized also with a moving simulation window. The moving window technique dynamically adjusts the simulation grid to follow particle movement, keeping the region of interest within the window. This method enhances the computational efficiency of simulations, making it a common choice for simulating the LWFA process. This preference is due to the fact that simulation times can extend to several picoseconds, whereas the area of interest usually spans only a few wakefield periods.

8.2 Additional modules for PIC codes

In order to consider additional physical effects that cannot be neglected in several cases of laser-plasma interaction, extra modules can be added into the main PIC loop, depicted in Fig. 8.2. These attributes need to be usually included directly in PIC codes as they influence the dynamics of particles in the simulation box. Examples of such features include the employment of particle collisions, ionization, radiation from particles, or electron-positron pair creation.

While typically not of great importance for laser-plasma acceleration, in some cases, e.g., for non-relativistic particles moving through a highly ionized plasma [376], binary collisions may play a significant role and, thus, cannot be neglected. In this case, the collision term in the Boltzmann transport equation can be simulated by adding the Monte Carlo algorithm [377–379] into the main PIC loop. In each timestep, the probability of a binary collision occurring between pairs of particles is computed. The pairs that are close enough to potentially interact are first determined. Subsequently, based on the Monte Carlo sampling, it is decided whether a collision occurs. In simple terms, this involves generating a random number between zero and one from the uniform distribution and comparing it to the calculated collision probability. If the number is smaller than the probability, a collision is assumed to happen, and the velocities of the colliding particles are modified accordingly.

To model the tunnel ionization, the Monte Carlo sampling is used in a similar manner, typically relying on the ionization rate in the quasi-static limit from the Ammosov-Delone-Krainov (ADK) theory [35, 380, 381]. In this approach, the probability of ionizing the ion macroparticle is calculated. If the event is accepted based on the Monte-Carlo sampling, a new macroelectron is created, having the same velocity as the ion macroparticle. Additionally, the ion charge is updated. Moreover, the code can also incorporate collisional ionization in a similar manner [382].

Modeling radiation inside the PIC loop is quite a challenging task since it significantly increases computational times. However, it is necessary in case the radiation reaction significantly affects the particle dynamics. The choice of the algorithm for computing radiation typically depends on the regime of radiation reaction [383, 384], described in Section 6.4. For arbitrary values of the quantum parameter (6.21), the Monte-Carlo description of discrete high-energy photon emission is efficient [385]. It is based on the creation of macropotons according to the rate of photon emission [386]. This approach is mandatory for the quantum regime, i.e., for $\chi_e \gtrsim 1$. For $\chi_e \ll 1$, Landau-Lifshitz

force (6.20) can be summed up with the Lorentz force and discretized directly within the PIC loop. Moreover, for semi-quantum regime $\chi_e \lesssim 1$, it is possible to add a stochastic diffusion force term to the equation to include the quantum effects [383].

Radiation can be also efficiently calculated outside the loop in case the energy of radiated photons is low and it has a negligible impact on the electron dynamics itself, such as in betatron oscillations. The intensity of radiation can be calculated numerically by Liénard-Wiechert potentials (Eqs. (6.1), (6.2)) in the far field [387–389]. Recently, the Liénard-Wiechert approach has been also considered to be implemented directly as a run-time diagnostic inside the PIC code, e.g., in Ref. [390].

The nonlinear Breit-Wheeler process of pair creation can be also treated with the Monte-Carlo method [385, 391–393]. The probability of creation of an e^- - e^+ pair is calculated according to the quantum parameter of photon

$$\chi_\gamma = \frac{|\hbar k_\mu F^{\mu\nu}|}{m_e c E_c}. \quad (8.18)$$

The parameter is defined analogously as for the electron in Eq. (6.21), and k_μ is the wave four-vector. If the pair creation based on random sampling occurs, new macroparticles of an electron and a positron are created at the position of the original macrophton.

8.3 Methodology employed in this work

As already mentioned, in this work, five separate publications are included in Appendix: Included publications. Three different particle-in-cell codes were utilized for these studies, namely the EPOCH [394], Smilei [69], and OSIRIS [395, 396] codes. All these codes are popular, state-of-the-art projects with very similar advantages. They are capable of high performances and massive parallelization, and thus, they are suitable for use on supercomputers. EPOCH and OSIRIS are written in Fortran. Smilei has been developed in C++, whereas the input files provided by users are adapted for the Python programming language. Simulations in these three codes can be run in 1D, 2D, and 3D, while Smilei and OSIRIS also offer a cylindrical geometry, with a possible decomposition into azimuthal modes (sometimes also called quasi-3D geometry). The codes feature several physics modules mentioned in Section 8.2, including binary collisions, ionization, radiation reaction (Monte Carlo QED module in all the codes, classical module in Smilei and OSIRIS, and semi-quantum module in Smilei), and the Breit-Wheeler process.

In Publication A, which studies self-injection into the wakefield generated by a non-Gaussian laser beam, and Publication D, which focuses on the enhancement of the betatron radiation, EPOCH was utilized. In addition, in order to calculate the radiation, in Publication D, the post-processing code based on the method described in Ref. [389] was used. Publication B and Publication C examine a novel optical injection technique with the Smilei code. These papers also include experimental results, which were performed by collaborators at the University of Nebraska-Lincoln (UNL) in the USA. The last study, Publication E, focuses on one-stage generation and laser-plasma acceleration of positrons, employing the OSIRIS code with the support of theoretical analysis.

In the simulations, a convention that the laser pulse is moving in the x direction is preserved. In case laser pulses propagate under an angle with respect to the main

axis (in Publication B and Publication C), they move in the $x - y$ plane, and they are also polarized in the $x - y$ plane. The exception is Publication E, where the laser pulse is moving in the z direction and is linearly polarized in the x direction. This arrangement was chosen to follow the same notation as the preceding work on the topic, carried out by Martinez et al. [366]. All the details including the laser-plasma setup and simulation parameters such as resolution are described in particular publications in detail.

In the next chapter, the contents of each of the publications are outlined and put into a broader context.

Chapter 9

Proposed concepts

In this chapter, the concepts introduced in this work are concisely summarized and explained. The corresponding publications are subsequently included in Appendix: Included publications.

9.1 Publication A: Laser wakefield accelerator driven by the super-Gaussian laser beam in the focus

The first concept presented here (see Publication A [397]) addresses the quality of the electron beam given by the injection mechanism in LWFA. In the standard transverse self-injection process in the bubble regime [28], a laser beam with a Gaussian spatial profile is employed, and injection occurs during the later stages of the laser beam propagation within plasma as a consequence of the laser beam evolution. The Gaussian shape of the laser beam is consistently maintained throughout its evolution in both the near field and far field.

The situation changes if the laser beam is focused into a super-Gaussian profile. The diffraction pattern of the super-Gaussian beam closely resembles that of a flat-top beam. Achieving the super-Gaussian profile at the focal area requires initial shaping of the beam in the far-field into an Airy disk. Subsequently, during defocusing, the spatial profile of the beam undergoes distinct alterations before reaching the Airy-disk pattern again. This transitional phase involves a temporary formation of a hollow-like laser beam.

If such a laser beam is focused into plasma, it creates a wakefield, similarly as in the case of the Gaussian beam. However, the wakefield reflects the evolution of the super-Gaussian beam accordingly, creating diverse density structures. The initial appearance of the temporary ring-like laser beam results in an on-axis stream of electrons within the first wakefield period. Nevertheless, due to the subsequent redistribution of intensity, with maximum intensity occurring on the axis, the electron stream initiates expansion within the wakefield, giving rise to a new bubble structure. During this transformation, the former bubble created behind the pulse is gradually replaced by the newly formed bubble. The new bubble expands rapidly during two separate stages, each lasting up to several hundreds of femtoseconds. Both expansions trigger transverse self-injections, where electrons sliding along the sheath of the new bubble are injected into the wakefield, similarly as in the transverse self-injection process observed in the bubble regime with a Gaussian beam.

The main constraint of the injection with a super-Gaussian beam is the necessity

of a complex spatio-temporal control of the laser profile to establish a stable super-Gaussian focus. Furthermore, the energy spread is higher than 1%, which is not sufficient for several prospective applications, such as the FEL, collider, or ultrafast diffraction (see Table 7.1). Despite this limitation, a notable advantage over the typical transverse self-injection is that the injection happens at the early stage of the laser beam propagation in plasma, immediately following the focusing process. This enables an extended acceleration time and a more precisely controlled localization of the injection process. The time-limited expansion of the new bubble is imprinted in the ultrashort duration of the electron beam, which is less than 2 fs RMS. Moreover, the high charge of the beam (~ 0.2 nC) indicates the potential for generating currents exceeding 100 kA.

9.2 Publication B: Transient Relativistic Plasma Grating to Tailor High-Power Laser Fields, Wakefield Plasma Waves, and Electron Injection

Publication B [398] presents a novel optical injection technique, demonstrated by experiment and PIC simulations. The injection of electrons into the laser wakefield is provided by a collision of two laser pulses intersecting at a small acute angle. The project was carried out in collaboration with Extreme Light Laboratory, University of Nebraska - Lincoln in the USA. The collaborators were responsible primarily for the experimental part of the project.

In this study, two nearly identical laser pulses, p-polarized in the x - y plane, collided under $\theta = 10^\circ$ angle in plasma. We assumed that each pulse propagated at $\theta/2 = 5^\circ$ angle with respect to the x axis. In order to demonstrate the process, we used the same parameters of the laser pulses in the simulations (normalized vector potential $a_0 = 1.3$, duration $\tau = 29$ fs). In the experiment, the normalized vector potentials and durations of the laser pulse 1 and 2 slightly varied from each other ($a_1 = 1.37$, $a_2 = 1.52$, and $\tau_1 = 39$ fs, $\tau_2 = 35$ fs, respectively). These discrepancies arose due to an imperfect split of the original pulse coming from the laser system into two pulses. This effect did not influence the general outcomes of the research.

As the laser pulses propagated in plasma, they both created their own wakefields. The collision caused a temporary interference of the two pulses, generating a standing wave in the y direction. The standing wave has wavelength $\lambda_I = \lambda_0/(2 \sin(\theta/2)) = 4.6 \mu\text{m}$, where λ_0 is the laser wavelength. Inside the plasma, the standing wave produces an electron grating. A theoretical, simulation and experimental study on the generation of the standing wave and the grating was presented in a conference proceedings paper in Ref. [399] (not included in this thesis).

The relativistic plasma grating dephases electrons that can end up trapped in multiple periods of the wakefields. The dynamics of this injection is influenced by relative delay τ_d between the intersecting laser pulses. In scenarios where one laser pulse slightly precedes the other (from $\tau_d \approx \tau_0$ up to $\tau_d \approx 2\tau_0$), electrons end up trapped in the leading wakefield. Here, we assume that the duration of the pulses is approximately the same, τ_0 , and put $\tau_0 = \tau_2$. The injection into one of the wakefields can be explained by the filamentation of the laser pulses induced by the electron grating. The filamentation consequently affected the wakefield shape and also its amplitude. As a result, the acceleration capability

of the wakefields is partially diminished due to the grating influence. Nevertheless, the front part of the leading laser pulse is less impacted by this grating because the grating predominantly forms at the area of the most intense laser intersection. In contrast, the delayed pulse experiences more significant filamentation during its passage through the plasma grating. The grating significantly impacts both the front and rear sections of the delayed pulse. This results in a situation where the leading pulse retains its ability to catch and accelerate electrons while the filamentation of the delayed pulse remarkably weakens its wakefield amplitude, mitigating its efficiency in electron trapping. The partial filamentation of the laser pulse and wakefield ahead was also imprinted in profiles of electron beams, both in simulation and experiment, where a splitting of electron beams was detected.

In the case of the on-time collision (from $\tau_d \approx 0$ up to $\tau_d \approx \tau_0$), the efficiency of the injection is comparably lower than in the case from $\tau_d \approx \tau_0$ up to $\tau_d \approx 2\tau_0$. This happens due to the fact that amplitudes of both wakefields are significantly affected by the interference. This effect was observed in simulations, which showed minimal trapping in both wakefields, with a slight preference for the leading wakefield. Similarly, experimental results showed a notably lower charge compared to the delayed collision. In the experimental on-time collision, the charge was nonnegligible exclusively in the wakefield ahead.

If the delay between the pulses exceeds approximately $2\tau_0$, the optical injection process ceases to occur due to a minimal overlap between the most intense sections of the laser pulses. The simulations reveal corresponding results. They also indicate that the collision can lead to the mutual injection into both wakefields in case the delay is $\tau_d > 1.2\tau$ if the interference is still sufficient enough to generate the plasma grating but it does not severely disrupt the delayed pulse. While this specific effect is not addressed in Publication B, it will be further explored in the subsequent Publication C, as outlined in Section 9.3.

This research represents the first demonstration of an optical injection induced by the collision of two laser pulses under an angle lower than 135° . A specific feature of this process is also the trapping of electrons into several wakefield periods (buckets), creating a train of electron beams separated approximately by a plasma wavelength. Moreover, injected electrons are trapped in wakefield buckets that are further behind the laser pulse, in contrast to more common injection into the first period. This can be utilized in combination with plasma density tapering to overcome the dephasing limit. As described in Subsection 7.2.2, by optimally modulating the plasma density, the electron beam injected into a wake bucket more distant from the driver laser pulse can be locked with the maximum acceleration phase for a longer distance [276].

9.3 Publication C: Injection of electron beams into two laser wakefields and generation of electron rings

The work contained in Publication C [400] is a follow-up research of the one described in the previous section, Section 9.2. In this subsequent study, we studied two specific phenomena that occurred during the experiments with the optical injection at the 10° collision angle, namely mutual injection into both wakefields and the generation of an

electron structure resembling a partial ring, occurring out-of-axis with respect to the main on-axis electron beam.

The majority of experimental observations indicate that electrons are typically captured either in one of the wakefields or not at all. However, in certain experimental runs, particularly when the delay between the laser pulses was $\tau_d \approx \tau_0$, a mutual injection into both wakefields was observed. In contrast, simulations suggest that this mutual injection is likely for delays ranging from 1.2τ to 2.2τ . In simulations, the occurrence of mutual injection appears to be a consequence of a relatively weak plasma grating. Such a grating results in less drastic alterations to the structures of wakefields compared to scenarios with shorter τ_d , including the wakefield that is delayed. Consequently, this facilitates the possibility of electrons being injected into both wakefields.

The mismatch between the simulation and experimental results can be caused by several factors. First of all, in the simulations, laser pulses with identical characteristics were chosen in order to grasp the fundamental principles of the process. In contrast, in the experiment, these parameters slightly differed, which could have affected the final comparison. In addition, the experimental inaccuracies were essentially affected by an unstable spatio-temporal laser profile and also by measurement inaccuracies. The pointing jitter of the laser pulses might have caused distinct results at particular experimental shots. Consequently, electron injection might have occurred in only one wakefield, contrary to the anticipated mutual injection under optimal, deviation-free conditions.

In addition, the spatio-temporal deviations of the laser profile were imprinted in the front-view profiles of the electron beams. Once the laser beam is directed slightly off the axis due to the experimental imperfection, this off-center positioning is also reflected in the spatial profile of the electron beam. As a result, the electron beam may exhibit a slight tilt with respect to the main axis of acceleration.

We also observed both in simulation and experiment that ring-like electron beams are generated out of the main axis of the delayed laser beam. The simulations revealed that the ring electrons also come from the collision of the laser beams. These are, similarly to the on-axis injected electrons, electrons that were dephased at the plasma grating. However, in contrast, these ring electrons were deflected from the center of the collision towards the wakefield of the delayed pulse but they were not captured in it. Consequently, they diverged from the main electron beam, escaping radially outward. The phenomenon of electrons forming a ring inside or outside the wakefield has been previously observed [280–285]. As discussed in Chapter 7, such rings might carry off a significant portion of the laser energy, energy that could otherwise contribute to the acceleration of the on-axis electron beam. Nevertheless, in scenarios where enhancing betatron radiation gain is the main goal, previous experiments indicate that additional annular electrons might provide the desirable boost [282].

■ 9.4 Publication D: Betatron radiation enhancement by a density up-ramp in the bubble regime of LWFA

Publication D [401] describes a method of increasing the betatron X-ray radiation gain from LWFA electrons. The technique is based on the application of a local density increase (up ramp) at later acceleration times. As stated in Subsection 7.2.2, an increase in plasma

density reduces λ_p and can keep particles at the rear part of the bubble [170, 273–276, 402]. Essentially, this energy boost has a potential to amplify the betatron radiation gain [322].

The presented publication unveils a novel simulation observation resulting from the employment of a density up ramp. When the density of the up ramp is sufficiently high, electrons travel behind the rear part of the bubble. The transverse electromagnetic fields in this region cause defocusing for electrons, leading to transverse spatial spread in the electron beam. If the modulation is precisely tuned to push the electron beam outside the bubble, allowing it to spread and then return to the rear part of the bubble, the betatron radiation gain can be notably boosted compared to the case without the up ramp. This enhancement stems not only from the energy increase at the rear part of the bubble, as mentioned above, but also from the growth of the betatron oscillation amplitude, a consequence of the temporary beam expansion behind the bubble.

To formulate the methodology for the experiments, a further thorough analysis is essential. Moreover, considering a potential impact of the 2D geometry on the bubble shape [403], additional analysis would also benefit from 3D simulations. The findings from this research have been documented in conference proceedings [401]. It is noteworthy that the technique was independently discovered and described in the dissertation of J. Ferri [404]. More extensive parametric simulation study is planned in future research.

9.5 Publication E: Radiation-dominated injection of positrons generated by the nonlinear Breit-Wheeler process into a plasma channel

The last concept presented here addresses the urge to examine positron acceleration in order to explore the feasibility of constructing a future plasma-based $e^- - e^+$ collider, as described in Subsection 7.2.6. The project was carried out within the collaboration with Group for Lasers and Plasmas of the Instituto de Plasmas e Fusão Nuclear at Instituto Superior Técnico in Lisbon, Portugal. The scheme presented in Publication E [405] proposes the generation and acceleration of positrons in one stage with a single highly intense laser pulse.

Initially, the positrons are generated by an orthogonal collision of a laser pulse and incident relativistic e^- beam, as a consequence of the Compton scattering and the subsequent Breit-Wheeler pair creation process. Positrons and electrons from the pairs inherit the momentum direction from the impinging e^- beam. In case the laser pulse is polarized in the e^- beam propagation, the newly generated electrons and positrons, with a nonzero initial momentum, travel in the direction of the laser pulse polarization, and eventually escape the finite spot size of the laser pulse. However, in contrast to counter-propagating geometry, some particles from the pairs can be deflected in the direction of the laser pulse propagation [331]. Such particles can travel with the laser pulse into a plasma channel, where they possibly undergo an energy boost by the DLA process (see Subsection 5.4). The advantage of the DLA process here is that an abundance of electrons from the plasma can be loaded on the laser axis, in addition to the ones originated from the pair creation. This accumulation of electrons acts as a mechanism to generate focusing fields for positrons along the propagation axis. The significant on-axis e^- charge changes

the sign of the initially defocusing fields inside the channel. This allows positrons to be maintained at the laser spot area for an extended time during acceleration. This setup is well described in the preceding research carried out by B. Martinez et al. [366]

The aim of Publication E was to investigate the process of positron injection into the plasma channel, or, in other words, what are the conditions for the deflection of positrons towards the plasma channel. In this context, "deflection" means that the positrons travel in the direction of the laser pulse propagation and remain confined within the laser spot. The first part of the work consists of a theoretical analysis of a positron motion in a plane wave with initial momentum in the direction of the wave polarization. The second part analyzes the process with a laser pulse focused into a small spot size via quasi-3D PIC simulations, which resembles more realistic experimental conditions. Both theoretical and simulation analysis lead to the conclusion that the probability of deflection increases with increasing intensity of the laser pulse. This outcome is attributed to the amplified impact of the radiation reaction recoil force at higher intensities. At such high intensities, the radiation reaction effectively counteracts the expulsive ponderomotive force, which leads to the on-axis radiative trapping of particles. For the parameters used in our work, the intensity of at least 2.2×10^{23} W/cm² would be required in order to inject more than 1% of positrons initially created. This intensity slightly exceeds the current world record of $(1.1 \pm 0.2) \times 10^{23}$ W/cm² [22].



Conclusion

LWFA represents a groundbreaking approach in the generation of ultrashort, relativistic electron beams over notably short distances, paving the way for the development of compact particle accelerators. The introduction of the LWFA method for practical utilization has become one of the main contemporary tasks for the laser-plasma community. Several applications, including the use of VHEE for medical purposes and specific uses of secondary X-ray sources, currently predominantly require advancements in the stability, reproducibility, and tunability of electron beams. Following these enhancements, the next step involves the demonstration of preliminary models and prototypes of such devices. On the other hand, other future prospects such as $e^- - e^+$ collider not only need to improve the stability factor but also elementary e^- beam parameters, such as emittance. A plethora of other attributes need to be considered as well, e.g., the particle beam transport or developing a positron accelerator with features equal to the electron counterpart. This thesis focuses on several aspects of the LWFA analysis, exploration, and improvement. It introduces novel concepts aimed at deepening our understanding of LWFA and increasing its efficiency, all examined through numerical PIC simulations.


First, production of a high-charge electron beam with femtosecond-scale duration and relatively low transverse emittance is presented. This is achieved through the creation of a super-Gaussian spatial profile at the laser focus. The electron beam is self-injected into the laser-created wakefield, which provides the accelerating gradient, during the early stages of the laser pulse propagation in plasma. A key aspect of this process is the specific evolution of the laser spatial profile during defocusing, which ensures effective injection. However, predicting the performance of this technique under real experimental conditions based on the simulation proposal remains currently challenging. The outcome would most likely highly depend on the stability of the spatio-temporal profile and ability to control very sensitive laser-beam shape at the focal spot. The mechanism might, therefore, benefit from the ongoing development of more stable laser systems and innovative techniques, including the integration of artificial intelligence. Potentially, more detailed studies may show a possible tunability of the setup based on the parameters of the laser pulse, such as the intensity or duration, as well as plasma density, similarly as in other injection schemes.

The next two studies incorporated in this work present a novel injection process involving the collision of two laser pulses at a 10° angle. When these pulses, polarized within their propagation plane, intersect, they create a temporary interference pattern. This pattern forms a plasma electron grid, which effectively dephases electrons. Depending on the relative delay between the pulses at their central collision point, electrons may

be trapped in one or both of the resulting wakefields or in neither. In this study, PIC simulations supported experimental results obtained by the collaborators at the University of Nebraska-Lincoln in the USA. The research highlights several noteworthy features of the LWFA injection. Namely, this is the first comprehensive experiment-simulation study of the LWFA optical injection where the collision is triggered at a small acute angle instead of a straight-like, obtuse angle. Next, electron trapping occurs at several periods of LWFA, not starting with the first period. This opens an opportunity to utilize a sequence of electron beams spaced by several microns. Moreover, by carefully tailoring the plasma density, the acceleration can be prolonged, and the final energy of electrons can be boosted. This can be achieved as electrons are progressively shifted to earlier wakefield periods, gradually accumulating energy in each of the periods. Furthermore, we observed off-axis ring-shaped electron structures, a phenomenon also noted previously as an attribute of other injection methods. In addition, this research contributes to a broader range of laser-plasma applications, suggesting that the temporary plasma grating might have implications for relativistic plasma optics.

This dissertation also introduces a technique aimed at enhancing betatron radiation, a secondary LWFA X-ray source, through plasma density modulation. It has been demonstrated that the intensity of radiation can be augmented by a local plasma density increase. This enhancement is caused either by electron energy gain at the rear part of the bubble or by an oscillation amplitude boost by fields behind the bubble. Future plans include a more in-depth exploration of this technique, specifically through comprehensive 3D simulations that will provide more detailed experimental guidelines. Furthermore, it could be worth exploring density down ramp injection as the initial injection mechanism. Although optical injection is utilized in the study presented here, a density down-ramp approach might offer greater experimental simplicity, as suggested by an independent study in Ref. [404]. The plasma source, likely a gas jet, could be designed to initially introduce a density modulation to initiate injection, followed by another density alteration in later stages of acceleration to enhance the radiation characteristics. This would bring experimental simplicity, as it relies solely on plasma density tailoring to both generate and improve the X-ray source.

The thesis concludes with a study of a one-stage process for both the generation and acceleration of positrons, a scheme potentially notable for a future e^- - e^+ collider. Electron-positron pair generation is achieved by an orthogonal collision of a multi-PW laser pulse and a GeV-scale e^- beam by the nonlinear Breit-Wheeler process. Positrons that are deflected in the direction of the laser pulse propagation can be injected into a plasma channel placed right after the area of the collision. Once in the channel, these positrons undergo acceleration through the direct laser acceleration process facilitated by the same laser pulse which was responsible for their initial generation. Simulations revealed that the radiation reaction resulting from the ultrahigh laser intensity plays a crucial role in the positron injection into the plasma channel. In the paper included here, the intensity of at least 2.2×10^{23} W/cm² was needed to accelerate more than 1% of positrons. At present, the tens-of-petawatts power scale required for an experimental setup with high deflection rates remains beyond reach. Furthermore, even if such power levels were achievable, the efficiency of the scheme might still not be outstanding. However, there is still a lot of potential for improving the setup. Investigating various interaction angles could reveal more optimal geometries for positron deflection. Moreover,



a higher electron charge of the incoming electron beam than considered in the presented work (10 pC) could be utilized. By increasing the charge of the incident electron beam tenfold, from 10 to 100 pC, the positron charge would be increased accordingly. Another alternative strategy might involve generating positrons through the Bethe-Heitler process. This would entail directing the laser beam onto a solid target with a plasma channel set up behind it, as opposed to utilizing a relativistic electron beam for pair generation. This technique could presumably increase the positron charge while simultaneously lowering the laser power demands. This particular approach has been extensively explored by collaborators at IST in Lisbon, Portugal, showing promising results.

In summary, this dissertation presents new concepts in the LWFA field, providing new perspectives and setting the groundwork for future explorations. It also builds the basis for practical uses in compact plasma particle acceleration. The upcoming decade is likely to reveal the future direction of LWFA, determining key factors that will drive its advancement not only in the realm of applications but also in our fundamental understanding of plasma physics.



Bibliography

1. Wiedemann, H. *Particle accelerator physics* (Springer Nature, 2015).
2. Tajima, T. & Dawson, J. M. Laser electron accelerator. *Physical Review Letters* **43**, 267 (1979).
3. Albert, F. & Thomas, A. G. R. Applications of laser wakefield accelerator-based light sources. *Plasma Physics and Controlled Fusion* **58**, 103001 (2016).
4. Gonsalves, A. J. *et al.* Petawatt laser guiding and electron beam acceleration to 8 GeV in a laser-heated capillary discharge waveguide. *Physical Review Letters* **122**, 084801 (2019).
5. Couperus, J. P. *et al.* Demonstration of a beam loaded nanocoulomb-class laser wakefield accelerator. *Nature Communications* **8**, 487 (2017).
6. Li, Y. F. *et al.* Generation of 20 kA electron beam from a laser wakefield accelerator. *Physics of Plasmas* **24**, 023108 (2017).
7. Xu, J. *et al.* Nanoparticle-insertion scheme to decouple electron injection from laser evolution in laser wakefield acceleration. *Scientific Reports* **12**, 11128 (2022).
8. Weingartner, R. *et al.* Ultralow emittance electron beams from a laser-wakefield accelerator. *Physical Review Special Topics-Accelerators and Beams* **15**, 111302 (2012).
9. Barber, S. K. *et al.* Measured emittance dependence on the injection method in laser plasma accelerators. *Physical Review Letters* **119**, 104801 (2017).
10. Vrbová, M., Jelínková, H. & Gavrilov, P. *Úvod do laserové techniky* (Vydavatelství ČVUT, 1998).
11. Laussade, J.-P. & Yariv, A. Analysis of mode locking and ultrashort laser pulses with a nonlinear refractive index. *IEEE Journal of Quantum Electronics* **5**, 435–441 (1969).
12. Paschotta, R. *Field Guide to Laser Pulse Generation* (SPIE Press, 2008).
13. Mocker, H. W. & Collins, R. J. Mode competition and self-locking effects in a Q-switched ruby laser. *Applied Physics Letters* **7**, 270–273 (1965).
14. Ippen, E. P. Principles of passive mode locking. *Applied Physics B* **58**, 159–170 (1994).
15. Renaudier, J. *et al.* Active and passive mode-locking in buried ridge mode-locked quantum dots Fabry-Perot semiconductor lasers in 2005 31st European Conference on Optical Communication, ECOC 2005 **3** (2005), 571–572.

16. Maiman, T. H. Stimulated Optical Radiation in Ruby. *Nature* **187**, 493–494 (1960).
17. DiDomenico Jr., M. Small-signal analysis of internal (coupling-type) modulation of lasers. *Journal of Applied Physics* **35**, 2870–2876 (1964).
18. Hargrove, L. E., Fork, R. L. & Pollack, M. A. Locking of He–Ne laser modes induced by synchronous intracavity modulation. *Applied Physics Letters* **5**, 4–5 (1964).
19. Strickland, D. & Mourou, G. Compression of amplified chirped optical pulses. *Optics Communications* **55**, 447–449 (1985).
20. Iparraguirre, I. *et al.* Wavelength tuning of Titanium Sapphire Laser by its own crystal birefringence. *Optics Express* **13**, 1254–1259 (2005).
21. Šulc, J. & Jelínková, H. *Solid-state lasers for medical applications* in *Lasers for medical applications* 127–176 (Elsevier, 2013).
22. Yoon, J. W. *et al.* Realization of laser intensity over 10^{23} W/cm². *Optica* **8**, 630–635 (2021).
23. *Press release: The Nobel Prize in Physics 2018*, 2024. <https://www.nobelprize.org/prizes/physics/2018/press-release/> (visited on January 19, 2024).
24. Wang, Z., Zhang, Z., Xu, Z. & Lin, Q. Space-time profiles of an ultrashort pulsed Gaussian beam. *IEEE Journal of Quantum Electronics* **33**, 566–573 (1997).
25. Ferri, J. *et al.* Effect of experimental laser imperfections on laser wakefield acceleration and betatron source. *Scientific Reports* **6**, 27846 (2016).
26. Nakanii, N. *et al.* Effect of halo on the stability of electron bunches in laser wakefield acceleration. *Europhysics Letters* **113**, 34002 (2016).
27. Cummings, P. & Thomas, A. G. R. A computational investigation of the impact of aberrated Gaussian laser pulses on electron beam properties in laser-wakefield acceleration experiments. *Physics of Plasmas* **18**, 053110 (2011).
28. Corde, S. *et al.* Observation of longitudinal and transverse self-injections in laser-plasma accelerators. *Nature Communications* **4**, 1501 (2013).
29. Vieira, J. & Mendonça, J. T. Nonlinear laser driven donut wakefields for positron and electron acceleration. *Physical Review Letters* **112**, 215001 (2014).
30. Zhang, G.-B. *et al.* Acceleration of on-axis and ring-shaped electron beams in wakefields driven by Laguerre-Gaussian pulses. *Journal of Applied Physics* **119**, 103101 (2016).
31. Albert, F. Principles and applications of x-ray light sources driven by laser wakefield acceleration. *Physics of Plasmas* **30**, 050902 (2023).
32. Nakamura, K. *et al.* Diagnostics, Control and Performance Parameters for the BELLA High Repetition Rate Petawatt Class Laser. *IEEE Journal of Quantum Electronics* **53**, 1–21 (2017).
33. Umstadter, D. Relativistic laser–plasma interactions. *Journal of Physics D: Applied Physics* **36**, R151 (2003).
34. Gibbon, P. *Short Pulse Laser Interactions with Matter: An Introduction* (Imperial College Press, 2005).

35. Ammosov, M. V., Delone, N. B. & Krainov, V. P. Tunnel ionization of complex atoms and of atomic ions in an alternating electromagnetic field. *Soviet Journal of Experimental and Theoretical Physics* **64**, 1191 (1986).
36. Sainadh, U. S. *et al.* Attosecond angular streaking and tunnelling time in atomic hydrogen. *Nature* **568**, 75–77 (2019).
37. Landsman, A. S. *et al.* Ultrafast resolution of tunneling delay time. *Optica* **1**, 343–349 (2014).
38. Kulhánek, P. *Úvod do teorie plazmatu* (AGA (Aldebaran Group for Astrophysics), 2011).
39. Kulhánek, P. *Blýskání* (AGA (Aldebaran Group for Astrophysics), 2011).
40. Chen, F. F. *Introduction to plasma physics* (Plenum Press, New York, 1974).
41. Vieira, J., Fonseca, R. A. & Silva, L. O. *Multidimensional Plasma Wake Excitation in the Non-linear Blowout Regime* in *Proceedings of the 2014 CAS-CERN Accelerator School: Plasma Wake Acceleration* **1** (2016), 79–107.
42. Esarey, E., Schroeder, C. B. & Leemans, W. P. Physics of laser-driven plasma-based electron accelerators. *Reviews of Modern Physics* **81**, 1229 (2009).
43. Sprangle, P., Esarey, E., Krall, J. & Joyce, G. Propagation and guiding of intense laser pulses in plasmas. *Physical Review Letters* **69**, 2200 (1992).
44. Chen, X. L. & Sudan, R. N. Two-dimensional self-focusing of short intense laser pulse in underdense plasma. *Physics of Fluids B: Plasma Physics* **5**, 1336–1348 (1993).
45. Esarey, E., Sprangle, P., Krall, J., Ting, A. & Joyce, G. Optically guided laser wake-field acceleration. *Physics of Fluids B: Plasma Physics* **5**, 2690–2697 (1993).
46. Chessa, P., Mora, P. & Antonsen Jr., T. M. Numerical simulation of short laser pulse relativistic self-focusing in underdense plasma. *Physics of Plasmas* **5**, 3451–3458 (1998).
47. Spence, D. J. & Hooker, S. M. Investigation of a hydrogen plasma waveguide. *Physical Review E* **63**, 015401 (2000).
48. Semushin, S. & Malka, V. High density gas jet nozzle design for laser target production. *Review of Scientific Instruments* **72**, 2961–2965 (2001).
49. Döpp, A. *et al.* 3D printing of gas jet nozzles for laser-plasma accelerators. *Review of Scientific Instruments* **87**, 073505 (2016).
50. Schmid, K. & Veisz, L. Supersonic gas jets for laser-plasma experiments. *Review of Scientific Instruments* **83**, 053304 (2012).
51. Lorenz, S. *et al.* Characterization of supersonic and subsonic gas targets for laser wakefield electron acceleration experiments. *Matter and Radiation at Extremes* **4**, 015401 (2019).
52. Clayton, C. E. *et al.* Self-guided laser wakefield acceleration beyond 1 GeV using ionization-induced injection. *Physical Review Letters* **105**, 105003 (2010).

53. Osterhoff, J. *et al.* Generation of Stable, Low-Divergence Electron Beams by Laser-Wakefield Acceleration in a Steady-State-Flow Gas Cell. *Physical Review Letters* **101**, 085002 (2008).
54. Vargas, M. *et al.* Improvements to laser wakefield accelerated electron beam stability, divergence, and energy spread using three-dimensional printed two-stage gas cell targets. *Applied Physics Letters* **104**, 174103 (2014).
55. Audet, T. L. *et al.* Investigation of ionization-induced electron injection in a wakefield driven by laser inside a gas cell. *Physics of Plasmas* **23**, 023110 (2016).
56. Audet, T. L. *et al.* Gas cell density characterization for laser wakefield acceleration. *Nuclear Instruments and Methods in Physics Research Section A: Accelerators, Spectrometers, Detectors and Associated Equipment* **909**, 383–386 (2018).
57. Kim, J. *et al.* Development of a density-tapered capillary gas cell for laser wakefield acceleration. *Review of Scientific Instruments* **92**, 023511 (2021).
58. Leemans, W. P. *et al.* GeV electron beams from a centimetre-scale accelerator. *Nature Physics* **2**, 696–699 (2006).
59. Nakamura, K. *et al.* GeV electron beams from a centimeter-scale channel guided laser wakefield accelerator. *Physics of Plasmas* **14**, 056708 (2007).
60. Karsch, S. *et al.* GeV-scale electron acceleration in a gas-filled capillary discharge waveguide. *New Journal of Physics* **9**, 415 (2007).
61. Abuazoum, S. *et al.* Linearly tapered discharge capillary waveguides as a medium for a laser plasma wakefield accelerator. *Applied Physics Letters* **100**, 014106 (2012).
62. Kim, M. S. *et al.* Characteristics of a tapered capillary plasma waveguide for laser wakefield acceleration. *Applied Physics Letters* **102**, 204103 (2013).
63. Bobrova, N. A. *et al.* Simulations of a hydrogen-filled capillary discharge waveguide. *Physical Review E* **65**, 016407 (2001).
64. Joshi, C. Laser-Driven Plasma Accelerators Operating in the Self-Guided, Blowout Regime. *IEEE Transactions on Plasma Science* **45**, 3134–3146 (2017).
65. Gorbunov, L. M. & Kirsanov, V. I. Excitation of plasma waves by an electromagnetic wave packet. *Soviet Journal of Experimental and Theoretical Physics* **93**, 509–518 (1987).
66. Esarey, E., Ting, A., Sprangle, P. & Joyce, G. The laser wakefield accelerator. *Comments on Plasma Physics and Controlled Fusion* **12**, 191–204 (1989).
67. Sprangle, P., Joyce, G., Esarey, E. & Ting, A. *Laser wakefield acceleration and relativistic optical guiding in AIP Conference Proceedings* **175** (1988), 231–239.
68. Dawson, J. M. Nonlinear electron oscillations in a cold plasma. *Physical Review* **113**, 383 (1959).
69. Derouillat, J. *et al.* Smilei: A collaborative, open-source, multi-purpose particle-in-cell code for plasma simulation. *Computer Physics Communications* **222**, 351–373 (2018).

70. Bulanov, S. V., Kirsanov, V. I. & Sakharov, A. S. Excitation of ultrarelativistic plasma waves by pulse of electromagnetic radiation. *Journal of Experimental and Theoretical Physics Letters* **50**, 198–201 (1989).
71. Sprangle, P., Esarey, E. & Ting, A. Nonlinear interaction of intense laser pulses in plasmas. *Physical Review A* **41**, 4463 (1990).
72. Sprangle, P., Esarey, E. & Ting, A. Nonlinear theory of intense laser-plasma interactions. *Physical Review Letters* **64**, 2011 (1990).
73. Berezhiani, V. I. & Murusidze, I. G. Relativistic wake-field generation by an intense laser pulse in a plasma. *Physics Letters A* **148**, 338–340 (1990).
74. Berezhiani, V. I. & Murusidze, I. G. Interaction of highly relativistic short laser pulses with plasmas and nonlinear wake-field generation. *Physica Scripta* **45**, 87 (1992).
75. Teychenné, D., Bonnaud, G. & Bobin, J.-L. Wave-breaking limit to the wake-field effect in an underdense plasma. *Physical Review E* **48**, R3248 (1993).
76. Esarey, E., Ting, A., Sprangle, P., Umstadter, D. & Liu, X. Nonlinear analysis of relativistic harmonic generation by intense lasers in plasmas. *IEEE Transactions on Plasma Science* **21**, 95–104 (1993).
77. Akhiezer, A. I. & Polovin, R. V. Theory of wave motion of an electron plasma. *Soviet Journal of Experimental and Theoretical Physics* **3**, 696–705 (1956).
78. Esarey, E. & Pilloff, M. Trapping and acceleration in nonlinear plasma waves. *Physics of Plasmas* **2**, 1432–1436 (1995).
79. Benedetti, C., Schroeder, C. B., Esarey, E., Rossi, F. & Leemans, W. P. Numerical investigation of electron self-injection in the nonlinear bubble regime. *Physics of Plasmas* **20**, 103108 (2013).
80. Li, X., Nghiem, P. A. P. & Mosnier, A. Toward low energy spread in plasma accelerators in quasilinear regime. *Physical Review Accelerators and Beams* **21**, 111301 (2018).
81. Pukhov, A., Gordienko, S., Kiselev, S. & Kostyukov, I. The bubble regime of laser–plasma acceleration: monoenergetic electrons and the scalability. *Plasma Physics and Controlled Fusion* **46**, B179 (2004).
82. Kostyukov, I., Pukhov, A. & Kiselev, S. Phenomenological theory of laser-plasma interaction in “bubble” regime. *Physics of Plasmas* **11**, 5256–5264 (2004).
83. Lu, W. *et al.* Generating multi-GeV electron bunches using single stage laser wakefield acceleration in a 3D nonlinear regime. *Physical Review Special Topics-Accelerators and Beams* **10**, 061301 (2007).
84. Lu, W. *Nonlinear plasma wakefield theory and optimum scaling for laser wakefield acceleration in the blowout regime* PhD thesis (University of California, Los Angeles, 2006).
85. Golovanov, A. A., Kostyukov, I. Y., Thomas, J. & Pukhov, A. Analytic model for electromagnetic fields in the bubble regime of plasma wakefield in non-uniform plasmas. *Physics of Plasmas* **24**, 103104 (2017).

86. Zobdeh, P., Sadighi-Bonabi, R. & Afarideh, H. Cavity generation and quasi-monoenergetic electron generation in laser-plasma interaction. *Physics of Particles and Nuclei Letters* **6**, 413–416 (2009).
87. Horný, V. *et al.* Optical injection dynamics in two laser wakefield acceleration configurations. *Plasma Physics and Controlled Fusion* **60**, 064009 (2018).
88. Golovanov, A. A., Kostyukov, I. Y., Thomas, J. & Pukhov, A. Beam loading in the bubble regime in plasmas with hollow channels. *Physics of Plasmas* **23**, 093114 (2016).
89. Cros, B. *Laser-driven Plasma Wakefield: Propagation Effects in Proceedings of the 2014 CAS-CERN Accelerator School: Plasma Wake Acceleration* **1** (2016), 207–230.
90. Kalmykov, S. Y., Gorbunov, L. M., Mora, P. & Shvets, G. Injection, trapping, and acceleration of electrons in a three-dimensional nonlinear laser wakefield. *Physics of Plasmas* **13**, 113102 (2006).
91. Yi, S., Khudik, V., Kalmykov, S. & Shvets, G. Hamiltonian analysis of electron self-injection and acceleration into an evolving plasma bubble. *Plasma Physics and Controlled Fusion* **53**, 014012 (2010).
92. Oguchi, A. *et al.* Multiple self-injection in the acceleration of monoenergetic electrons by a laser wake field. *Physics of Plasmas* **15**, 043102 (2008).
93. Golovin, G. *et al.* Generation of ultrafast electron bunch trains via trapping into multiple periods of plasma wakefields. *Physics of Plasmas* **27**, 033105 (2020).
94. Floettmann, K. Some basic features of the beam emittance. *Physical Review Special Topics-Accelerators and Beams* **6**, 034202 (2003).
95. Mangles, S. P. D. *et al.* Monoenergetic beams of relativistic electrons from intense laser–plasma interactions. *Nature* **431**, 535–538 (2004).
96. Geddes, C. G. R. *et al.* High-quality electron beams from a laser wakefield accelerator using plasma-channel guiding. *Nature* **431**, 538–541 (2004).
97. Faure, J. *et al.* A laser–plasma accelerator producing monoenergetic electron beams. *Nature* **431**, 541–544 (2004).
98. Bulanov, S. V., Pegoraro, F., Pukhov, A. & Sakharov, A. Transverse-wake wave breaking. *Physical Review Letters* **78**, 4205 (1997).
99. Tsung, F. S. *et al.* Near-GeV-energy laser-wakefield acceleration of self-injected electrons in a centimeter-scale plasma channel. *Physical Review Letters* **93**, 185002 (2004).
100. Kalmykov, S. Y. *et al.* Numerical modelling of a 10-cm-long multi-GeV laser wakefield accelerator driven by a self-guided petawatt pulse. *New Journal of Physics* **12**, 045019 (2010).
101. Banerjee, S. *et al.* Stable, tunable, quasimonoenergetic electron beams produced in a laser wakefield near the threshold for self-injection. *Physical Review Special Topics-Accelerators and Beams* **16**, 031302 (2013).
102. Umstadter, D., Kim, J. K. & Dodd, E. Laser injection of ultrashort electron pulses into wakefield plasma waves. *Physical Review Letters* **76**, 2073 (1996).

103. Esarey, E., Hubbard, R., Leemans, W., Ting, A. & Sprangle, P. Electron injection into plasma wakefields by colliding laser pulses. *Physical Review Letters* **79**, 2682 (1997).
104. Esarey, E., Schroeder, C. B., Leemans, W. & Hafizi, B. Laser-induced electron trapping in plasma-based accelerators. *Physics of Plasmas* **6**, 2262–2268 (1999).
105. Leemans, W. P. *et al.* Laser-driven plasma-based accelerators: Wakefield excitation, channel guiding, and laser triggered particle injection. *Physics of Plasmas* **5**, 1615–1623 (1998).
106. Schroeder, C. B., Lee, P., Wurtele, J., Esarey, E. & Leemans, W. Generation of ultrashort electron bunches by colliding laser pulses. *Physical Review E* **59**, 6037 (1999).
107. Fubiani, G., Esarey, E., Schroeder, C. & Leemans, W. Beat wave injection of electrons into plasma waves using two interfering laser pulses. *Physical Review E* **70**, 016402 (2004).
108. Faure, J. *et al.* Controlled injection and acceleration of electrons in plasma wakefields by colliding laser pulses. *Nature* **444**, 737–9 (2006).
109. Golovin, G. *et al.* Electron trapping from interactions between laser-driven relativistic plasma waves. *Physical Review Letters* **121**, 104801 (2018).
110. Hemker, R. G., Tzeng, K.-C., Mori, W., Clayton, C. & Katsouleas, T. Computer simulations of cathodeless, high-brightness electron-beam production by multiple laser beams in plasmas. *Physical Review E* **57**, 5920 (1998).
111. Rechatin, C. *et al.* Controlling the phase-space volume of injected electrons in a laser-plasma accelerator. *Physical Review Letters* **102**, 164801 (2009).
112. Kotaki, H. *et al.* Electron optical injection with head-on and countercrossing colliding laser pulses. *Physical Review Letters* **103**, 194803 (2009).
113. Corde, S. *et al.* Controlled betatron x-ray radiation from tunable optically injected electrons. *Physical Review Letters* **107**, 255003 (2011).
114. Lehe, R., Lifschitz, A., Davoine, X., Thaury, C. & Malka, V. Optical transverse injection in laser-plasma acceleration. *Physical Review Letters* **111**, 085005 (2013).
115. Horný, V., Petržílka, V., Klimo, O. & Krůs, M. Short electron bunches generated by perpendicularly crossing laser pulses. *Physics of Plasmas* **24**, 103125 (2017).
116. Chitgar, Z. M., Gibbon, P., Böker, J., Lehrach, A. & Büscher, M. Electron self-injection threshold for the tandem-pulse laser wakefield accelerator. *Physics of Plasmas* **27**, 023106 (2020).
117. Bulanov, S., Naumova, N., Pegoraro, F. & Sakai, J. Particle injection into the wave acceleration phase due to nonlinear wake wave breaking. *Physical Review E* **58**, R5257 (1998).
118. Hansson, M. *et al.* Down-ramp injection and independently controlled acceleration of electrons in a tailored laser wakefield accelerator. *Physical Review Special Topics-Accelerators and Beams* **18**, 071303 (2015).

119. Massimo, F., Lifschitz, A. F., Thaury, C. & Malka, V. Numerical study of laser energy effects on density transition injection in laser wakefield acceleration. *Plasma Physics and Controlled Fusion* **60**, 034005 (2018).
120. Geddes, C. G. R. *et al.* Plasma gradient controlled injection and postacceleration of high quality electron bunches in AIP Conference Proceedings **1086** (2009), 12–20.
121. Schmid, K. *et al.* Density-transition based electron injector for laser driven wakefield accelerators. *Physical Review Special Topics-Accelerators and Beams* **13**, 091301 (2010).
122. Faure, J., Rechatin, C., Lundh, O., Ammoura, L. & Malka, V. Injection and acceleration of quasimonoenergetic relativistic electron beams using density gradients at the edges of a plasma channel. *Physics of Plasmas* **17**, 083107 (2010).
123. Buck, A. *et al.* Shock-front injector for high-quality laser-plasma acceleration. *Physical Review Letters* **110**, 185006 (2013).
124. Swanson, K. *et al.* Electron beam control using shock-induced density downramp injection in AIP Conference Proceedings **1812** (2017), 040004.
125. Xu, J. *et al.* Dynamics of electron injection in a laser-wakefield accelerator. *Physics of Plasmas* **24**, 083106 (2017).
126. McGuffey, C. *et al.* Ionization induced trapping in a laser wakefield accelerator. *Physical Review Letters* **104**, 025004 (2010).
127. Pak, A. *et al.* Injection and trapping of tunnel-ionized electrons into laser-produced wakes. *Physical Review Letters* **104**, 025003 (2010).
128. Mirzaie, M. *et al.* Demonstration of self-truncated ionization injection for GeV electron beams. *Scientific Reports* **5**, 14659 (2015).
129. Zhao, Q. *et al.* Ionization injection in a laser wakefield accelerator subject to a transverse magnetic field. *New Journal of Physics* **20**, 063031 (2018).
130. Shen, B. *et al.* Electron injection by a nanowire in the bubble regime. *Physics of Plasmas* **14**, 053115 (2007).
131. Cho, M. H., Pathak, V. B., Kim, H. T. & Nam, C. H. Controlled electron injection facilitated by nanoparticles for laser wakefield acceleration. *Scientific Reports* **8**, 16924 (2018).
132. Aniculaesei, C. *et al.* Proof-of-principle experiment for nanoparticle-assisted laser wakefield electron acceleration. *Physical Review Applied* **12**, 044041 (2019).
133. Marchetti, B., Assmann, R., Dorda, U. & Zhu, J. Conceptual and technical design aspects of accelerators for external injection in LWFA. *Applied Sciences* **8**, 757 (2018).
134. Luttkikhof, M. J. H., Khachatryan, A., Van Goor, F. & Boller, K.-J. The effect of the vacuum-plasma transition and an injection angle on electron-bunch injection into a laser wakefield. *Physics of Plasmas* **14**, 083101 (2007).
135. Gregocki, D., Maslarova, D. & Krus, M. *Transition of electron beams between vacuum and plasma in the external injection into a laser wakefield accelerator in Laser Acceleration of Electrons, Protons, and Ions VII* **12579** (2023), 43–52.

136. Rossi, A. R. *et al.* The external-injection experiment at the SPARC_LAB facility. *Nuclear Instruments and Methods in Physics Research Section A: Accelerators, Spectrometers, Detectors and Associated Equipment* **740**, 60–66 (2014).
137. Weikum, M. *et al.* Improved electron beam quality from external injection in laser-driven plasma acceleration at SINBAD in *Proceeding of the International Particle Accelerator Conference, IPAC* **17** (2017), 1707–1710.
138. Walker, P. A. *et al.* Horizon 2020 EuPRAXIA design study in *Journal of Physics: Conference Series* **874** (2017), 012029.
139. Boella, E., Corner, L., Holloway, J. & Silva, T. External injection in laser wakefield acceleration at the CLARA accelerator facility: a preparatory study in *APS Division of Plasma Physics Meeting Abstracts* **2019** (2019), TP10.024.
140. Thaury, C. *et al.* Shock assisted ionization injection in laser-plasma accelerators. *Scientific Reports* **5**, 16310 (2015).
141. Zeng, M. *et al.* Multichromatic Narrow-Energy-Spread Electron Bunches from Laser-Wakefield Acceleration with Dual-Color Lasers. *Physical Review Letters* **114**, 084801 (2014).
142. Chen, M., Sheng, Z.-M., Ma, Y.-Y. & Zhang, J. Electron injection and trapping in a laser wakefield by field ionization to high-charge states of gases. *Journal of Applied Physics* **99**, 056109 (2006).
143. Rosenbluth, M. N. & Liu, C. S. Excitation of plasma waves by two laser beams. *Physical Review Letters* **29**, 701 (1972).
144. Amiranoff, F. *et al.* Observation of modulational instability in Nd-laser beat-wave experiments. *Physical Review Letters* **68**, 3710 (1992).
145. Schroeder, C. B., Benedetti, C., Esarey, E., Chen, M. & Leemans, W. Two-color ionization injection using a plasma beatwave accelerator. *Nuclear Instruments and Methods in Physics Research Section A: Accelerators, Spectrometers, Detectors and Associated Equipment* **909**, 149–152 (2018).
146. Nakajima, K. Plasma-wave resonator for particle-beam acceleration. *Physical Review A* **45**, 1149 (1992).
147. Umstadter, D., Esarey, E. & Kim, J. Nonlinear plasma waves resonantly driven by optimized laser pulse trains. *Physical Review Letters* **72**, 1224 (1994).
148. Hooker, S. M. *et al.* Multi-pulse laser wakefield acceleration: a new route to efficient, high-repetition-rate plasma accelerators and high flux radiation sources. *Journal of Physics B: Atomic, Molecular and Optical Physics* **47**, 234003 (2014).
149. Tomassini, P. *et al.* The resonant multi-pulse ionization injection. *Physics of Plasmas* **24**, 103120 (2017).
150. Joshi, C., Tajima, T., Dawson, J., Baldis, H. & Ebrahim, N. Forward Raman instability and electron acceleration. *Physical Review Letters* **47**, 1285 (1981).
151. Andreev, N. Resonant excitation of wakefields by a laser pulse. *Journal of Experimental and Theoretical Physics Letters* **55**, 571–576 (1992).
152. Antonsen Jr., T. M. & Mora, P. Self-focusing and Raman scattering of laser pulses in tenuous plasmas. *Physical Review Letters* **69**, 2204 (1992).

153. Antonsen Jr., T. M. & Mora, P. Self-focusing and Raman scattering of laser pulses in tenuous plasmas. *Physics of Fluids B: Plasma Physics* **5**, 1440–1452 (1993).
154. Esarey, E., Krall, J. & Sprangle, P. Envelope analysis of intense laser pulse self-modulation in plasmas. *Physical Review Letters* **72**, 2887 (1994).
155. Batani, D., Joachain, C. J., Martellucci, S. & Chester, A. N. *Atoms, solids, and plasmas in super-intense laser fields* (Springer Science + Business Media, 2001).
156. Pukhov, A. & Meyer-ter-Vehn, J. Relativistic laser-plasma interaction by multi-dimensional particle-in-cell simulations. *Physics of Plasmas* **5**, 1880–1886 (1998).
157. Pukhov, A., Sheng, Z.-M. & Meyer-ter-Vehn, J. Particle acceleration in relativistic laser channels. *Physics of Plasmas* **6**, 2847–2854 (1999).
158. King, P. M. *et al.* Predominant contribution of direct laser acceleration to high-energy electron spectra in a low-density self-modulated laser wakefield accelerator. *Physical Review Accelerators and Beams* **24**, 011302 (2021).
159. Shaw, J. L. *et al.* Role of direct laser acceleration of electrons in a laser wakefield accelerator with ionization injection. *Physical Review Letters* **118**, 064801 (2017).
160. Shaw, J. L., Lemos, N., Marsh, K., Froula, D. & Joshi, C. Experimental signatures of direct-laser-acceleration-assisted laser wakefield acceleration. *Plasma Physics and Controlled Fusion* **60**, 044012 (2018).
161. Hussein, A. E. *et al.* Towards the optimisation of direct laser acceleration. *New Journal of Physics* **23**, 023031 (2021).
162. Khudik, V., Arefiev, A., Zhang, X. & Shvets, G. Universal scalings for laser acceleration of electrons in ion channels. *Physics of Plasmas* **23**, 103108 (2016).
163. Ji, L. L., Pukhov, A., Kostyukov, I. Y., Shen, B. & Akli, K. Radiation-reaction trapping of electrons in extreme laser fields. *Physical Review Letters* **112**, 145003 (2014).
164. Gong, Z., Mackenroth, F., Yan, X. & Arefiev, A. Radiation reaction as an energy enhancement mechanism for laser-irradiated electrons in a strong plasma magnetic field. *Scientific Reports* **9**, 17181 (2019).
165. Yeh, I. L., Tangtartharakul, K., Rinderknecht, H., Willingale, L. & Arefiev, A. Strong interplay between superluminosity and radiation friction during direct laser acceleration. *New Journal of Physics* **23**, 095010 (2021).
166. Jirka, M., Vranic, M., Grismayer, T. & Silva, L. Scaling laws for direct laser acceleration in a radiation-reaction dominated regime. *New Journal of Physics* **22**, 083058 (2020).
167. Babjak, R., Willingale, L., Arefiev, A. & Vranic, M. *Efficient direct laser acceleration by multi-petawatt lasers*, 2023. arXiv: 2304.10469 [physics.plasm-ph]. (visited on January 19, 2024).
168. Chen, P., Dawson, J., Huff, R. W. & Katsouleas, T. Acceleration of electrons by the interaction of a bunched electron beam with a plasma. *Physical Review Letters* **54**, 693 (1985).
169. Rosenzweig, J. B. *et al.* Experimental observation of plasma wake-field acceleration. *Physical Review Letters* **61**, 98 (1988).

170. Katsouleas, T. Physical mechanisms in the plasma wake-field accelerator. *Physical Review A* **33**, 2056 (1986).
171. Adli, E. *et al.* Acceleration of electrons in the plasma wakefield of a proton bunch. *Nature* **561**, 363–367 (2018).
172. Blue, B. E. *et al.* Plasma-wakefield acceleration of an intense positron beam. *Physical Review Letters* **90**, 214801 (2003).
173. Litos, M. *et al.* High-efficiency acceleration of an electron beam in a plasma wakefield accelerator. *Nature* **515**, 92–95 (2014).
174. Deng, A. *et al.* Generation and acceleration of electron bunches from a plasma photocathode. *Nature Physics* **15**, 1156–1160 (2019).
175. Pompili, R. *et al.* Energy spread minimization in a beam-driven plasma wakefield accelerator. *Nature Physics* **17**, 499–503 (2021).
176. Jackson, J. D. *Classical Electrodynamics* (John Wiley & Sons, 2007).
177. Hogan, M. J. *et al.* E-157: A 1.4-m-long plasma wake field acceleration experiment using a 30 GeV electron beam from the Stanford Linear Accelerator Center Linac. *Physics of Plasmas* **7**, 2241–2248 (2000).
178. Esarey, E., Shadwick, B., Catravas, P. & Leemans, W. Synchrotron radiation from electron beams in plasma-focusing channels. *Physical Review E* **65**, 056505 (2002).
179. Kostyukov, I., Kiselev, S. & Pukhov, A. X-ray generation in an ion channel. *Physics of Plasmas* **10**, 4818–4828 (2003).
180. Rouse, A. *et al.* Production of a keV X-ray beam from synchrotron radiation in relativistic laser-plasma interaction. *Physical Review Letters* **93**, 135005 (2004).
181. Phuoc, K. T. *et al.* Imaging electron trajectories in a laser-wakefield cavity using betatron X-ray radiation. *Physical Review Letters* **97**, 225002 (2006).
182. Kneip, S. *et al.* Observation of synchrotron radiation from electrons accelerated in a petawatt-laser-generated plasma cavity. *Physical Review Letters* **100**, 105006 (2008).
183. Mangles, S. P. D. *et al.* Controlling the spectrum of x-rays generated in a laser-plasma accelerator by tailoring the laser wavefront. *Applied Physics Letters* **95**, 181106 (2009).
184. Nemeth, K. *et al.* Laser-driven coherent betatron oscillation in a laser-wakefield cavity. *Physical Review Letters* **100**, 095002 (2008).
185. Cipiccia, S. *et al.* Gamma-rays from harmonically resonant betatron oscillations in a plasma wake. *Nature Physics* **7**, 867 (2011).
186. Madey, J. M. J. Stimulated emission of bremsstrahlung in a periodic magnetic field. *Journal of Applied Physics* **42**, 1906–1913 (1971).
187. Pellegrini, C., Marinelli, A. & Reiche, S. The physics of x-ray free-electron lasers. *Reviews of Modern Physics* **88**, 015006 (2016).
188. Pandey, S. *et al.* Time-resolved serial femtosecond crystallography at the European XFEL. *Nature Methods* **17**, 73–78 (2020).

189. Wang, W. *et al.* Free-electron lasing at 27 nanometres based on a laser wakefield accelerator. *Nature* **595**, 516–520 (2021).
190. Labat, M. *et al.* Seeded free-electron laser driven by a compact laser plasma accelerator. *Nature Photonics* **17**, 150–156 (2023).
191. Arutyunian, F. R. & Tumanian, V. A. The Compton effect on relativistic electrons and the possibility of obtaining high energy beams. *Physics Letters* **4**, 176–178 (1963).
192. Rykovanov, S. G. *et al.* Quasi-monoenergetic femtosecond photon sources from Thomson Scattering using laser plasma accelerators and plasma channels. *Journal of Physics B: Atomic, Molecular and Optical Physics* **47**, 234013 (2014).
193. Albert, F. *et al.* Design of narrow-band Compton scattering sources for nuclear resonance fluorescence. *Physical Review Special Topics-Accelerators and Beams* **14**, 050703 (2011).
194. Muşat, V., Latina, A. & D’Auria, G. A high-energy and high-intensity inverse Compton scattering source based on CompactLight technology. *Photonics* **9**, 308 (2022).
195. Glinec, Y. *et al.* High-resolution γ -ray radiography produced by a laser-plasma driven electron source. *Physical Review Letters* **94**, 025003 (2005).
196. Abraham, M. *Theorie der Elektrizität: Elektromagnetische Theorie der Strahlung* (Teubner, 1905).
197. Dirac, P. A. M. *Classical theory of radiating electrons* in *Proceedings of the Royal Society of London. Series A. Mathematical and Physical Sciences* **167** (1938), 148–169.
198. Landau, L. D. & Lifshitz, E. M. *The Classical Theory of Fields, The Course of Theoretical Physics* (Butterworth-Heinemann, Oxford, 1987).
199. Blackburn, T. G. Radiation reaction in electron–beam interactions with high-intensity lasers. *Reviews of Modern Plasma Physics* **4**, 5 (2020).
200. Di Piazza, A. Exact solution of the Landau-Lifshitz equation in a plane wave. *Letters in Mathematical Physics* **83**, 305–313 (2008).
201. Zeng, M. & Seto, K. Radiation reaction of betatron oscillation in plasma wakefield accelerators. *New Journal of Physics* **23**, 075008 (2021).
202. Golovanov, A. A., Nerush, E. N. & Kostyukov, I. Y. Radiation reaction-dominated regime of wakefield acceleration. *New Journal of Physics* **24**, 033011 (2022).
203. Saberi, H., Xia, G., Islam, M. R., Liang, L. & Davut, C. Radiation reaction and its impact on plasma-based energy-frontier colliders. *Physics of Plasmas* **30**, 043104 (2023).
204. Thomas, A. G. R., Ridgers, C., Bulanov, S., Griffin, B. & Mangles, S. Strong radiation-damping effects in a gamma-ray source generated by the interaction of a high-intensity laser with a wakefield-accelerated electron beam. *Physical Review X* **2**, 041004 (2012).
205. Poder, K. *et al.* Experimental signatures of the quantum nature of radiation reaction in the field of an ultraintense laser. *Physical Review X* **8**, 031004 (2018).

-
206. Evans, L. & Bryant, P. LHC machine. *Journal of Instrumentation* **3**, S08001 (2008).
 207. Albanese, R. *et al.* Observation of collider muon neutrinos with the SND@LHC experiment. *Physical Review Letters* **131**, 031802 (2023).
 208. Aad, G. *et al.* Observation of a new particle in the search for the Standard Model Higgs boson with the ATLAS detector at the LHC. *Physics Letters B* **716**, 1–29 (2012).
 209. Adolphsen, C. *et al.* *The International Linear Collider Technical Design Report - Volume 3.II: Accelerator Baseline Design*, 2013. arXiv: 1306.6328 [physics.acc-ph]. (visited on January 19, 2024).
 210. Wilson, I. The compact linear collider CLIC. *Physics Reports* **403**, 365–378 (2004).
 211. Brunner, O. *et al.* *The CLIC project*, 2022. arXiv: 2203.09186 [physics.acc-ph]. (visited on January 19, 2024).
 212. CERN. *The Future Circular Collider*, 2023. <https://home.cern/science/accelerators/future-circular-collider> (visited on November 14, 2023).
 213. Castelvechi, D. & Gibney, E. *CERN makes bold push to build €21-billion supercollider*, 2020. <https://www.nature.com/articles/d41586-020-01866-9> (visited on November 30, 2023).
 214. Adolphsen, C. *et al.* European Strategy for Particle Physics – Accelerator R&D Roadmap. *CERN Yellow Reports: Monographs* **1**, 1–270 (2022).
 215. Butler, J. N. *et al.* *Report of the 2021 U.S. Community Study on the Future of Particle Physics (Snowmass 2021) Summary Chapter*, 2023. arXiv: 2301.06581 [hep-ex]. (visited on January 19, 2024).
 216. Lundh, O. *et al.* Few femtosecond, few kiloampere electron bunch produced by a laser-plasma accelerator. *Nature Physics* **7**, 219–222 (2011).
 217. Buck, A. *et al.* Real-time observation of laser-driven electron acceleration. *Nature Physics* **7**, 543–548 (2011).
 218. Zhang, C. J. *et al.* Temporal characterization of ultrashort linearly chirped electron bunches generated from a laser wakefield accelerator. *Physical Review Accelerators and Beams* **19**, 062802 (2016).
 219. Schroeder, C. B. *et al.* Linear colliders based on laser-plasma accelerators. *Journal of Instrumentation* **18**, T06001 (2023).
 220. Schroeder, C. B., Esarey, E., Geddes, C., Benedetti, C. & Leemans, W. P. Physics considerations for laser-plasma linear colliders. *Physical Review Special Topics-Accelerators and Beams* **13**, 101301 (2010).
 221. Albert, F. *et al.* 2020 roadmap on plasma accelerators. *New Journal of Physics* **23**, 031101 (2021).
 222. Yampolsky, N. *et al.* *Feasibility study for the hard x-ray free electron laser based on synergistic use of conventional and plasma accelerator technologies*, 2022. arXiv: 2210.16425 [physics.acc-ph]. (visited on January 19, 2024).

223. Emma, C. *et al.* Free electron lasers driven by plasma accelerators: status and near-term prospects. *High Power Laser Science and Engineering* **9**, e57 (2021).
224. Lu, W. *Towards Future Light Sources and Colliders: the Promises and Challenges for the Plasma Based Accelerators*. Presented at USTC, Hefei, China. 2019.
225. Steinke, S. *et al.* Multistage coupling of independent laser-plasma accelerators. *Nature* **530**, 190–193 (2016).
226. Joshi, C., Corde, S. & Mori, W. B. Perspectives on the generation of electron beams from plasma-based accelerators and their near and long term applications. *Physics of Plasmas* **27**, 070602 (2020).
227. Antonsen, T. *et al.* *Advanced Accelerator Development Strategy Report: DOE Advanced Accelerator Concepts Research Roadmap Workshop* tech. rep. (U.S. DOE Office of Science, Washington, DC, United States, 2016).
228. Hidding, B. *et al.* Monoenergetic energy doubling in a hybrid laser-plasma wakefield accelerator. *Physical Review Letters* **104**, 195002 (2010).
229. Hidding, B. *et al.* *Progress in hybrid plasma wakefield acceleration in Photonics* **10** (2023), 99.
230. Joshi, C. *et al.* Plasma wakefield acceleration experiments at FACET II. *Plasma Physics and Controlled Fusion* **60**, 034001 (2018).
231. Corde, S. *et al.* Multi-gigaelectronvolt acceleration of positrons in a self-loaded plasma wakefield. *Nature* **524**, 442–445 (2015).
232. Kokurewicz, K. *et al.* *Laser-plasma generated very high energy electrons (VHEEs) in radiotherapy in Medical Applications of Laser-Generated Beams of Particles IV: Review of Progress and Strategies for the Future* **10239** (2017), 61–69.
233. Hughes, J. R. & Parsons, J. L. FLASH radiotherapy: current knowledge and future insights using proton-beam therapy. *International Journal of Molecular Sciences* **21**, 6492 (2020).
234. Labate, L. *et al.* Toward an effective use of laser-driven very high energy electrons for radiotherapy: Feasibility assessment of multi-field and intensity modulation irradiation schemes. *Scientific Reports* **10**, 17307 (2020).
235. Svendsen, K. *et al.* A focused very high energy electron beam for fractionated stereotactic radiotherapy. *Scientific Reports* **11**, 5844 (2021).
236. Matuszak, N. *et al.* FLASH Radiotherapy: an emerging approach in radiation therapy. *Reports of Practical Oncology and Radiotherapy* **27**, 343–351 (2022).
237. Favaudon, V. *et al.* Ultrahigh dose-rate FLASH irradiation increases the differential response between normal and tumor tissue in mice. *Science Translational Medicine* **6**, 245ra93 (2014).
238. Bourhis, J. *et al.* Treatment of a first patient with FLASH-radiotherapy. *Radiotherapy and Oncology* **139**, 18–22 (2019).
239. Boucher, S. *et al.* *Transformative Technology for FLASH Radiation Therapy: A Snowmass 2021 White Paper*, 2022. arXiv: 2203.11047 [physics.med-ph]. (visited on January 19, 2024).

240. Mangles, S. P. D. *et al.* Table-top laser-plasma acceleration as an electron radiography source. *Laser and Particle Beams* **24**, 185–190 (2006).
241. Ramanathan, V. *et al.* Submillimeter-resolution radiography of shielded structures with laser-accelerated electron beams. *Physical Review Special Topics-Accelerators and Beams* **13**, 104701 (2010).
242. Schumaker, W. *et al.* Ultrafast electron radiography of magnetic fields in high-intensity laser-solid interactions. *Physical Review Letters* **110**, 015003 (2013).
243. Hazra, D., Mishra, S., Moorti, A. & Chakera, J. Electron radiography with different beam parameters using laser plasma accelerator. *Physical Review Accelerators and Beams* **22**, 074701 (2019).
244. Falk, K. *et al.* Laser-driven low energy electron beams for single-shot ultra-fast probing of meso-scale materials and warm dense matter. *Scientific Reports* **13**, 4252 (2023).
245. Zhang, C. J. *et al.* Femtosecond probing of plasma wakefields and observation of the plasma wake reversal using a relativistic electron bunch. *Physical Review Letters* **119**, 064801 (2017).
246. He, Z.-H. *et al.* Capturing structural dynamics in crystalline silicon using chirped electrons from a laser wakefield accelerator. *Scientific Reports* **6**, 36224 (2016).
247. Wenz, J. *et al.* Quantitative X-ray phase-contrast microtomography from a compact laser-driven betatron source. *Nature Communications* **6**, 7568 (2015).
248. Kneip, S. *et al.* X-ray phase contrast imaging of biological specimens with femtosecond pulses of betatron radiation from a compact laser plasma wakefield accelerator. *Applied Physics Letters* **99**, 093701 (2011).
249. Suortti, P. & Thomlinson, W. Medical applications of synchrotron radiation. *Physics in Medicine & Biology* **48**, R1 (2003).
250. Cole, J. M. *et al.* Laser-wakefield accelerators as hard x-ray sources for 3D medical imaging of human bone. *Scientific Reports* **5**, 13244 (2015).
251. Hussein, A. E. *et al.* Laser-wakefield accelerators for high-resolution X-ray imaging of complex microstructures. *Scientific Reports* **9**, 3249 (2019).
252. Wood, J. C. *et al.* Ultrafast imaging of laser driven shock waves using betatron x-rays from a laser wakefield accelerator. *Scientific Reports* **8**, 11010 (2018).
253. Oulianov, D. A. *et al.* Ultrafast pulse radiolysis using a terawatt laser wakefield accelerator. *Journal of Applied Physics* **101**, 053102 (2007).
254. Malka, V. *et al.* Principles and applications of compact laser-plasma accelerators. *Nature Physics* **4**, 447–453 (2008).
255. Gauduel, Y. A., Glinec, Y., Rousseau, J.-P., Burgy, F. & Malka, V. High energy radiation femtochemistry of water molecules: early electron-radical pairs processes. *The European Physical Journal D* **60**, 121–135 (2010).
256. Mahieu, B. *et al.* Probing warm dense matter using femtosecond X-ray absorption spectroscopy with a laser-produced betatron source. *Nature Communications* **9**, 3276 (2018).

257. Banerjee, S. *et al.* Compact source of narrowband and tunable X-rays for radiography. *Nuclear Instruments and Methods in Physics Research Section B: Beam Interactions with Materials and Atoms* **350**, 106–111 (2015).
258. Chen, S. *et al.* Shielded radiography with a laser-driven MeV-energy X-ray source. *Nuclear Instruments and Methods in Physics Research Section B: Beam Interactions with Materials and Atoms* **366**, 217–223 (2016).
259. Ta Phuoc, K. *et al.* All-optical Compton gamma-ray source. *Nature Photonics* **6**, 308–311 (2012).
260. Ben-Ismaïl, A., Faure, J. & Malka, V. Optimization of gamma-ray beams produced by a laser-plasma accelerator. *Nuclear Instruments and Methods in Physics Research Section A: Accelerators, Spectrometers, Detectors and Associated Equipment* **629**, 382–386 (2011).
261. Underwood, C. I. D. *et al.* Development of control mechanisms for a laser wakefield accelerator-driven bremsstrahlung x-ray source for advanced radiographic imaging. *Plasma Physics and Controlled Fusion* **62**, 124002 (2020).
262. Lan, H.-Y. *et al.* Photonuclear production of nuclear isomers using bremsstrahlung induced by laser-wakefield electrons. *Nuclear Science and Techniques* **34**, 74 (2023).
263. Doumy, G. *et al.* Nonlinear atomic response to intense ultrashort x rays. *Physical Review Letters* **106**, 083002 (2011).
264. Rudenko, A. *et al.* Femtosecond response of polyatomic molecules to ultra-intense hard X-rays. *Nature* **546**, 129–132 (2017).
265. Bielecki, J., Maia, F. R. N. C. & Mancuso, A. P. Perspectives on single particle imaging with x rays at the advent of high repetition rate x-ray free electron laser sources. *Structural Dynamics* **7**, 040901 (2020).
266. Jiang, K., Wang, W., Feng, K. & Li, R. *Review of Quality Optimization of Electron Beam Based on Laser Wakefield Acceleration in Photonics* **9** (2022), 511.
267. Katsouleas, S., Wilks, T. & Su, J. D. J. Beam loading efficiency in plasma accelerators. *Particle Accelerators* **22**, 81–99 (1987).
268. Tzoufras, M. *et al.* Beam loading in the nonlinear regime of plasma-based acceleration. *Physical Review Letters* **101**, 145002 (2008).
269. Tzoufras, M. *et al.* Beam loading by electrons in nonlinear plasma wakes. *Physics of Plasmas* **16**, 056705 (2009).
270. Oumbarek Espinos, D. *et al.* Notable improvements on LWFA through precise laser wavefront tuning. *Scientific Reports* **13**, 18466 (2023).
271. Shaloo, R. J. *et al.* Low-density hydrodynamic optical-field-ionized plasma channels generated with an axicon lens. *Physical Review Accelerators and Beams* **22**, 041302 (2019).
272. Miao, B., Feder, L., Shrock, J., Goffin, A. & Milchberg, H. Optical guiding in meter-scale plasma waveguides. *Physical Review Letters* **125**, 074801 (2020).
273. Bulanov, S. V. *et al.* Laser acceleration of charged particles in inhomogeneous plasmas. I. *Plasma Physics Reports* **23**, 259–269 (1997).

274. Pukhov, A. & Kostyukov, I. Control of laser-wakefield acceleration by the plasma-density profile. *Physical Review E* **77**, 025401 (2008).
275. Sprangle, P. *et al.* Wakefield generation and GeV acceleration in tapered plasma channels. *Physical Review E* **63**, 056405 (2001).
276. Rittershofer, W., Schroeder, C., Esarey, E., Grüner, F. & Leemans, W. Tapered plasma channels to phase-lock accelerating and focusing forces in laser-plasma accelerators. *Physics of Plasmas* **17**, 063104 (2010).
277. Froula, D. H. *et al.* Flying focus: Spatial and temporal control of intensity for laser-based applications. *Physics of Plasmas* **26**, 032109 (2019).
278. Palastro, J. P. *et al.* Dephasingless laser wakefield acceleration. *Physical Review Letters* **124**, 134802 (2020).
279. Smartsev, S. *et al.* Axiparabola: a long-focal-depth, high-resolution mirror for broadband high-intensity lasers. *Optics Letters* **44**, 3414–3417 (2019).
280. Pollock, B. B. *et al.* Formation of ultrarelativistic electron rings from a laser-wakefield accelerator. *Physical Review Letters* **115**, 055004 (2015).
281. Maitrallain, A. *et al.* Parametric study of high-energy ring-shaped electron beams from a laser wakefield accelerator. *New Journal of Physics* **24**, 013017 (2022).
282. Zhao, T. Z. *et al.* High-flux femtosecond x-ray emission from controlled generation of annular electron beams in a laser wakefield accelerator. *Physical Review Letters* **117**, 094801 (2016).
283. Yang, X. *et al.* Three electron beams from a laser-plasma wakefield accelerator and the energy apportioning question. *Scientific Reports* **7**, 43910 (2017).
284. Behm, K. *et al.* Measurements of electron beam ring structures from laser wakefield accelerators. *Plasma Physics and Controlled Fusion* **61**, 065012 (2019).
285. Valenta, P., Grittani, G. M., Lazzarini, C. M., Klimo, O. & Bulanov, S. V. On the electromagnetic-electron rings originating from the interaction of high-power short-pulse laser and underdense plasma. *Physics of Plasmas* **28**, 122104 (2021).
286. Leemans, W. & Esarey, E. Laser-driven plasma-wave electron accelerators. *Physics Today* **62**, 44–49 (2009).
287. Antici, P. *et al.* Laser-driven electron beamlines generated by coupling laser-plasma sources with conventional transport systems. *Journal of Applied Physics* **112**, 044902 (2012).
288. Migliorati, M. *et al.* Intrinsic normalized emittance growth in laser-driven electron accelerators. *Physical Review Special Topics-Accelerators and Beams* **16**, 011302 (2013).
289. Floettmann, K. Adiabatic matching section for plasma accelerated beams. *Physical Review Special Topics-Accelerators and Beams* **17**, 054402 (2014).
290. Xu, X. L. *et al.* Physics of phase space matching for staging plasma and traditional accelerator components using longitudinally tailored plasma profiles. *Physical Review Letters* **116**, 124801 (2016).

291. Ariniello, R., Doss, C., Hunt-Stone, K., Cary, J. & Litos, M. Transverse beam dynamics in a plasma density ramp. *Physical Review Accelerators and Beams* **22**, 041304 (2019).
292. Mehrling, T., Grebenyuk, J., Tsung, F., Floettmann, K. & Osterhoff, J. Transverse emittance growth in staged laser-wakefield acceleration. *Physical Review Special Topics-Accelerators and Beams* **15**, 111303 (2012).
293. Dornmair, I., Floettmann, K. & Maier, A. R. Emittance conservation by tailored focusing profiles in a plasma accelerator. *Physical Review Special Topics-Accelerators and Beams* **18**, 041302 (2015).
294. Panofsky, W. K. H. & Baker, W. R. A focusing device for the external 350-MeV proton beam of the 184-inch cyclotron at Berkeley. *Review of Scientific Instruments* **21**, 445–447 (1950).
295. Van Tilborg, J. *et al.* Active plasma lensing for relativistic laser-plasma-accelerated electron beams. *Physical Review Letters* **115**, 184802 (2015).
296. Kuschel, S. *et al.* Demonstration of passive plasma lensing of a laser wakefield accelerated electron bunch. *Physical Review Accelerators and Beams* **19**, 071301 (2016).
297. Lehe, R., Thaury, C., Guillaume, E., Lifschitz, A. & Malka, V. Laser-plasma lens for laser-wakefield accelerators. *Physical Review Special Topics-Accelerators and Beams* **17**, 121301 (2014).
298. Thaury, C. *et al.* Demonstration of relativistic electron beam focusing by a laser-plasma lens. *Nature Communications* **6**, 6860 (2015).
299. Boggasch, E. *et al.* Z-pinch plasma lens focusing of a heavy-ion beam. *Physical Review Letters* **66**, 1705 (1991).
300. Dothan, F., Riege, H., Boggasch, E. & Frank, K. Dynamics of a z pinch for focusing high-energy charged particles. *Journal of Applied Physics* **62**, 3585–3591 (1987).
301. Rosenzweig, J. B. *et al.* Demonstration of electron beam self-focusing in plasma wake fields. *Physics of Fluids B: Plasma Physics* **2**, 1376–1383 (1990).
302. Nakanishi, H. *et al.* Direct observation of plasma-lens effect. *Physical Review Letters* **66**, 1870 (1991).
303. Hairapetian, G. *et al.* Transverse dynamics of a short, relativistic electron bunch in a plasma lens. *Physics of Plasmas* **2**, 2555–2561 (1995).
304. Geddes, C. G. R. *et al.* Plasma-density-gradient injection of low absolute-momentum-spread electron bunches. *Physical Review Letters* **100**, 215004 (2008).
305. Ekerfelt, H., Hansson, M., Gallardo González, I., Davoine, X. & Lundh, O. A tunable electron beam source using trapping of electrons in a density down-ramp in laser wakefield acceleration. *Scientific Reports* **7**, 12229 (2017).
306. Kim, H. T. *et al.* Stable multi-GeV electron accelerator driven by waveform-controlled PW laser pulses. *Scientific Reports* **7**, 10203 (2017).
307. Maier, A. R. *et al.* Decoding sources of energy variability in a laser-plasma accelerator. *Physical Review X* **10**, 031039 (2020).

308. Dann, S. J. D. *et al.* Laser wakefield acceleration with active feedback at 5 Hz. *Physical Review Accelerators and Beams* **22**, 041303 (2019).
309. Guénot, D. *et al.* Relativistic electron beams driven by kHz single-cycle light pulses. *Nature Photonics* **11**, 293–296 (2017).
310. Gustas, D. *et al.* High-charge relativistic electron bunches from a kHz laser-plasma accelerator. *Physical Review Accelerators and Beams* **21**, 013401 (2018).
311. Lazzarini, C. M. *et al.* 50 MeV electron beams accelerated by a terawatt scalable kHz laser, 2023. arXiv: 2302.11415 [physics.plasm-ph]. (visited on January 19, 2024).
312. Shaloo, R. J. *et al.* Hydrodynamic optical-field-ionized plasma channels. *Physical Review E* **97**, 053203 (2018).
313. Alejo, A., Cowley, J., Picksley, A., Walczak, R. & Hooker, S. Demonstration of kilohertz operation of hydrodynamic optical-field-ionized plasma channels. *Physical Review Accelerators and Beams* **25**, 011301 (2022).
314. Mangles, S. P. D. *et al.* Laser-wakefield acceleration of monoenergetic electron beams in the first plasma-wave period. *Physical Review Letters* **96**, 215001 (2006).
315. Popp, A. *et al.* All-Optical Steering of Laser-Wakefield-Accelerated Electron Beams. *Physical Review Letters* **105**, 215001 (2010).
316. Chen, L. M. *et al.* Bright betatron X-ray radiation from a laser-driven-clustering gas target. *Scientific Reports* **3**, 1912 (2013).
317. Wood, J. C. *et al.* Enhanced Betatron Radiation from a Laser Wakefield Accelerator in a Long Focal Length Geometry. *Gas* **1**, 2 (2017).
318. Yan, W. *et al.* Concurrence of monoenergetic electron beams and bright X-rays from an evolving laser-plasma bubble in *Proceedings of the National Academy of Sciences* **111** (2014), 5825–5830.
319. Zhang, Z. M. *et al.* Enhanced x-rays from resonant betatron oscillations in laser wakefield with external wigglers. *Plasma Physics and Controlled Fusion* **58**, 105009 (2016).
320. Ferri, J. & Davoine, X. Enhancement of betatron x rays through asymmetric laser wakefield generated in transverse density gradients. *Physical Review Accelerators and Beams* **21**, 091302 (2018).
321. Ma, Y. *et al.* Angular streaking of betatron X-rays in a transverse density gradient laser-wakefield accelerator. *Physics of Plasmas* **25**, 113105 (2018).
322. Ta Phuoc, K. *et al.* Betatron radiation from density tailored plasmas. *Physics of Plasmas* **15**, 063102 (2008).
323. Guo, B. *et al.* Enhancement of laser-driven betatron x-rays by a density-depressed plasma structure. *Plasma Physics and Controlled Fusion* **61**, 035003 (2019).
324. Shaw, J. L. *et al.* Role of direct laser acceleration in energy gained by electrons in a laser wakefield accelerator with ionization injection. *Plasma Physics and Controlled Fusion* **56**, 084006 (2014).

325. Cipiccia, S. *et al.* A tuneable ultra-compact high-power, ultra-short pulsed, bright gamma-ray source based on bremsstrahlung radiation from laser-plasma accelerated electrons. *Journal of Applied Physics* **111**, 063302 (2012).
326. Clendenin, J. E. *High-yield positron systems for linear colliders* in *Proceedings of the 1989 IEEE Particle Accelerator Conference* (1989), 1107–1111.
327. He, Y., Blackburn, T., Toncian, T. & Arefiev, A. Achieving pair creation via linear and nonlinear Breit–Wheeler processes in dense plasmas irradiated by high-intensity laser pulses. *Physics of Plasmas* **29**, 053105 (2022).
328. Burke, D. L. *et al.* Positron production in multiphoton light-by-light scattering. *Physical Review Letters* **79**, 1626 (1997).
329. Blackburn, T. G., Ridgers, C. P., Kirk, J. G. & Bell, A. R. Quantum radiation reaction in laser–electron-beam collisions. *Physical Review Letters* **112**, 015001 (2014).
330. Lobet, M., Davoine, X., d’Humières, E. & Gremillet, L. Generation of high-energy electron-positron pairs in the collision of a laser-accelerated electron beam with a multipetawatt laser. *Physical Review Accelerators and Beams* **20**, 043401 (2017).
331. Vranic, M., Klimo, O., Korn, G. & Weber, S. Multi-GeV electron-positron beam generation from laser-electron scattering. *Scientific Reports* **8**, 4702 (2018).
332. Ridgers, C. P. *et al.* Dense electron-positron plasmas and ultraintense γ rays from laser-irradiated solids. *Physical Review Letters* **108**, 165006 (2012).
333. Gu, Y.-J., Klimo, O., Bulanov, S. V. & Weber, S. Brilliant gamma-ray beam and electron–positron pair production by enhanced attosecond pulses. *Communications Physics* **1**, 93 (2018).
334. Nerush, E. N. *et al.* Laser field absorption in self-generated electron-positron pair plasma. *Physical Review Letters* **106**, 035001 (2011).
335. Chang, H. X. *et al.* Generation of overdense and high-energy electron-positron-pair plasmas by irradiation of a thin foil with two ultraintense lasers. *Physical Review E* **92**, 053107 (2015).
336. Zhu, X.-L. *et al.* Dense GeV electron–positron pairs generated by lasers in near-critical-density plasmas. *Nature Communications* **7**, 13686 (2016).
337. Jirka, M., Klimo, O., Vranic, M., Weber, S. & Korn, G. QED cascade with 10 PW-class lasers. *Scientific Reports* **7**, 15302 (2017).
338. Vranic, M., Grismayer, T., Fonseca, R. A. & Silva, L. O. Electron–positron cascades in multiple-laser optical traps. *Plasma Physics and Controlled Fusion* **59**, 014040 (2017).
339. Gong, Z. *et al.* High-efficiency γ -ray flash generation via multiple-laser scattering in ponderomotive potential well. *Physical Review E* **95**, 013210 (2017).
340. Efimenko, E. S. *et al.* Extreme plasma states in laser-governed vacuum breakdown. *Scientific Reports* **8**, 2329 (2018).
341. Zhu, X.-L., Yu, T.-P., Chen, M., Weng, S.-M. & Sheng, Z.-M. Generation of GeV positron and γ -photon beams with controllable angular momentum by intense lasers. *New Journal of Physics* **20**, 083013 (2018).

342. Zhao, J. *et al.* All-optical quasi-monoenergetic GeV positron bunch generation by twisted laser fields. *Communications Physics* **5**, 15 (2022).
343. Korn, G. *et al.* *Extreme light infrastructure (ELI): Physics and lasers at the ultra-intense frontier* in *Conference on Lasers and Electro-Optics* (2010), JThG2.
344. Sung, J. H. *et al.* 4.2 PW, 20 fs Ti:sapphire laser at 0.1 Hz. *Optics Letters* **42**, 2058–2061 (2017).
345. Zou, J. P. *et al.* Design and current progress of the Apollon 10 PW project. *High Power Laser Science and Engineering* **3**, e2 (2015).
346. Hernandez-Gomez, C. *et al.* *The Vulcan 10 PW Project* in *Journal of Physics: Conference Series* **244** (2010), 032006.
347. Meyerhofer, D. D. *et al.* *OMEGA EP OPAL: A Path to a 100-PW Laser System* in *APS Division of Plasma Physics Meeting Abstracts* **59** (2014), UO5.00006.
348. Kawanaka, J. *et al.* *Conceptual design of sub-exa-watt system by using optical parametric chirped pulse amplification* in *Journal of Physics: Conference Series* **688** (2016), 012044.
349. Peng, Y., Xu, Y. & Yu, L. Overview and status of station of extreme light toward 100 PW. *Reza Kenkyu* **49**, 93–96 (2021).
350. Heitler, W. *The Quantum Theory of Radiation* (Oxford, At the Clarendon Press, 1954).
351. Chen, H. *et al.* Relativistic positron creation using ultraintense short pulse lasers. *Physical Review Letters* **102**, 105001 (2009).
352. Chen, H. *et al.* Relativistic quasimonoenergetic positron jets from intense laser-solid interactions. *Physical Review Letters* **105**, 015003 (2010).
353. Liang, E. *et al.* High e⁺/e⁻ ratio dense pair creation with 10²¹ W.cm⁻² laser irradiating solid targets. *Scientific Reports* **5**, 13968 (2015).
354. Chen, H. *et al.* Scaling the yield of laser-driven electron-positron jets to laboratory astrophysical applications. *Physical Review Letters* **114**, 215001 (2015).
355. Sarri, G. *et al.* Table-top laser-based source of femtosecond, collimated, ultrarelativistic positron beams. *Physical Review Letters* **110**, 255002 (2013).
356. Xu, Z. Y. *et al.* New injection and acceleration scheme of positrons in the laser-plasma bubble regime. *Physical Review Accelerators and Beams* **23**, 091301 (2020).
357. Liu, W.-Y. *et al.* Tail-Wave-Assisted Positron Acceleration in Nonlinear Laser Plasma Wakefields. *Physical Review Applied* **19**, 044048 (2023).
358. Diederichs, S. *et al.* Positron transport and acceleration in beam-driven plasma wakefield accelerators using plasma columns. *Physical Review Accelerators and Beams* **22**, 081301 (2019).
359. Gessner, S. *et al.* Demonstration of a positron beam-driven hollow channel plasma wakefield accelerator. *Nature Communications* **7**, 11785 (2016).
360. Lindstrøm, C. A. *et al.* Measurement of transverse wakefields induced by a misaligned positron bunch in a hollow channel plasma accelerator. *Physical Review Letters* **120**, 124802 (2018).

361. Silva, T. *et al.* Stable positron acceleration in thin, warm, hollow plasma channels. *Physical Review Letters* **127**, 104801 (2021).
362. Doche, A. *et al.* Acceleration of a trailing positron bunch in a plasma wakefield accelerator. *Scientific Reports* **7**, 14180 (2017).
363. Liu, W.-Y. *et al.* Trapping and acceleration of spin-polarized positrons from γ photon splitting in wakefields. *Physical Review Research* **4**, L022028 (2022).
364. He, Y., Blackburn, T. G., Toncian, T. & Arefiev, A. V. Dominance of γ - γ electron-positron pair creation in a plasma driven by high-intensity lasers. *Communications Physics* **4**, 139 (2021).
365. Sugimoto, K. *et al.* Positron Generation and Acceleration in a Self-Organized Photon Collider Enabled by an Ultraintense Laser Pulse. *Physical Review Letters* **131**, 065102 (2023).
366. Martinez, B., Barbosa, B. & Vranic, M. Creation and direct laser acceleration of positrons in a single stage. *Physical Review Accelerators and Beams* **26**, 011301 (2023).
367. Boris, P. *Relativistic plasma simulation-optimization of a hybrid code in Proceedings of the Conference on the Numerical Simulations of Plasmas (4th)* (1970), 3–67.
368. Vay, J.-L. Simulation of beams or plasmas crossing at relativistic velocity. *Physics of Plasmas* **15**, 056701 (2008).
369. Higuera, A. V. & Cary, J. R. Structure-preserving second-order integration of relativistic charged particle trajectories in electromagnetic fields. *Physics of Plasmas* **24**, 052104 (2017).
370. Esirkepov, T. Exact charge conservation scheme for Particle-in-Cell simulation with an arbitrary form-factor. *Computer Physics Communications* **135**, 144–153 (2001).
371. Yee, K. Numerical solution of initial boundary value problems involving Maxwell's equations in isotropic media. *IEEE Transactions on Antennas and Propagation* **14**, 302–307 (1966).
372. Nuter, R. & Tikhonchuk, V. T. Suppressing the numerical Cherenkov radiation in the Yee numerical scheme. *Journal of Computational Physics* **305**, 664–676 (2016).
373. Godfrey, B. B. Numerical Cherenkov instabilities in electromagnetic particle codes. *Journal of Computational Physics* **15**, 504–521 (1974).
374. Cherenkov, P. A. Visible light from clear liquids under the action of gamma radiation. *Comptes Rendus (Doklady) de l'Academie des Sciences de l'URSS* **2**, 451–454 (1934).
375. Lehe, R., Lifschitz, A., Thaury, C., Malka, V. & Davoine, X. Numerical growth of emittance in simulations of laser-wakefield acceleration. *Physical Review Special Topics-Accelerators and Beams* **16**, 021301 (2013).
376. Brown, L. S., Preston, D. L. & Singleton Jr., R. L. Charged particle motion in a highly ionized plasma. *Physics Reports* **410**, 237–333 (2005).

377. Cranfill, C. W., Brackbill, J. U. & Goldman, S. R. A time-implicit Monte Carlo collision algorithm for particle-in-cell electron transport models. *Journal of Computational Physics* **66**, 239–249 (1986).
378. Nanbu, K. Theory of cumulative small-angle collisions in plasmas. *Physical Review E* **55**, 4642 (1997).
379. Nanbu, K. & Yonemura, S. Weighted particles in Coulomb collision simulations based on the theory of a cumulative scattering angle. *Journal of Computational Physics* **145**, 639–654 (1998).
380. Perelomov, A. M., Popov, V. S. & Terent'ev, M. V. Ionization of atoms in an alternating electric field. *Soviet Journal of Experimental and Theoretical Physics* **23**, 924–934 (1966).
381. Perelomov, A. M., Popov, V. S. & Terent'ev, M. V. Ionization of atoms in an alternating electric field: II. *Soviet Journal of Experimental and Theoretical Physics* **24**, 207–217 (1967).
382. Pérez, F., Gremillet, L., Decoster, A., Drouin, M. & Lefebvre, E. Improved modeling of relativistic collisions and collisional ionization in particle-in-cell codes. *Physics of Plasmas* **19**, 083104 (2012).
383. Niel, F., Riconda, C., Amiranoff, F., Ducloux, R. & Grech, M. From quantum to classical modeling of radiation reaction: A focus on stochasticity effects. *Physical Review E* **97**, 043209 (2018).
384. Vranic, M., Martins, J. L., Fonseca, R. A. & Silva, L. O. Classical radiation reaction in particle-in-cell simulations. *Computer Physics Communications* **204**, 141–151 (2016).
385. Lobet, M. *et al.* Modeling of radiative and quantum electrodynamics effects in PIC simulations of ultra-relativistic laser-plasma interaction in *Journal of Physics: Conference Series* **688** (2016), 012058.
386. Ritus, V. I. Quantum effects of the interaction of elementary particles with an intense electromagnetic field. *Journal of Soviet Laser Research* **6**, 497–617 (1985).
387. Thomas, A. G. R. Algorithm for calculating spectral intensity due to charged particles in arbitrary motion. *Physical Review Special Topics-Accelerators and Beams* **13**, 020702 (2010).
388. Chen, M. *et al.* Modeling classical and quantum radiation from laser-plasma accelerators. *Physical Review Special Topics-Accelerators and Beams* **16**, 030701 (2013).
389. Horný, V. *et al.* Temporal profile of betatron radiation from laser-driven electron accelerators. *Physics of Plasmas* **24**, 063107 (2017).
390. Pardal, M., Sainte-Marie, A., Reboul-Salze, A., Fonseca, R. & Vieira, J. RaDiO: An efficient spatiotemporal radiation diagnostic for particle-in-cell codes. *Computer Physics Communications* **285**, 108634 (2023).
391. Timokhin, A. N. Time-dependent pair cascades in magnetospheres of neutron stars—I. Dynamics of the polar cap cascade with no particle supply from the neutron star surface. *Monthly Notices of the Royal Astronomical Society* **408**, 2092–2114 (2010).

392. Elkina, N. V. *et al.* QED cascades induced by circularly polarized laser fields. *Physical Review Special Topics-Accelerators and Beams* **14**, 054401 (2011).
393. Duclous, R., Kirk, J. G. & Bell, A. R. Monte Carlo calculations of pair production in high-intensity laser–plasma interactions. *Plasma Physics and Controlled Fusion* **53**, 015009 (2010).
394. Arber, T. D. *et al.* Contemporary particle-in-cell approach to laser-plasma modelling. *Plasma Physics and Controlled Fusion* **57**, 113001 (2015).
395. Fonseca, R. A. *et al.* OSIRIS: A three-dimensional, fully relativistic particle in cell code for modeling plasma based accelerators in *Computational Science—ICCS 2002: International Conference Amsterdam, The Netherlands, April 21–24, 2002 Proceedings, Part III 2* (2002), 342–351.
396. Fonseca, R. A. *et al.* Exploiting multi-scale parallelism for large scale numerical modelling of laser wakefield accelerators. *Plasma Physics and Controlled Fusion* **55**, 124011 (2013).
397. Maslarova, D., Krus, M., Horny, V. & Psikal, J. Laser wakefield accelerator driven by the super-Gaussian laser beam in the focus. *Plasma Physics and Controlled Fusion* **62**, 024005 (2019).
398. Chen, Q. *et al.* Transient relativistic plasma grating to tailor high-power laser fields, wakefield plasma waves, and electron injection. *Physical Review Letters* **128**, 164801 (2022).
399. Mašlářová, D. *et al.* Generation of a static plasma electron grating in *Laser Acceleration of Electrons, Protons, and Ions VI* **11779** (2021), 8–13.
400. Chen, Q., Maslarova, D., Wang, J., Li, S. & Umstadter, D. Injection of electron beams into two laser wakefields and generation of electron rings. *Physical Review E* **106**, 055202 (2022).
401. Mašlářová, D., Horný, V., Krus, M. & Psikal, J. *Betatron radiation enhancement by a density up-ramp in the bubble regime of LWFA in Laser Acceleration of Electrons, Protons, and Ions V* **11037** (2019), 1103710.
402. Döpp, A. *et al.* Energy boost in laser wakefield accelerators using sharp density transitions. *Physics of Plasmas* **23**, 056702 (2016).
403. Golovanov, A. A. & Kostyukov, I. Y. Bubble regime of plasma wakefield in 2D and 3D geometries. *Physics of Plasmas* **25**, 103107 (2018).
404. Ferri, J. *Étude des rayonnements Bétatron et Compton dans l'accélération d'électrons par sillage laser*. PhD thesis (Université Paris-Saclay, 2016).
405. Maslarova, D., Martinez, B. & Vranic, M. Radiation-dominated injection of positrons generated by the nonlinear Breit–Wheeler process into a plasma channel. *Physics of Plasmas* **30**, 093107 (2023).



Appendix: Included publications



■ Publication A

Reference:

D. Maslarova, M. Krus, V. Horny, and J. Psikal. "Laser wakefield accelerator driven by the super-Gaussian laser beam in the focus". In: *Plasma Physics and Controlled Fusion* 62.2 (2019), p. 024005.

Available from:

<https://iopscience.iop.org/article/10.1088/1361-6587/ab57ee/meta>

The author of the thesis:

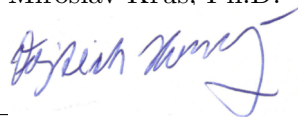
- performed and analyzed numerical simulations,
- prepared visualization,
- was the main and corresponding author,
- proposed methodology,
- led the initial conceptualization process,
- edited the manuscript with the other co-authors.

The undersigned co-authors, M. Krůs, V. Horný, and J. Pšikal, hereby affirm that the contributions of the thesis author to the publication, as detailed above, are accurately presented.



Ing. Miroslav Krůs, Ph.D.

Digitally signed
by Vojtěch Horný



Ing. Vojtěch Horný, Ph.D.



doc. Ing. Jan Pšikal, Ph.D.



■ Publication B

Reference:

Q. Chen, D. Maslarova, J. Wang, S. X. Lee, V. Horný, and D. Umstadter. "Transient relativistic plasma grating to tailor high-power laser fields, wakefield plasma waves, and electron injection". In: *Physical Review Letters* 128.16 (2022) p. 164801.

Available from:

<https://journals.aps.org/prl/abstract/10.1103/PhysRevLett.128.164801>

The author of the thesis:

- performed and analyzed numerical simulations,
- proposed the methodology of the simulations,
- prepared the visualization of the simulation outcomes,
- co-wrote the manuscript with the other co-authors,
- edited the manuscript with the other co-authors,
- contributed to the interpretation of the experimental and simulations results,
- contributed to conceptualization.

The undersigned, Q. Chen, the main and corresponding author of the publication, hereby affirms on behalf of all co-authors that the contributions of the thesis author, as detailed above, are accurately presented.



Dr. Qiang Chen



■ Publication C

Reference:

Q. Chen, D. Maslarova, J. Wang, S. X. Lee, and D. Umstadter. " Injection of electron beams into two laser wakefields and generation of electron rings". In: *Physical Review E* 106.5 (2022) p. 055202.

Available from:

<https://journals.aps.org/pre/abstract/10.1103/PhysRevE.106.055202>

The author of the thesis:

- performed and analyzed numerical simulations,
- proposed the methodology of the simulations,
- prepared the visualization of the simulation outcomes,
- co-wrote the manuscript with the other co-authors,
- edited the manuscript with the other co-authors,
- contributed to the interpretation of the experimental and simulations results,
- contributed to conceptualization.

The undersigned, Q. Chen, the main and corresponding author of the publication, hereby affirms on behalf of all co-authors that the contributions of the thesis author, as detailed above, are accurately presented.



Dr. Qiang Chen



■ Publication D

Reference:

D. Mašlárová, V. Horný, M. Krůs, and J. Pšikal. “Betatron radiation enhancement by a density up-ramp in the bubble regime of LWFA”. In: *Laser Acceleration of Electrons, Protons, and Ions V*. Vol. 11037. *International Society for Optics and Photonics*. 2019, p. 1103710.

Available from:

<https://www.spiedigitallibrary.org/conference-proceedings-of-spie/11037/1103710/Betatron-radiation-enhancement-by-a-density-up-ramp-in-the/10.1117/12.2520980.full>

The author of the thesis:

- performed and analyzed numerical simulations,
- prepared visualization,
- was the main and corresponding author,
- proposed methodology,
- led the initial conceptualization process,
- edited the manuscript with the other co-authors.

The undersigned co-authors, V. Horný, M. Krůs, and J. Pšikal, hereby affirm that the contributions of the thesis author to the publication, as detailed above, are accurately presented.

Digitally signed
by Vojtěch Horný



Ing. Vojtěch Horný, Ph.D.



Ing. Miroslav Krůs, Ph.D.



doc. Ing. Jan Pšikal, Ph.D.



■ Publication E

Reference:

D. Maslarova, B. Martinez, and M. Vranic. "Radiation-dominated injection of positrons generated by the nonlinear Breit–Wheeler process into a plasma channel." In: *Physics of Plasmas* 30.9 (2023) p. 093107.

Available from:

<https://doi.org/10.1063/5.0160121>

The author of the thesis:

- performed theoretical analysis,
- performed and analyzed numerical simulations,
- prepared visualization,
- was the main and corresponding author,
- proposed methodology with the other co-authors,
- edited the manuscript with the other co-authors,
- contributed to conceptualization,
- contributed to data curation.

The undersigned, M. Vranic, the supervisor of the project, hereby affirms on behalf of the co-authors that the contributions of the thesis author to the publication, as detailed above, are accurately presented.



Dr. Marija Vranic